UNIVERSITÀ DEGLI STUDI DI GENOVA

FACOLTÀ DI INGEGNERIA

Tesi di Laurea in INGEGNERIA MECCANICA

STUDY ON SKYBIRD PERFORMANCE IMPROVEMENT

RELATORE:

CHIAR.MO PROF. ALESSANDRO BOTTARO

CO-RELATORE:

DOTT. ING. JOEL GUERRERO

ALLIEVO:

FEDERICO VECCHIA

Anno Accademico: 2011/2012

DICCA

Ringraziamenti

Un sincero ringraziamento va al mio professore e relatore Prof. Alessandro Bottaro e al Dipartimento di Ingegneria Chimica, Civile ed Ambientale, grazie ai quali ho potuto prendere parte allo sviluppo del progetto *"Skybird"* in collaborazione con Selex Galileo MUAS. Ringrazio inoltre l'Ing. e ricercatore Joel Guerrero per il tempo e la disponibilità dedicatami nell'introduzione e nell'utilizzo degli strumenti di calcolo necessari alla stesura di questa tesi. Un cordiale ringraziamento va anche all'Ing. Carlo Pacioselli per la pazienza avuta nel darmi le prime e necessarie informazioni sul progetto "*Skybird",* durante la compilazione della sua tesi di Laurea Magistrale in Ingegneria Meccanica.

Un grande ringraziamento va ai miei genitori Laura ed Elvio, per il loro supporto morale e la fiducia dimostratami fino a questo punto degli studi. Ringrazio loro anche per aver appoggiato moralmente, e non solo, le importanti esperienze all'estero intraprese negli ultimi anni. Infine ringrazio il compagno di studi Lorenzo Vaggi, con il quale ho condiviso gran parte del mio percorso di studi, per la sua amicizia e per la costanza nei comuni impegni accademici.

Acronyms and frequently used symbols

"0.0" – Case base label

μ_T – turbulent eddy viscosity

AFW – Articulated Flapping Wing

BCs – Boundary Conditions

BD – Backward Differencing

CAD – Computer Aided Drawing

C_D – Drag coefficient

CFD – Computational Fluid Dynamics

C_L – Lift coefficient

C_m – Average aerodynamic chord length

CN – Crank Nicholson

C_S – Side force coefficient

$\mathcal{CV}$ – Control Volume

DNS – Direct Numerical Simulation

f – Frequency

FVM – Finite Volume Method

GPS – Global Positioning System

LES – Large Eddy Simulation

MAV – Micro Aerial Vehicle

NACA – National Advisory Committee for Aeronautics (nowadays, NASA)

NSE – Navier-Stokes Equation

p – Pressure

PDE – Partial Differential Equation

RAF – Royal Air Force

RANS – Reynolds Averaged Navier-Stokes

Re – Reynolds number

RFA – Relative Flapping Angle

S – Wing planform surface

SIMPLE – Semi-implicit Method for Pressure-Linked Equations

SST – Shear Stress Transport

TVD – Total Variation Differencing

u, v, w – Components of the velocity vector

UAV – Unmanned Aerial Vehicle

UDF – User Defined Function

URANS – Unsteady Reynolds Averaged Navier-Stokes

VLM – Vortex Lattice Method

x – Position vector

$\boldsymbol{\vartheta}_{\mathbf{in,out,rel}}$ – Wing angle in time

$\boldsymbol{\kappa}$ – Turbulent kinetic energy

$\boldsymbol{\rho}$ – Density

$\boldsymbol{\tau}^{\mathbf{R}}$ – Reynolds Stress tensor

$\boldsymbol{\Phi}$ – Flux

Abstract

The collaboration with SELEX GALILEO MUAS has brought the opportunity to the University of Genova to collaborate to the development of a *UAV* (Unmanned Aerial Vehicle). This project, baptized the *Skybird*, focuses on a vehicle for reconnaissance and screening missions. Similar *UAV*s have been already designed and assembled but mainly with the sake of flying their own weights. The *Skybird* project plans features such as half an hour of flight time and total weight about 1kg mass (≈10 N) including structure and kinematic, high power batteries, avionics and operational devices. The relatively small aerodynamic surfaces require a particular and optimized design based on fluid dynamics simulations using *CFD* (Computational Fluid Dynamics) software. Flapping wings are necessary for multiple reasons. First of all, a flapping source of motion is the only way to provide enough lift to sustain this object, the flight of which is characterized by a low Reynolds number. Secondly, thrust is needed and it can be obtained by a particular kinematics of the flapping wing motion (such as the dynamic pitch of the wings). Also, maneuverability is an important issue, and it is expected that a flapping-wing vehicle may display better characteristics that a fixed-wing model, to the point of being even able to perch onto a tree. Last but not least, considering the purpose of this *UAV*, the biomimetic issue has to be accomplished which means that the usage of any kind of (noisy) propeller is definitely not allowed. Thus shape and motion have to remind the flight of an actual bird. The feasibility study has been developed in parallel with the DIME Department of the University, which is in the process of designing the mechanical train in order to make the actual robot perform the kinematics previously tested and optimized.

An introduction to the subject is given with an overview about *MAVs* and *UAV*s already designed and built by different developers over the last few years (Chapter 1). Then, the focus will be placed particularly on the development of the *Skybird*, from the creation of the geometry, to the *CFD* simulations performed so far (Chapter 2). This will be the starting point of the actual study. Chapter 3 will present the performance improvement process of the wing shape. The smooth and aerodynamic edges of the wing make the resistance decrease and wing end tips reduce the induced drag coefficient. Throughout Chapter 4 theoretical concepts of Computational Fluid Dynamics will be recalled, upon which simulations are based and the *CFD* software finds solutions. "*ANSYS Fluent R14®*" has been used to simulate and provide results for different cases. Each one of the improved components has been separately tested and compared with the standard, initial geometry of the *Skybird*. The final layout of improvements and all results of simulations are presented in Chapter 5 of this report. The conclusions ending this study and the future work are presented in Chapter 6.

Traduzione >>>

Prefazione

La collaborazione con SELEX GALILEO MUAS ha portato all'Università di Genova la possibilità di collaborare allo sviluppo di un *UAV* (Unmanned Aerial Vehicle). Questo progetto, battezzato *Skybird*, riguarda un velivolo ad ala battente per la sorveglianza e missioni di ricognizione. *UAV* simili sono stati già progettati e prodotti, ma con il principale scopo di volare sostenendo esclusivamente il proprio peso. Il progetto Skybird prevede caratteristiche quali mezz'ora di autonomia di volo e totale massa di circa un chilogrammo (equivalente a circa *10 N* di peso). Nel *payload* sono inclusi struttura meccanica e cinematismo, batterie di elevata potenza, avionica e dispositivi operativi. Le superfici aerodinamiche relativamente ridotte richiedono una particolare progettazione e ottimizzazione, basate su simulazioni fluidodinamiche, utilizzando un software di *CFD* (Computational Fluid Dynamics). Una propulsione ad ali battenti è necessaria per molteplici ragioni. Prima di tutto, una simile dinamica è l'unica alternativa per fornire portanza sufficiente a sostenere questo oggetto, il cui volo è caratterizzato da un basso numero di Reynolds. In secondo luogo, è necessaria una spinta nella direzione di volo ed essa può essere ottenuta da una particolare cinematica del moto dell'ala battente (il cosiddetto svergolamento dinamico). Inoltre è importante la manovrabilità e si prevede che un veicolo *flapping-wing* possa avere migliori caratteristiche di un modello ad ala fissa, fino al punto di essere in grado di atterrare autonomamente o addirittura appollaiarsi su un albero. Ultimo aspetto, ma non per importanza, è il mimetismo. Considerando lo scopo di questo *UAV*, l'utilizzo di qualsiasi tipo di elica (rumorosa) non può essere preso in considerazione. La forma e il movimento devono ricordare il più possibile il volo di un uccello reale. Lo studio di fattibilità è stato sviluppato in parallelo con il dipartimento DIME dell'Università, che è in fase di progettazione del treno meccanico per conferire al robot la cinematica precedentemente testata e ottimizzata.

Un'introduzione all'argomento di interesse di questa tesi è fornita attraverso una panoramica sugli *MAV* e *UAV* progettati e costruiti da diversi sviluppatori negli ultimi anni (*Capitolo 1*). Successivamente, l'attenzione sarà posta in particolare sullo sviluppo dello *Skybird*, dalla creazione della geometria, alle simulazioni *CFD* eseguite fino ad ora (*Capitolo 2*). Questo sarà il punto di partenza dello studio in questione. Il *Capitolo 3* presenterà il processo di ottimizzazione delle prestazioni a partire da modifiche della forma dell'ala: bordi lisci e aerodinamici delle superfici alari consentono una diminuzione della resistenza e alette di fondo ala riducono il coefficiente di resistenza indotta. Nel *Capitolo 4* saranno richiamati i concetti teorici di fluidodinamica computazionale, sui quali sono basate le simulazioni e attraverso le quali il software *CFD* calcola le soluzioni. "*ANSYS Fluent R14®*" è stato utilizzato per simulare i vari casi e fornire risultati. Ognuno dei componenti aggiuntivi è stato testato separatamente e confrontato con la geometria iniziale di riferimento dello *Skybird*. La visione d'insieme dei risultati e delle migliorie simulate sono presentati nel C*apitolo 5* di questa tesi. Le conclusioni tratte da questo studio e il lavoro futuro sono argomento del *Capitolo 6*.

Table of Contents

List of figures

1. Existing configurations of *MAVs* and *UAVs*

Usually any scientific study starts from what others have already achieved. *Skybird* study is not an exception, so in this chapter existing devices, which have been developed and manufactured by many companies for civilian or military sakes, will be presented. The overview on such vehicles will be organized by sections according to the nature of the machines: a brief summary on fixed wing *UAV*s, then *MAV*s and *UAV*s based on flapping wing technology [1].

1.1 Fixed wing *UAVs*

These prototypes of *UAV*s are just the point of reference for more complicated devices, since they come from a widely explored field of research in flight dynamics. They are put in motion by a propeller and essentially based on the geometry of small airplanes. These objects are basically built with common modelling materials such as balsa wood, fiber glass tape or *EPP (expanded polypropylene)*, which has high resilience properties and very low weight. However, structures of the *UAV*s involve carbon fiber or steel rods and braces. Some examples with relative performance are presented below.

1.1.1 Desert Hawk (Lockheed-Martin)

Length	***91 cm***
Wing span	***1.37 m***
Area	***0.128 m***^{2}
Weight	***3 kg (+payload 1kg)***
Motor	***electric***
Max endourance	***90+min***
Max range	***15 km***

Table 1: Desert Hawk characteristics.

Figure 1.1: Control set of the Lockheed-Martin Desert Hawk and view of its recognition devices.

1.1.2 Raven (Aerovironment)

Length	*109 cm*
Wing span	*1.3 m*
Weight	*1.9 kg*
Flight level	*30-152 m*
Motor	*electric*
Batteries	*lithium ions*
Max endourance	*60-90 min*
Max range	*10 km*

Table 2: Raven characteristics.

Figure 1.2: Hand launch of the Raven.

Aerovironment has been working on the field for many years. The first prototype has been developed in 1999; the last one, the so called Raven, is the newest. It has also been used in Afghanistan for recognitions and surveillance operations. Like the others, it needs a manual thrust to take off; however, it is equipped with a *GPS* device to track the course and a program to guide itself back to the starting point.

1.1.3 Bird Raptor International

This vehicle has been developed with the purpose of avoiding the so called *bird strike hazard*. The body of this *UAV* reproduces the shape of a hawk, in order to turn away birds from places where they could be potentially dangerous, such as airports. The model is made out of Kevlar and it is equipped with a speaker to frighten birds. The wing position is fixed and the thrust comes from a propeller mounted on the beak.

Figures 1.3: Views of the Bird Raptor.

1.2 Flapping wing *MAVs*

This section concerns those vehicles with very small dimensions which reproduce the natural motion of birds or insects. *MAV* (Micro air Vehicles) are usually equipped with a particular kinematic train which creates the flapping motion from a rotational movement. Pitching motion is usually not adopted in these models. These flying machines are basically developed by universities and closely connected to hobby-modelling. In other words, it is more interesting in terms of mechanical structure and kinematics than from the point of view of the aerodynamic study.

1.2.1 Flapping wing Micro-robots

Some universities around the world have developed, as research studies, micro-robots able to fly. A high frequency of the flapping motion produces enough lift to make them able to sustain their low weight.

Berkeley University (USA) and Delft University (Netherlands) are the developers of the *MAV*s described below. Both of them remind the shape and the flight of a dragonfly. In fact, highly resilient rods sustain flexible wing and the movement is induced by their. The Delfly II (as the name suggests, by Delft University) is also able to *hover*, due to its extreme lightness.

Figure 1.4: BOLT by Berkeley University.

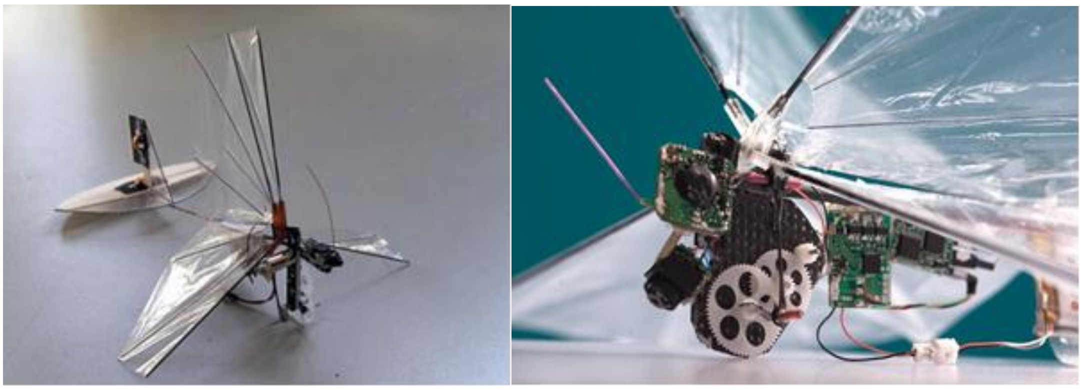

Figure 1.5: Delfly II (Delft University).

1.2.2 Models constructed at UNIGE

Our team has assembled two different ornithopters available on internet stores as mounting kits. Base structural material is balsa wood, whereas mountings and pins are made by metal. A certain fragility of the wing structure has been noticed, since sometimes balsa is not resilient enough to allow high local pressure which occurs around connections between elements. The asymmetry of the motion must also be underlined. As can be seen from Figure 1.6, the rotary motion is directly connected to the wings. However, each wing is driven separately, thus a delay occurs between the motion of the left wing and the right wing. This makes the model turn in the air describing a helix with a certain radius, function of the frequency of the flapping.

Figure 1.6: Luna construction kit ornithopter.

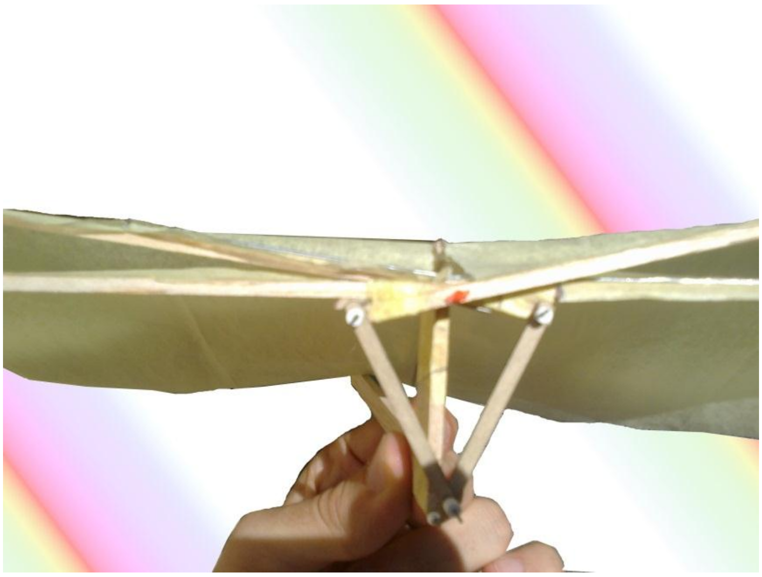

Figure 1.7: Kinematics of the Luna Ornithopter.

1.2.3 BEHEMOTH 4 by Patricia Jones-Bowman

This model is described in the website [2]. The site contains also links to activities of many others keen on small scale ornitopters. Patricia Jones-Bowman, has also been *test pilot* for all the large scale prototypes realized by James DeLaurier at UTIAS (Canada), from 1995 to 2001.

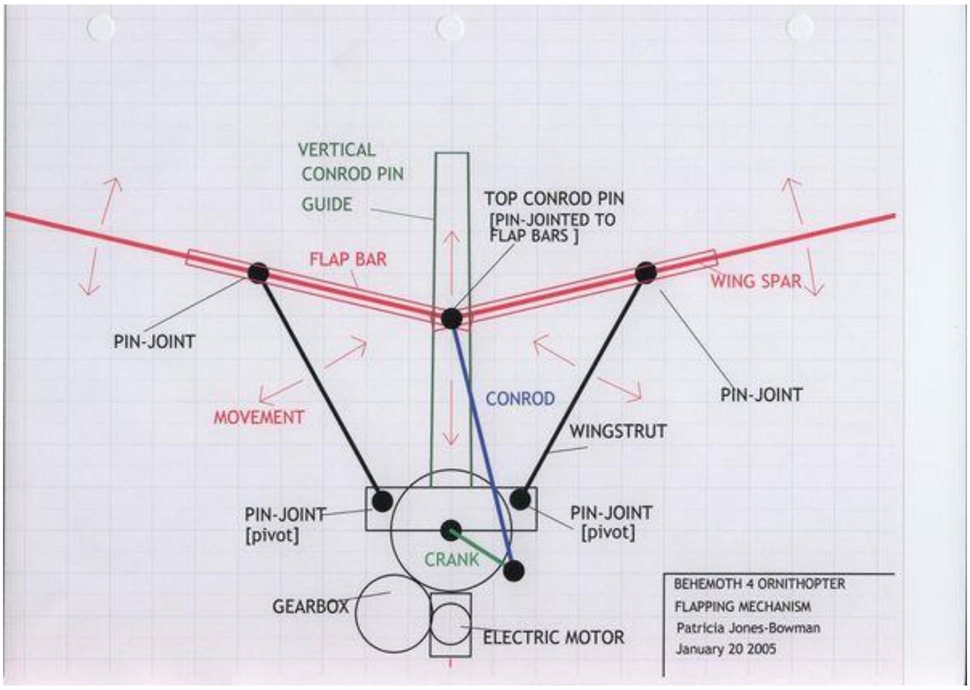

Figure 1.8: Mechanical kinematic of translation from rotational to flapping motion of Behemoth 4.

The most interesting part is the kinematic train, especially for its usage in more complicated models since this version avoids the problem previously described of the asymmetry of the motion. This mechanism makes the wings move essentially in the same way as the previous models shown in Figure 1.8. However, the pole of rotation and the point of transmission of the motion on the wings are switched and the sliding element assures the symmetry of the flapping.

1.3 Flapping wing *UAVs*

The main feature of the Unmanned Aerial Vehicles is the possibility to control them remotely or even program them and let them act without the human presence. Their use is particularly well fitted in dangerous places or operations; not only in military missions in war sceneries, but also civil tasks in chemically or radioactively compromised areas. Especially in the first case, the model appearance and dynamics have to be as close as possible to an actual bird, according to the place of use and local distribution of certain species of animal. Since this type of robots are the most technologically developed so far, they are supplied with complicated mechanical train able to reproduce the flapping motion of the wing considering many of the joints of a real bird wing.

The large field of application justifies fluid dynamics and aerodynamics studies in order to have realistic simulations before the actual manufacturing of the prototypes.

1.3.1 Greenx artificial bird

The finality of Greenx [3] is to develop robots as close to reality as possible to prevent the so called bird strike hazard. In other words the issue is to free the airport aerial zones from birds. The idea of the usage of a *UAV* came from the fact that the hawks used with this goal experience sometimes strikes with planes. A *UAV* can be programmed in order not to intersect flight paths of planes. This robot has been developed with a flapping wing system because it apparently frightens more the potential prays under attack of a predator. It is realized with plastic and fiber glass and it needs a hand launch for take-off.

Figure 1.9: Views of Greenx artificial bird on flight.

1.3.2 Ornithopter Project (UTIAS)

Ornithopter Project [4] by UTIAS (University of Toronto Institute for Aerospace Studies) is probably one of the most systematic and long term studies on *UAV* system. Directed by the aerodynamics and aerospace professor James DeLaurier, this project is based on studies on aeronautics and structural systems and it led to flight not only scaled models but also a prototype of the ornithopter with a pilot on board [5].

Adaptive aero elasticity is the base of the mobile wings motion, which is a combination of *heaving* and *pitching*.

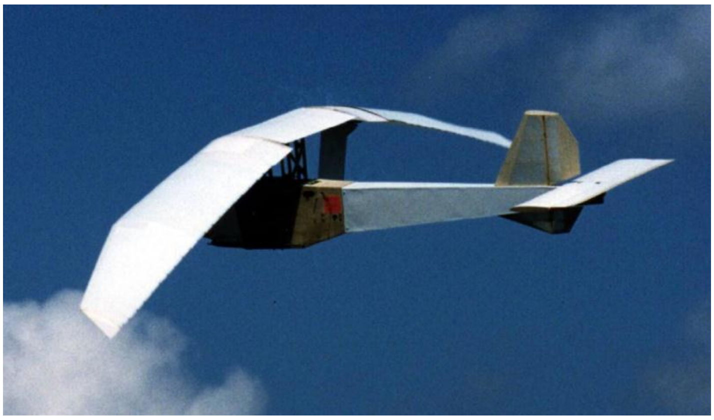

Figure 1.10: Ornithopter on flight.

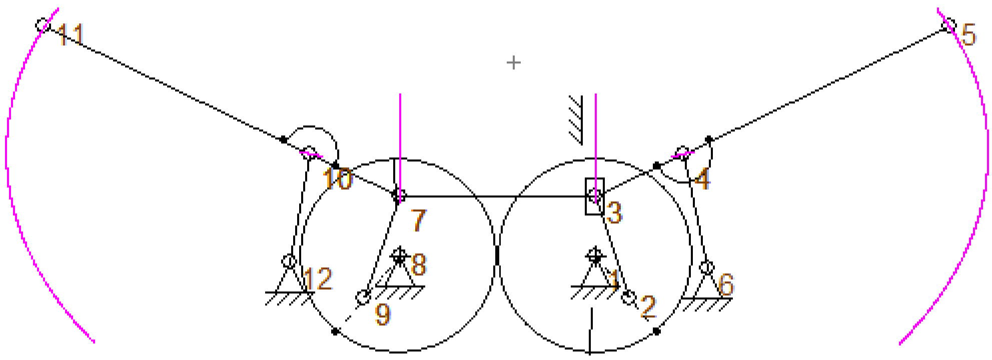

Figure 1.11: Structural mechanism of the ornithopter.

The purple lines are the trajectories of the wing tips, i.e. the output of the system. The motion law of the wing is a periodic oscillation, generally a combination of sines and cosines, asymmetric with respect to the horizontal axis.

1.3.3 Festo Smartbird

Festo is a German Company which works in the field of robotics and mechatronics [6]. It is well known around the world for its demonstrative reproductions of biomechanical systems of existing animals. The most interesting from our point of view is the so called Smartbird. Festo developed this project throughout eight years of studies by a team of engineers, as documented on their website by interviews and videos on *YouTube* [7].

The flapping wings of the Smartbird are composed by many parts, some rigid, some flexible. Essentially the wing structure can be represented by the rigid bodies interconnected by a rotational coupling at which flexible parts are attached.

Both lift and thrust are provided by the wings; they come from two different movements though, respectively, *flapping* and *pitching*. This is realized by a torsion servo-mechanism which allows a certain efficiency on flight. The control of the flight is mainly an issue of the tail adaptive surface. It gives also the necessary stability to the flight.

Smartbird is not equipped with any kind of gear or slide to take off and land from on the ground. However it can start in autonomy a flight without the help of a hand launch.

It is realized with extra light material for the external body and, reasonably, carbon fiber for structural parts. It is very well designed from the aerodynamic point of view, it enjoys high density of power with respect to thrust and lift and high agility in movements. This is probably the highest point which engineering have achieved through the years in the field of biomimetic flapping wing systems.

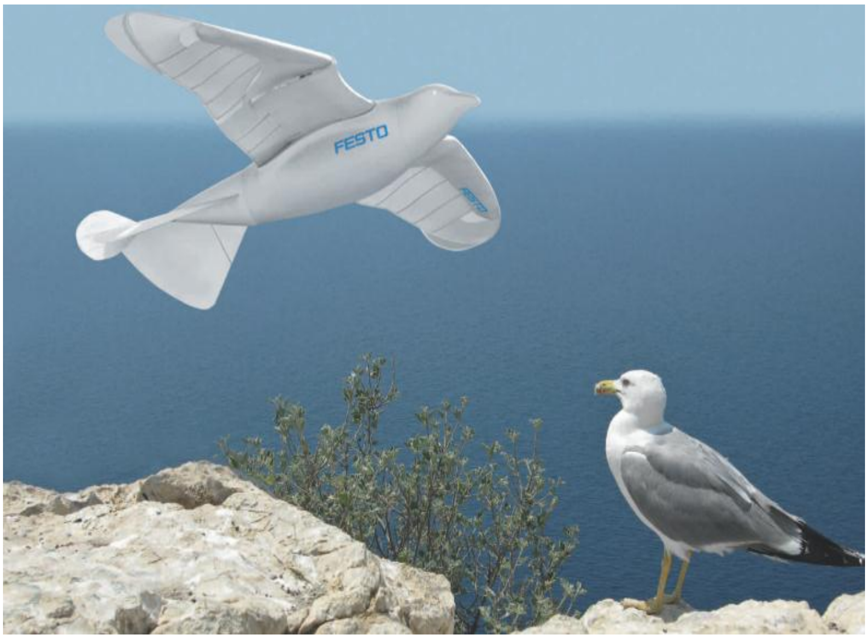

Figure 1.12: Festo Smartbird compared to a seagull.

Figure 1.13: Smartbird components and view of the *UAV* compared to the human scale.

Length	*1.07 m*
Wing span	*2.00 m*
Wight	*0.450 kg*
Structure	*Carbon fiber*
Body	*Polyurethane foam*
Batteries	*Lithium polymers cell, 2 cells, 7.4 V, 450 mA*
Required electric power	*23 W*
Motor	*compact 135, brushless*

Table 3: Characteristics of the Smartbird.

2. Previous development and state-of-the-art of the *Skybird*

In this chapter all the work done before since the beginning of the project will be presented. A brief summary of the steps which brought to the current configuration of the *Skybird* and some of the essential results found so far will be shown.

2.1 Preliminary project

Wing shapes of different birds have been considered from an aerodynamic point of view [8]. Geometric quantities related to flight performance such as *camber line, airfoil thickness, wing span, twist angle, etc.* have been stored as analytic data. After a first sight and theoretical comparison it turned out that seagull and owl wings were likely the highest performing wing shapes. Thus, a robotic arm equipped with the visual technology *3D NVision* has been used to capture a three-dimensional model of an actual wing (Figure 2.1).

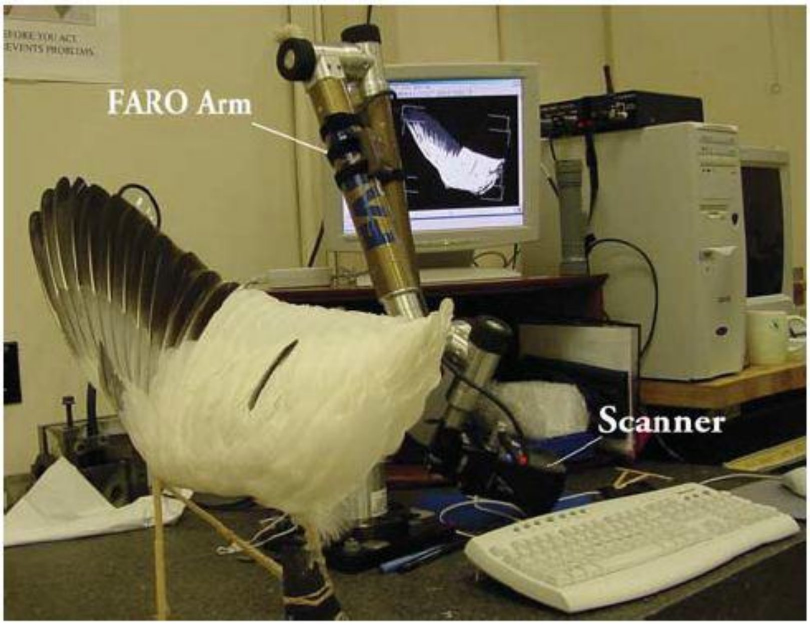

Figure 2.1: 3D Laser Scanner.

2.1.1 Seagull and owl wing planforms

A statistical approach to collected data has been necessary to compute coefficients. For instance, some of them are *curvature line angle* (Figure 2.2), *distribution of the wing thickness* (Figure 2.3) and *distribution of the chord length.* This made possible to reconstruct an analytical model of the wing planform (Figure 2.4), which has been the origin of the wing used in the preliminary geometry of the *Skybird*.

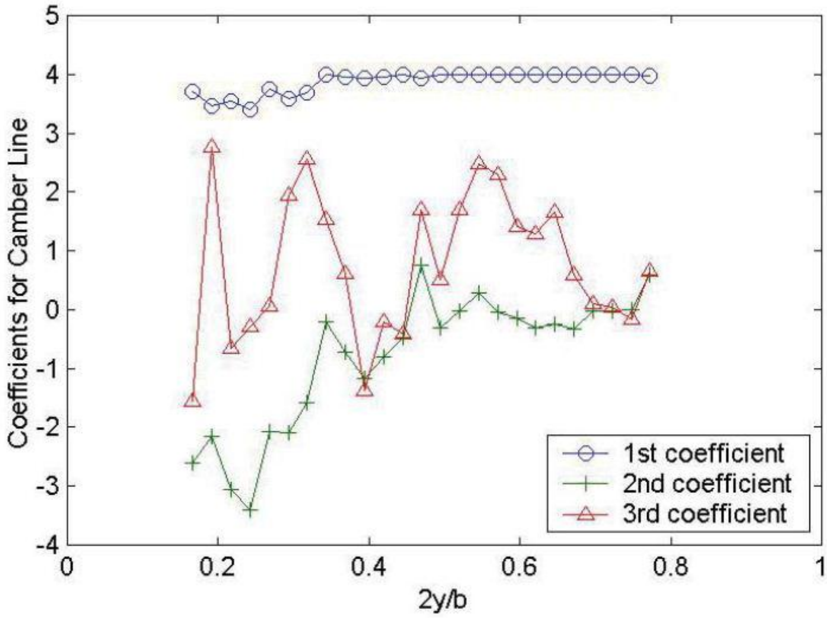

Figure 2.2: Curvature line coefficients.

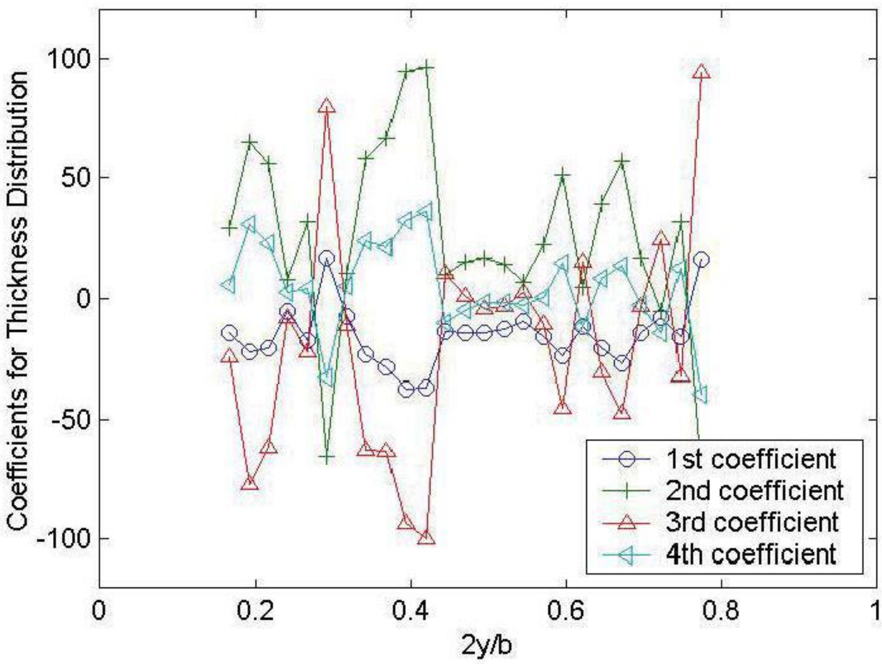

Figure 2.3: Distribution of the wing thickness coefficient.

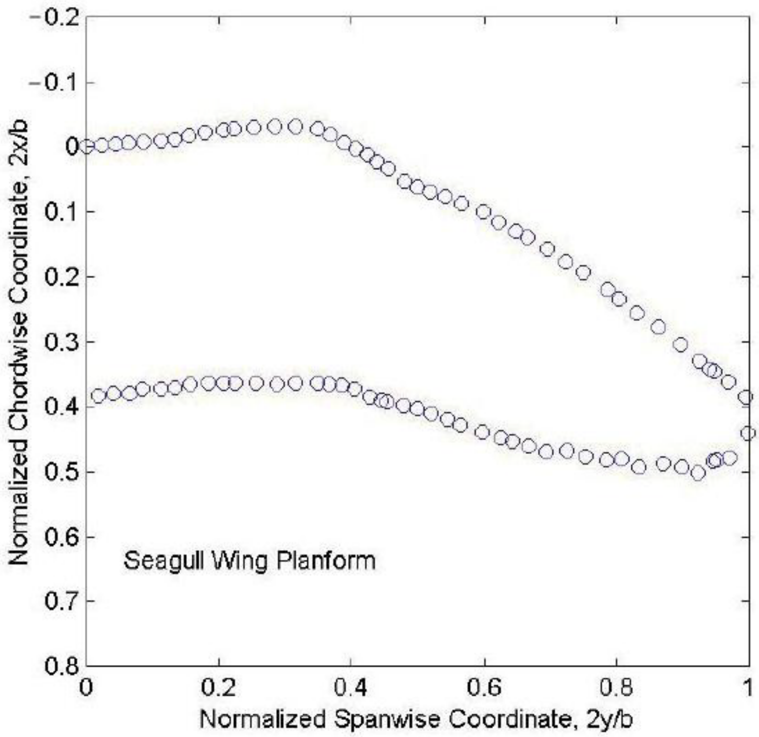

Figure 2.4: Seagull wing planform.

At first instance all the edges have been considered continuous. This first order approach was preferred than considering the irregular shape due to long feathers, especially at the wingtips. This, however, will be the main concern of next chapters and thus, tackled further.

As far as the owl wing planform is concerned, it is much thinner than the seagull one, as shown in Figure 2.5. From a plan view it appears squatter (Figure 2.6) and, considering the different scale, less spanned than the seagull wing. However, as said before, the owl wing geometry will be rejected since not as efficient as that of the seagull for the purposes of the *Skybird*.

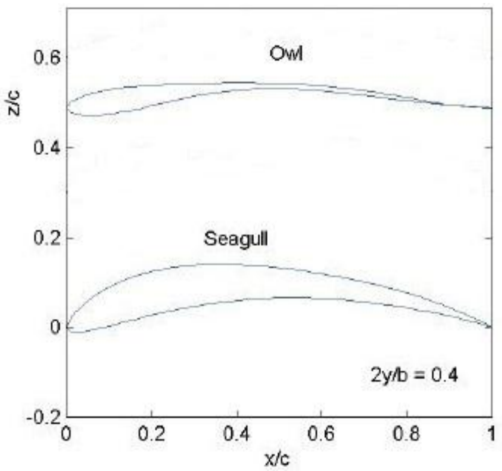

Figure 2.5: Comparison between owl and seagull airfoils.

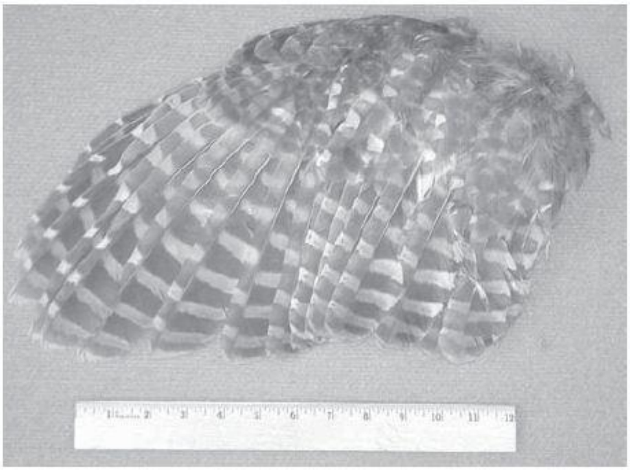

Figure 2.6: Planform view of the owl wing.

2.2 Geometry creation

2.2.1 Seagull wing

The wing geometry creation is the first and most complicated concern. Software called "*GraphClick*" [9] has been used to edit the *Nvision* data input into a *CAD* drawing extension. "*Solidworks 2011*" [10] has been chosen among other commercial softwares capable to import a line from a *.txt* file. A reference system *xyz* is assigned, pointing respectively towards *chord, perpendicular to wing plan* and *wing span.* A closed *spline,* as result of the command "*line from points",* forms the root airfoil (Figure 2.7). This has been the starting point of the parametric model. Using the *Solidworks* command "*extrusion*", the airfoil has been projected in three dimensions to recreate the wing of the seagull. Trailing and leading edges of the wing shape worked out as "*guidelines*" of the extrusion. In other words they are the three-dimensional limits within which the root airfoil is swept in space.

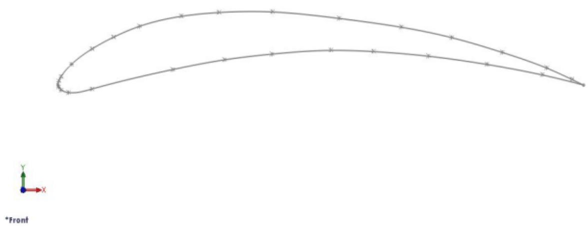

Figure 2.7: Root section of the seagull wing.

Then, the solid wing is deformed by a small dihedral angle to recreate the actual shape of the seagull wing and to give more stability during flight, as shown in Figure 2.8.

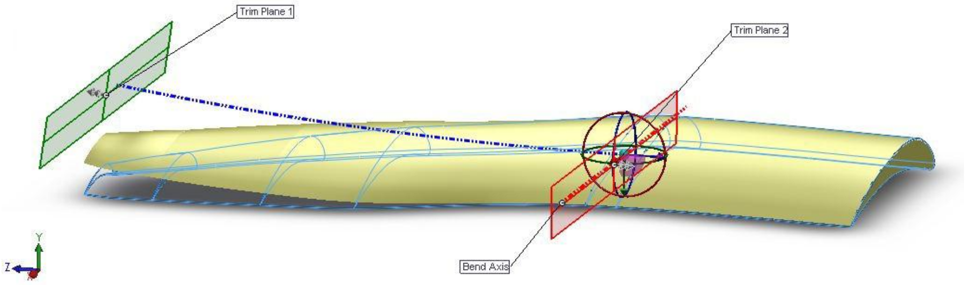

Figure 2.8: Setting up of the dihedral angle through *Solidworks* "flex" command.

Finally, a scaling factor is used to adequate the quotes of the model to the needed *chord* and *span* dimensions. Final version of the wing and its characteristics are shown in Figure 2.9.

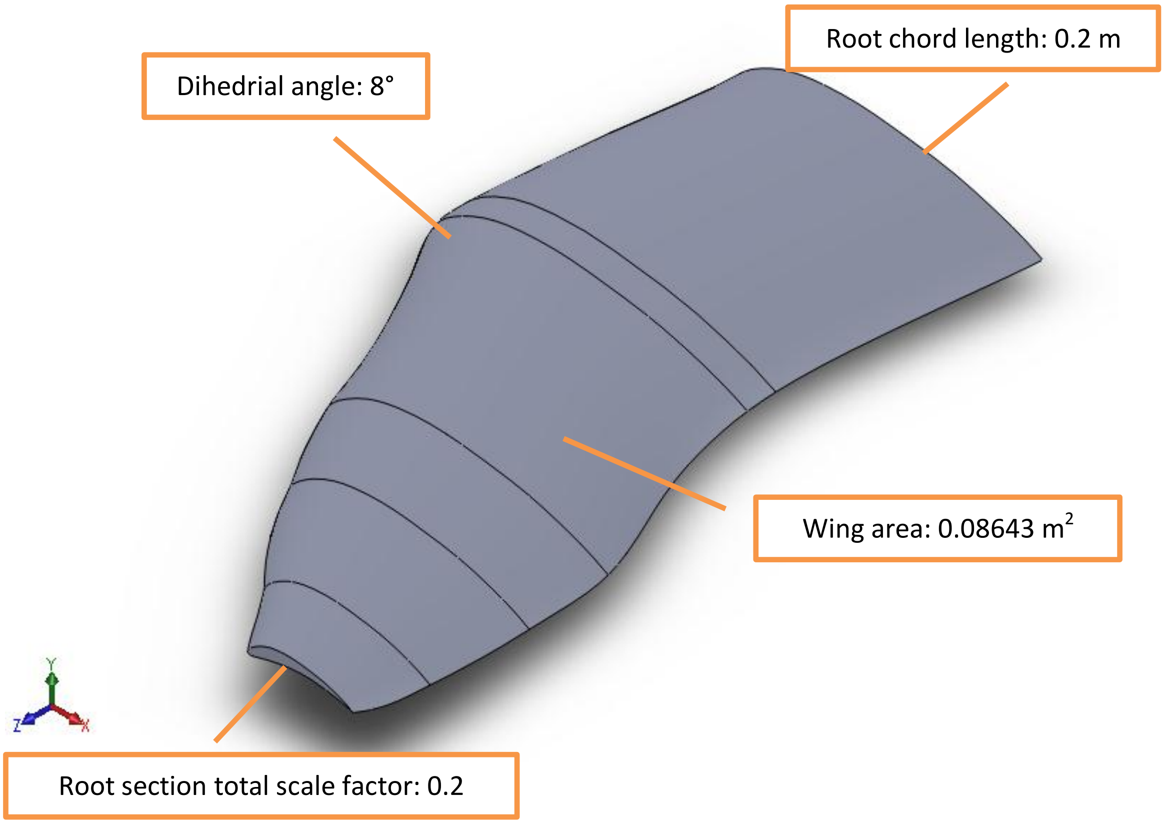

Figure 2.9: Isometric view of the seagull wing.

2.2.2 Selig wing

Despite the fact that previous study has been dedicated to a faithful recreation of the bird wing, from an engineering point of view it is more usual to approach problems in a standardized way. Using a standard airfoil profile allows a wider range of improvements, since a huge amount of database of airfoil performance already exists. This designing is aiming to a single prototype; however, also the production process can be quicker if dealing with a standard wing cross section. Many airfoils have been developed and improved all in time with different goals and applications in different situations. In this particular case we have looked for an airfoil designed for low-Reynolds number flight. Selig profile S1223 [11] (Figure 2.10) has been chosen because of its similarity to the cross section of the real bird wing. Following a similar process to the creation of the seagull wing, the solid model has been created on *CAD* software *Solidworks 2011.* The main difference is the leading edge of the wing. This is in fact a straight line, instead of having a bio-mimetic shape. First simulations and improvements have been done on the simplified geometry, shown in Figure 2.11.

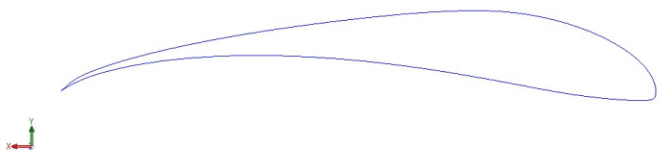

Figure 2.10: S1223 Selig Airfoil.

A particular addition to this version of the wing is the static twisting of the wing. An analytical law of twist defines the angle of which the cross sections are rotated with respect to the root section (Figure 2.12). The adjective "static" referred to the twisting underlines the difference with the *dynamic twisting*, which is a specifically controlled movement of the wing in time on the same axis.

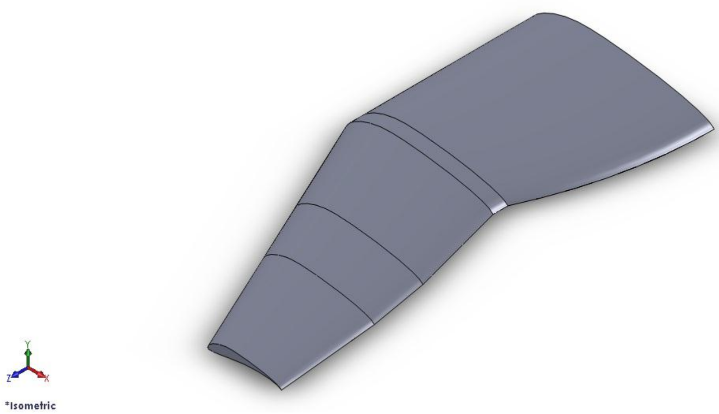

Figure 2.11: Selig wing (isometric view).

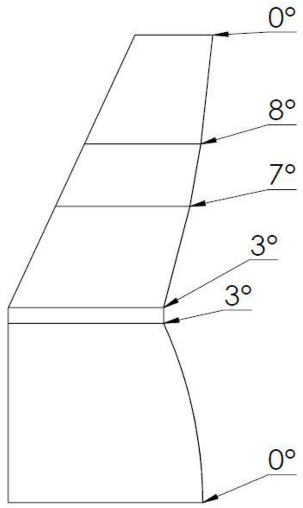

Figure 2.12: Twisting function.

2.2.3 Fuselage and tail

A body for the *Skybird* is as necessary as all the other parts of the *UAV*. Inside the fuselage all the avionic devices, the power sources and the kinematic train have to be located. The external shape though, has to be aerodynamic as much as possible. A sequence of *CFD* simulations has been done to test the different lengths and proportions of a fuselage with a simple shape. The best performing fuselage is shown below in Figure 2.13.

As far as the tail was concerned at the moment, a simple V-shape tail has been mounted on the fuselage. The *NACA0012* airfoil has been used to create a first-attempt tail. More sophisticated tails have been considered I the thesis by Ghelardi [12] where flight stability considerations in gliding flight have led to the development of an "optimal" tail.

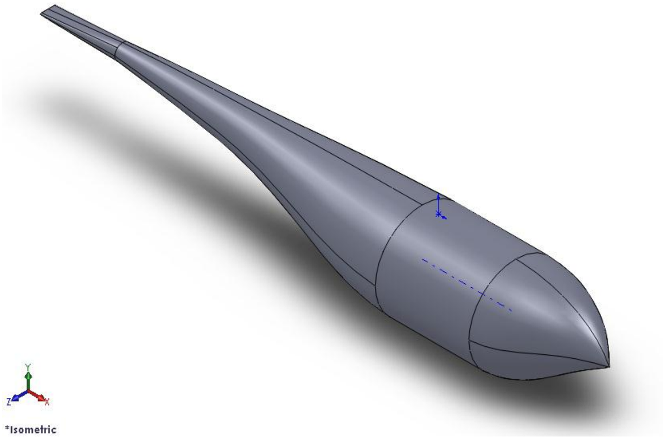

Figure 2.13: fuselage of the Skybird.

2.3 Flapping wing study

2.3.1 Introduction to flapping wing flight

Engineers and inventors have been inspired by looking at the birds for years and years. Flapping wing flight not only is a fascinating aspect of the dream of flight, it is also very interesting from an engineering point of view. It is actually able to produce a very high lift at incredibly low Reynolds number flows [13]. Obviously flapping wings produce a kind of lift which is a periodic function in time (Figure 2.18, for example). However, the average lift on a period is a positive value, and increasing the frequency means increasing the power generated. Hummingbirds are just an example of how nature can provide to the human sight exceptional mechanical systems. Flapping though is only one of the different movements that birds perform during flight. Generally, there are four degrees of freedom: *flapping, lagging, feathering* and *spanning.* The *lagging* motion is the rotation about the vertical axis. It is not very important on flight, whereas it is crucial to control to distribution of weight during the operations of take-off and landing. However, this is not a requirement for the *Skybird* and this aspect is going to be neglected. The *spanning* is instead very important to increase performances. This is the relative motion between inner and outer wings, i.e. the relative rotation between the two rigid parts of the wing. Figure 2.15 shows the two most important displacements of the wing: *flapping* and *feathering* (in this context also known as "*dynamic twist").* Our focus will be then displaced on these two movements. Once the geometry has been created, the industrial *CFD* software "*Ansys Fluent R14"* [14] has been used to perform numerical simulations of the aerodynamics. It was necessary to create a fluid domain around the object to simulate large enough with respect to scale of influence of the presence of the body. Then, with the aid of the toolbox "*Ansys Mesher"* the fluid domain has been divided into a finite volume grid, on which the conservation equations have been integrated.

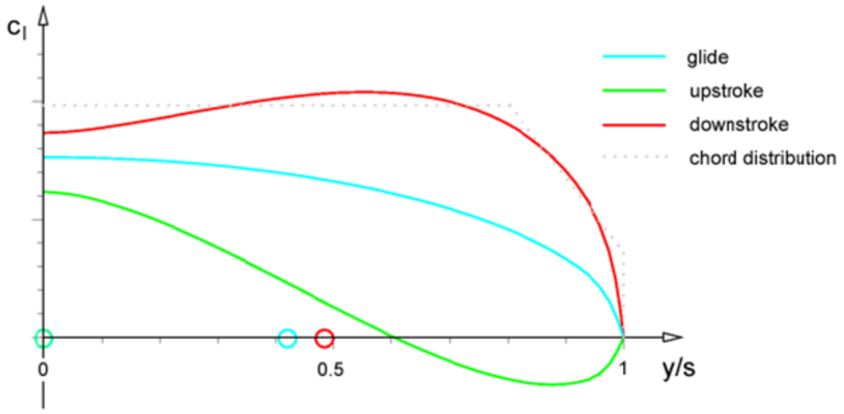

Figure 2.14: Lift coefficient distribution over the wing span, during *upstroke* and *downstroke*.

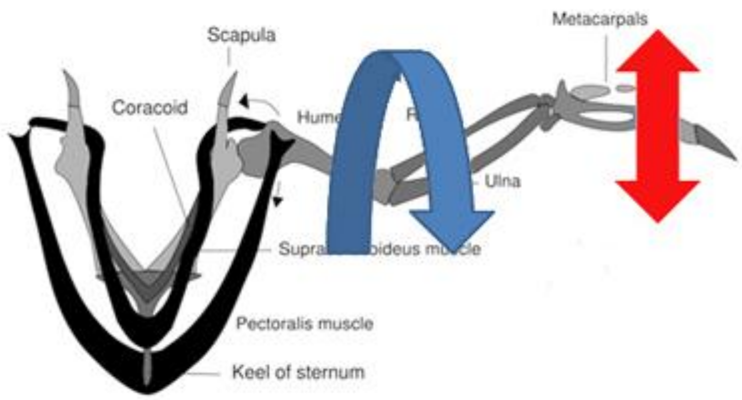

Figure 2.15: Dynamic twist (blue arrow) and flapping (red arrow).

2.3.2 Dynamic meshes

Since the aim of the simulations is to virtually recreate the flight of the *Skybird*, a particularly complex concept has to be applied to the simulation. It is called "*dynamic mesh"* and it deals with domains of fluid having borders which change in time. The flow indeed sees the object as a wall with its shape; the air overcomes the obstacle generating a distribution of pressure all over the body. The wings of the *Skybird* are moving though, and consequently so does the domain. Thus, the mesh of tiny elements is different for each moment in time. Time is discretized into small portions, the so-called *time steps.* The engine runs a steady simulation each time step and coupling all of them an almost continuous solution turns out. Obviously the accuracy of the solution is depending on the number of iterations on each *time step* and also on the duration of the single *time step.* Then, the domain moves, and the grid follows it according to meshing algorithms. It can also be set a recreation of the mesh after a certain number of *time steps*. This is because essentially the mesh is stretched using an algorithm which treats the cell edges as springs. Before the mesh quality drops to low values, the grid is generated again instead of just being stretched.

2.3.3 User Defined Functions (*UDFs*)

The so called *UDF*s are the programming codes which have the role to control to motion of the moving surfaces. They are usually written in *C* language and they need some reference points into the mesh. For this reason, all the reference systems of the *CAD* drawing, the solid model and the mesh have to match on the same point. This type of *UDF* is generally fitted to include motions about three different axes: *roll, spanning* and *pitch.* The *frequency* of the *flapping* is another variable which can be adjusted as preferred.

However, this program is suited to move a rigid wing. Later on in next chapter, the *UDF* for the articulated wing, much more mathematically complicated but also necessary to advanced design, will be presented.

2.3.4 Result data

Hereafter, an overall summary of the results dealing with simulation cases tackled in next chapter will be shown. The base geometry has been the Selig wing without twist, as shown below in Figure 2.16 and Figure 2.17. This wing is also called “sufficient” wing, since its rigid flapping at 5 *Hz* guarantees enough lift to sustain the theoretical *payload* of the *UAV*.

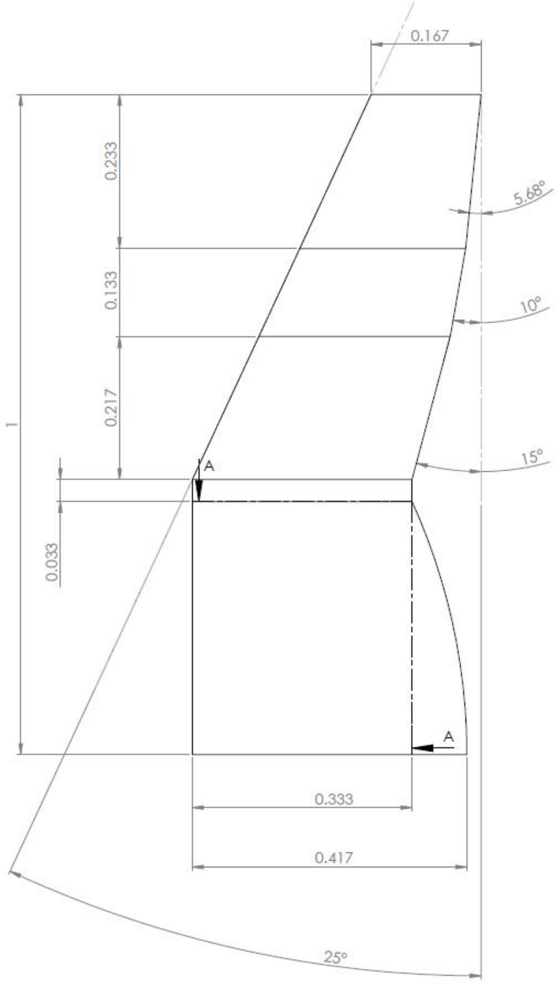

Figure 2.16: Selig wing planform dimensions.

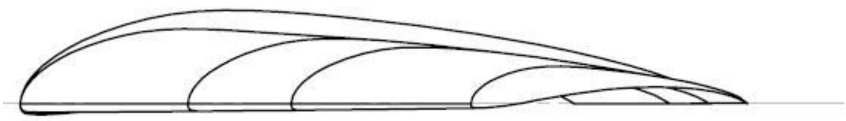

Figure 2.17: Side view of the "sufficient" wing.

In Table 4, parameters and outputs of two simulations involving a rigid flapping wing at two different frequencies are shown. It has to be noticed the crucial effect of the frequency on *thrust* and lift performances. At *3 Hz* the lift produced is not enough to carry the weight of the body, whereas raising the frequency to 5 *Hz* values are definitely satisfying. We have to remember that this is a rigid wing case and performances are widely affected by the negative lift during the *upstroke*.

Flight velocity ***U***	***5 m/s***	***5 m/s***
Flapping frequency ***f***	***3 Hz***	***5 Hz***
Flapping angles	*Upstroke 45° - Downstroke 15°*	*Upstroke 45° - Downstroke 15°*
Flapping amplitude **ϕ**	*60°*	*60°*
Wing surface	*0.3135* m^2	*0.3135* m^2
Average aerodynamic chord $\mathbf{C_m}$	*0.335 m*	*0.335*
Average lift	***2.8948 N*** *(*$C_L \approx 0.60$*)*	***6.2266 N*** *(*$C_L \approx 1.30$*)*
Average Drag (negative drag means positive thrust)	***- 0.5697 N***	***- 3.2508 N***

Table 4: Parameters and performances at 5 m/s.

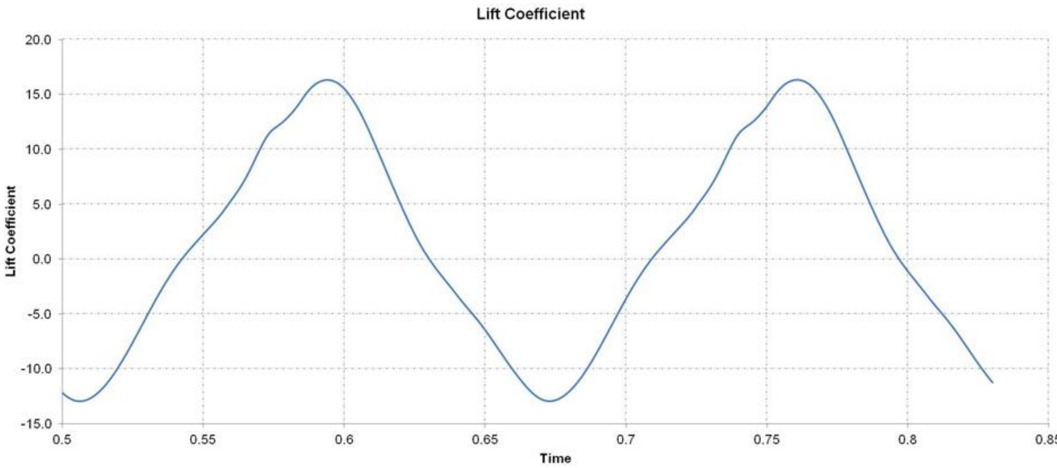

Figure 2.18: Lift coefficient at 5 m/s, 5 *Hz* and rigid flapping wing as function of time. Two periods of oscillation are displayed.

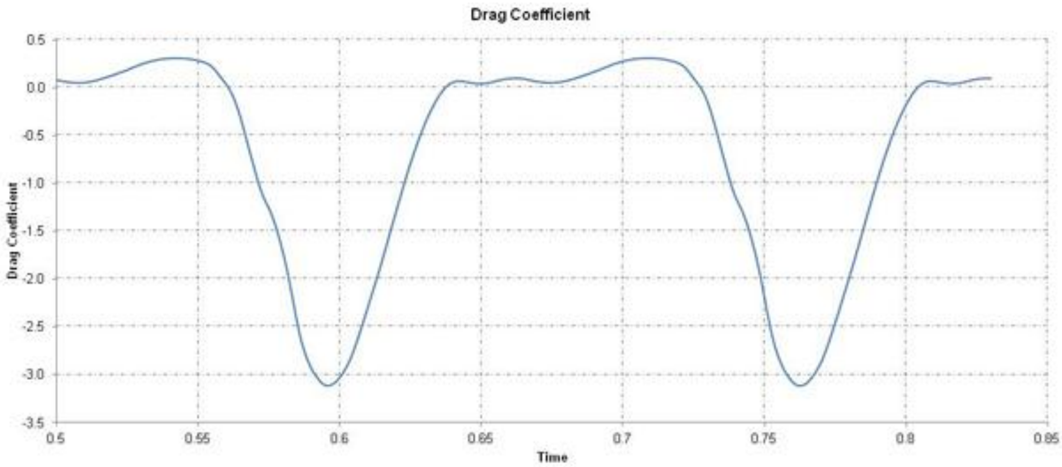

Figure 2.19: Drag coefficient at 5 m/s, 5 *Hz* and rigid flapping wing as function of time. Two periods of oscillation are displayed.

As said before, introducing a dynamic pitching function can increase performances very much. Below, some results taken from Carlo Pacioselli's Thesis [15]:

wing with no twist	roll +30°,-30° pitch 0° caso (1)		roll +30°,-30° pitch +5°,-5° caso (2)	
velocity (V) [*m/s*]	5	5	5	5
frequency (F) [*Hz*]	3	4	3	4
lift force (L) [*N*]	2.9796	4.0918	2.968	3.9507
drag force (D) [*N*]	-0.5841	-1.2985	-1.1698	-2.2917
sideslip force (S) [*N*]			-0.1529	0.0816
Strouhal n. (ST)	0.3	0.4	0.3	0.4
reduced frequency (K)	0.63145959	0.84194612	0.63145959	0.84194612

wing with no twist	roll +30°,-30° pitch +10,-10° caso (3)	
velocity (V) [*m/s*]	5	5
frequency (F) [*Hz*]	3	4
lift force (L) [*N*]	2.8932	3.9526
drag force (D) [*N*]	-1.6524	-3.1572
sideslip force (S) [*N*]	-0.685	-0.6902
Strouhal n. (ST)	0.3	0.4
reduced frequency (K)	0.63145959	0.84194612

Table 5: Simulation results showing the effect of the pitching movement on performances.

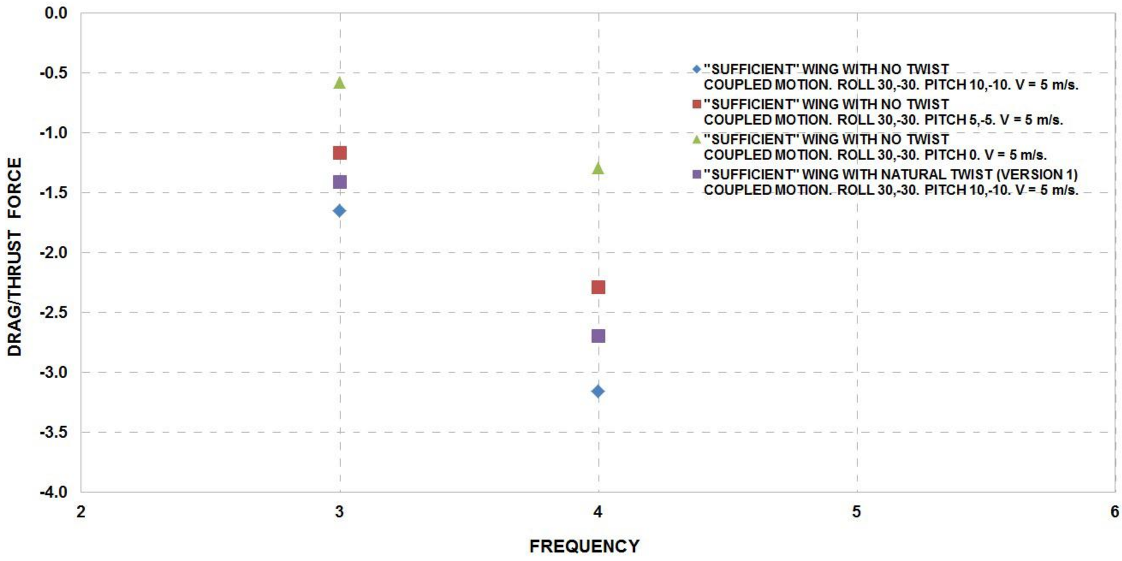

Figure 2.20: Drag/thrust chart as function of frequency for 4 studied cases.

Last considerations about the “optimized wing”, taken from [16], will be the starting point of the actual development process described by this report.

3. Wing improvements

After an introduction on the whole project, the purpose of this study will be tackled. So far, all the improvements and development have led to a version of the *Skybird* with a simplified geometry. However, the advanced step of the design focuses on more complicated and more efficient aerodynamic surfaces. Hereafter the very last considerations of the previous design are presented. They are taken by Report to Selex #4 [16] and analyzed in each point throughout this Chapter.

3.1 Introduction and starting point of the development

3.1.1 Considerations on optimized wing

The wing described in section 2.3.4 provides lift enough to sustain the *Skybird* in leveled flight at all considered speeds; at low velocity it is necessary a sufficiently high flapping frequency whereas at high speed the lift provided is largely more than required. It has also to be noticed that high frequencies induce peaks on lift function (±70 N) [17] potentially dangerous for structure and flight stability. Below some of the guidelines which lead from the *"sufficient wing" (sw)* to the *"optimized wing"* function of time.

1. **Reduction of the wing surface**: reducing the *chord* length to 70% and the *wing span* by the same factor results in a *wing area* reduced of about the half. Assuming that aerodynamic coefficients do not vary too much since the geometry is similar, forces into play are reduced by a factor of 2. So are wing oscillation amplitude and peak loads. There is still the issue about the lift generation which decreases proportionally with *wing area* (from 2.895 N to 1.45 *N* at 3 *Hz*). However, this can be overcome introducing advanced solutions such as natural twist or the articulated wing.

2. **Flapping angle optimization:** so far we have usually considered a total *flapping angle* equal to Φ = 60°, divided in 45° in *upstroke* and 15° in *downstroke.* Even though this configuration gives a generous thrust, they are weaker in producing lift. Configurations closer to the symmetric one are then preferable from this point of view. Studies led by others [13], [18], [19] have shown how lift is barely affected by the flapping angle. This would suggest reducing the *flapping angle* in order to reduce mechanical loads. However thrust is reduced as well. Thus the optimal situation is to increase the oscillation of the wing during low speed flight to maximize thrust, whereas a small angle Φ is sufficient to provide lift at high speed if combined to a higher frequency to increase thrust. All this is referred to the rigid wing. A particular dissertation about the relative roll angle between inner and outer wing of the articulated one will be presented later on (cf. section 3.2.1).

3. **Twisted vs. non twisted wing:** Figure 2.20 and Figure 2.21 show how lift generation is much higher for twisted wing; thrust is a bit lower for low speed though. A downscale of 70% of the dimensions and natural twist applied to the wing should be the best solution to guarantee thrust, especially at low speed.

4. **Dynamic pitching during swing:** coupling a *flapping* motion with a dynamic *pitching,* translates into an advantage in thrust production, for a little loss in lift. This choice is clearly necessary to produce thrust flying at high speed using low flapping frequencies. (cf. reference [6], Festo video clip, http://www.youtube.com/watch?v=kA7PNQiHT1Q)

5. **Round tips or *deployable winglets* devices:** an increase of the thrust can be produced by reducing the drag. Turbulence vortices at the wingtip can be partially removed and thus increase performances. During the advanced design elliptic shapes at the wingtips will be considered to reduce induced drag and also biomimetic inspired winglets [34] (cf. sections 3.3 and 3.4).

6. **Articulated wing:** last but not least is the possibility to design a wing divided into two pieces. This solution must improve performances much, since the down force during *upstroke* is reduced by the folding wing. Accurate results will be given after numerical simulations. Much more complicated mathematical function to describe motion are required (cf. section 3.2.1), however, as it will be shown later on, this will be the biggest improvement from the point of view of the flight performances. Lastly, it must be said that for simulations involving “complex kinematics”, *Strouhal* number is equal to 0.3; which is the optimal value for the best thrust efficiency ([35], [36]).

3.1.2 Standard base configuration *“0.0”*

All the experimental processes need a reference point. In other words, it is necessary to have available data of a standard case to which we can relate the results of the customized cases. To accomplish this task, the case usually called *“0.0”* has to be free from everything which differentiates each other case of study.

3.1.2.1 Geometry definition

As shown below in Figures 3.1, 3.2 and 3.3 the base configuration is supported by a revised geometry. Fuselage is the same as the one mentioned in section 2.2.3. A quite wide set of simulations was run and it pointed out the fuselage most “penetrating” into the air; in other words, the geometry associated to the lowest C_d coefficient. A shape able to fit inside all the devices and kinematics was not a requirement at that point of the study though. Since this study is still focused only on aerodynamics, the same simple cylindrical based shape is used. The only attention has been directed to its dimensions, which are roughly the definitive ones. They are in the order of *1 m* (see Figure 3.1). As far as the tail is concerned, it is freely inspired by the *Festo Smartbird* one [6]. *Solidworks loft* functions envelop volumes between different planes inclined as much as the sections move away from the symmetry plane (Figure 3.2). The base profile is a *NACA0004*. It is a thin and symmetric airfoil frequently used for tales of aircrafts. A small vertical rudder can be noticed in the side view (Figure 3.1). Few approximate simulations have been run using the software *"Tornado"* [20]. It is based on *VLM* (Vortex Lattice Method), where aerodynamic surfaces are modeled as thin layers of micro vortices. It does not take account of the viscosity of the fluid [21], but it gives a first order idea of the response of a three-dimensional geometry. In this case the assembly of tail and rudder gives a decent flight stability, but definitely improvable. Lastly, the focus is oriented on the wing arrangement. The non-twisted Selig airfoil has been scaled to have a *wing span* of 1*m*[1], as can be noticed from quotes in Figure 3.2 and Figure 3.3. Then, an adjustment of the solid model is needed. It concers the *dynamic mesh* of the flapping wing; a gap between two parts of the wing is necessary. The reasons of the creation of this void space are explained in the dedicated session 3.1.2.2.

As far as the geo-kinematic parameters are concerned, the flapping frequency is adjusted to *3 Hz*, whereas angles of flapping are *±30°* for inner wing and *50°* of relative rotation at the articulation. Both angles are referred to the horizontal axis, as further explained in section 3.2.1

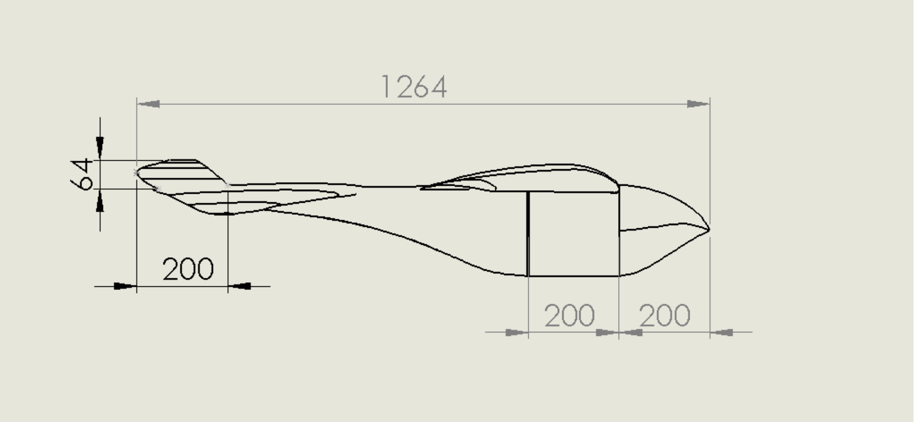

Figure 3.1: Side view of the *Skybird.*

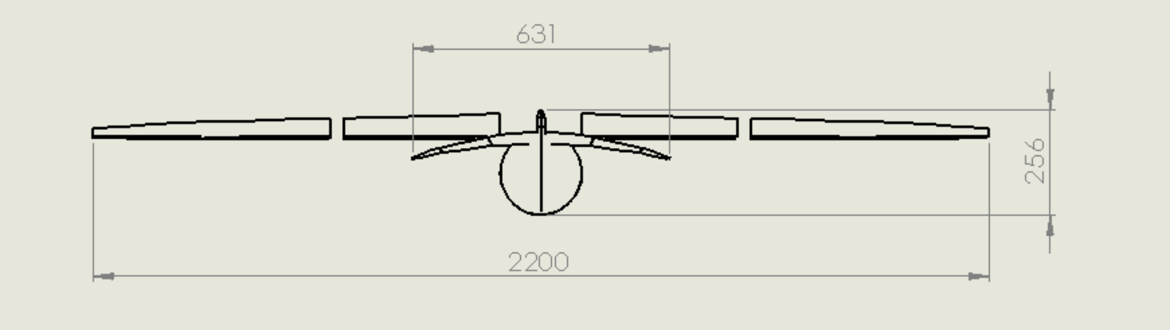

Figure 3.2: Front view of the *Skybird.*

[1] Wing span is referred to a single wing. The total wing span is equal to *2.2 m*.

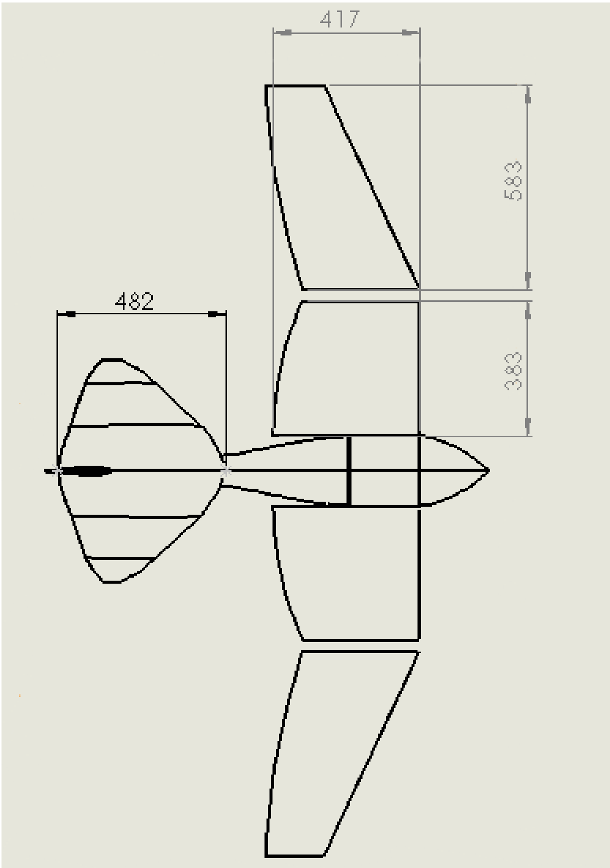

Figure 3.3: Top view of the *Skybird.*

3.1.2.2 Articulated Flapping Wing (AFW)

The articulated wing is the first big introduction in the advanced design. The goal of this solution is to recreate the joint of an actual bird wing. What is then the advantage in using such system? The answer is situated in the shape of the lift as function of time. Lift oscillates from negative to positive values during flapping. Even though the airfoil shape of the wing produces a part of the lift, only a small portion comes from there. Dynamic pressure on the wing is the origin of the substantial portion of the lift. If the *downstroke* of the wing provides an effective lift, during *upstroke* a *downforce* is induced to the *UAV*. The aim of the *AFW* is to reduce the projected area during *upstroke* in order the reduce the drag on it. This results in a total *downforce* reduction and, ultimately, the magnitude of the averaged lift on a period rises. It does by a factor of almost *2* since averaged lift goes from *2.89 N* for the rigid wing case (cf. section 2.3.4) to approximately *5 N.* The articulation of the wing is situated on the axis shown in Figure 3.4 and Figure 3.5. It is directed towards the line of flight and located *400 mm* far from the base profile. Then the wing has been split in two parts at *40%* of the *span* from the *base chord*. As can be seen in Figure 3.4, inner and outer wings are actually *17 mm* shorter, in order to leave a free space around the axis of rotation. This has been done because of simulation requirements; this *3 cm* gap indeed prevents inner and outer wing volumes to intersect each other during relative motion, as shown in Figure

3.5. Otherwise, that would represent a fatal error in the solution process since the intersection would be recognized as a negative volume.

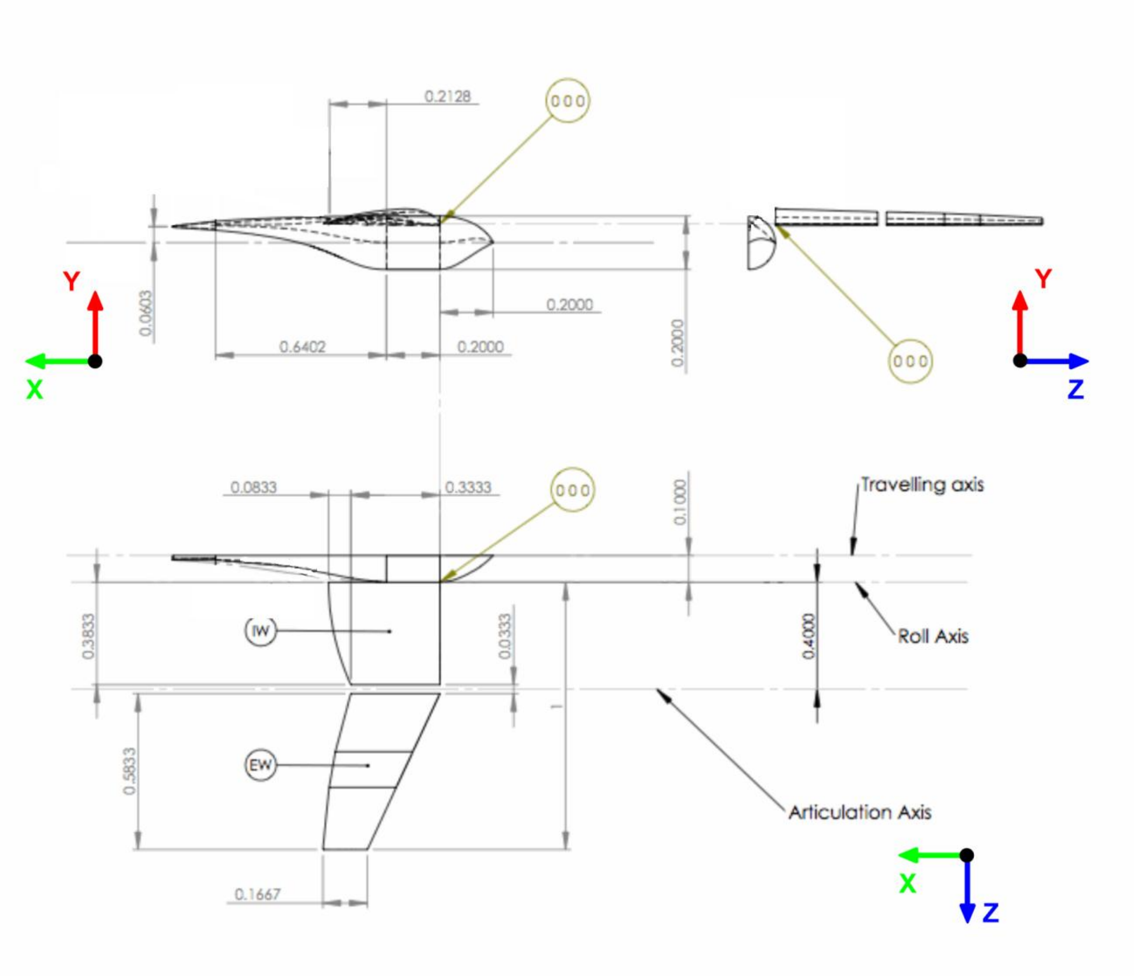

Figure 3.4: Projections of the *Skybird* with labeled axes and reference origin (tail not displayed).

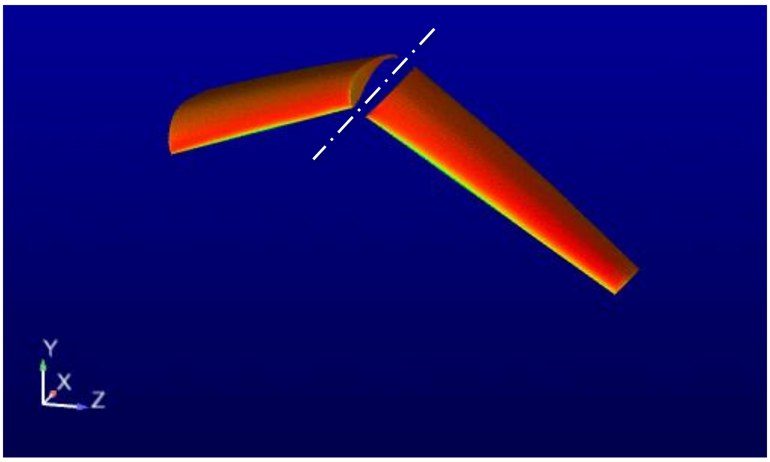

Figure 3.5: *Skybird* wing during *upstroke.* White dash line is the axis of relative rotation.

3.2 Relative roll angle optimization

The kinematic code which controls the articulation is quite complex. Thus, before starting to expose the set of simulation performed, an introduction to the *User Defined Function* of this case is tackled.

3.2.1 *AFW* User Defined Function

First of all, a reference system has to be assigned. This does not only mean to fix a *(0, 0, 0) point* to which refer geometry and kinematics, but also two parts of the wings have to be controlled as rigid bodies moving in the space. This case involves two rigid rotations about two axes, one of them fixed, while the other is moving. Then, it is enough to determine a point inside the body and its kinematics can be controlled by simple or combined trigonometric relations. Below, all analytical descriptions of the flapping wing based on reference point are expressed. They refer to Figure 3.6 and Figure 3.7.

- O, general *(0,0,0)* point and root pivot
- A, connection of semi-wings or generically a point on the joint axis
- C, the arbitral reference point in the outer wing volume
- θ_{in} the angle formed by the inner wing with the horizontal, $\theta_{in} > 0$ the wing flaps down
- θ_{out} the angle formed by the outer wing with the horizontal, $\theta_{out} > 0$ the wing flaps down
- θ_{rel} the relative angle between wings
- L_{OA} the distance between the connection and the main pivot
- L_{CA} the distance between the outer reference point and A
- β_A the angle between $\overline{OA}$ and the horizontal, $\beta_A > 0$ -> A is *lower* than O
- β_C the angle between $\overline{CA}$ and the horizontal, $\beta_C > 0$ -> C is *lower* than A

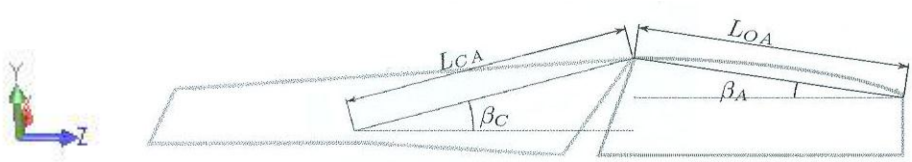

Figure 3.6: Initial configuration of the wing, with both semi-wings horizontal.

In the equations (3.1) the basic geometric relations used to define the position of the wing are recalled. The *z-axis* is horizontal and *y* is the vertical axis.

$$\begin{cases} \beta_A = -arctg\left(\frac{y_A - y_O}{z_A - z_O}\right) \\ \beta_C = -arctg\left(\frac{y_C - y_A}{z_C - z_A}\right) \end{cases} \tag{3.1}$$

which are constant during the motion, as a consequence of the rigidity of the semi-wings. The dynamic position of the wing can be completely defined as a function of θ_{in} , θ_{rel} and the following relations (3.2)

$$\begin{cases} \theta_{out} = \theta_{in} + \theta_{rel} \\ y_A = y_O - L_{OA}\sin(\theta_{in} + \beta_A) \\ y_C = y_A - L_{CA}\sin(\theta_{out} + \beta_C) \\ z_A = z_O - L_{OA}\cos(\theta_{in} + \beta_A) \\ z_C = z_O - L_{CA}\cos(\theta_{out} + \beta_C) \end{cases} \tag{3.2}$$

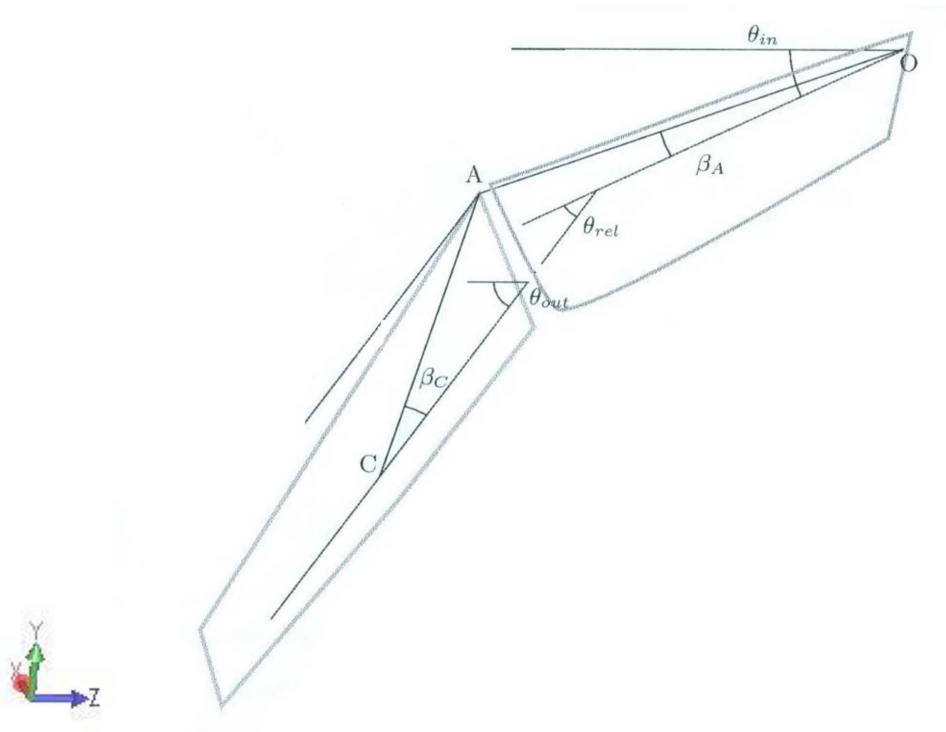

Figure 3.7: Generic configuration of the wing (proportions changed for clarity).

Next step is to write a code in a *C* programming language to be compiled and eventually read by the fluid solver. It consists of several pages of commands which include explicit and editable parameters. The crucial ones are the flapping *frequency* and the *amplitude* of the oscillation of the two semi-wings, expressed, respectively, in *Hz* and *degrees*. Some extracts of it are shown in the following Code 3.1 and Code 3.2.

```
DEFINE_CG_MOTION(motion_extwing, dt, v_cg, omega, time, dtime)

{

        Thread *t;
        face_t f;
        real NV_VEC (A);

        frequency = 3.0;        /*frequency in hetrz*/

        pi = 3.141592654;       /*pi*/

        /* define motion variables */

        Ar   = 30.0;  /*roll  amplitude of internal wing*/
        Ar2  = 30.0;  /*roll  amplitude for external, this amplitude is not related to the expression to compute roll2 implemented in this function*/


        Arolldif = 50.0; /*roll  amplitude between wings, this amplitude is used to compute roll2 implemented in this function*/


        Ap   = 0.0;  /*pitch amplitude*/
        Ay   = 0.0;  /*yaw   amplitude*/

        Aroll     = Ar*pi/180.0;        /*conversion to radians*/
        Aroll2    = Ar2*pi/180.0;       /*conversion to radians, roll  amplitude for external, this amplitude is not related to the expression to compute roll2
implemented in this function*/
        Arolldif  = Arolldif*pi/180.0;  /*conversion to radians*/

        Apitch = Ap*pi/180.0;    /*conversion to radians*/
        Ayaw   = Ay*pi/180.0;    /*conversion to radians*/

        w=2.0*pi*frequency;                     /*omega (radians)*/
        T=1.0/frequency;                        /*period*/
```

Code 3.1: Parameters definition section of the *UDF*.

```
/*WING GEOMETRIC DEFINITIONS*/
lint = 0.38333333;
lgap = 0.03333333;
lext = 0.58333333;
lcg  = 0.23333333;
/*WING GEOMETRIC DEFINITIONS*/


/*ROLL DEFINITION*/
/*THIS IS THE ROLL ANGLE OF THE INTERNAL WING AND ITS HAS TO BE EQUAL TO THAT IN THE DEFINITION OF THE INTERNAL BODY ROLL MOTION*/

roll    = Aroll*sin   (w*time + 0.0*pi/2.0);
droll   = w*Aroll*cos(w*time + 0.0*pi/2.0);
```

```
/*ROLL DIFF DEFINITION*/
/*THIS IS THE DEFINITION OF THE ROLL ANGLE BETWEEN WINGS*/

/*0 for rigid case*/
/*
rolldif         = 0.0;
drolldif        = 0.0;
*/


/*DEF1*/
/*
rolldif         = 1.0*Arolldif*sin   (w*time + 0.0*pi/2.0);
drolldif        = 1.0*w*Arolldif*cos   (w*time + 0.0*pi/2.0);
*/


/*DEF2*/
/*rolldif               = -0.523829*Arolldif*erf(1.414213562*cos(w*time));*/
```

Code 3.2: Definition of the roll angles for both semi wings.

3.2.2 Optimization process

This section gives an overview on the results of few extra simulations about the relative flapping angle. A full set of simulations has been already run. First three cases, shown in Table 6, experience a variation of the relative flapping angle.

CASE	A Internal wing	A External wing	B[2]	C[2]
NF1	30°	40°	4.0	0.6266
NF2	30°	50°	4.0	0.6266
NF3	30°	60°	4.0	0.6266
NF4	30°	50°	1.0	1.1963

Table 6: Kinematic behaviors for different angles.

The inner wing flapping angle is fixed to *30°*, since it seemed to be the best compromise between performances and induced structural stresses. As it can be seen from Table 6, cases *NF1, NF2* and *NF3* are connected to three different kinematic configurations, whereas numerical coefficients are kept constant. A results chart is presented below for *30°, 40°* and *50°* cases.

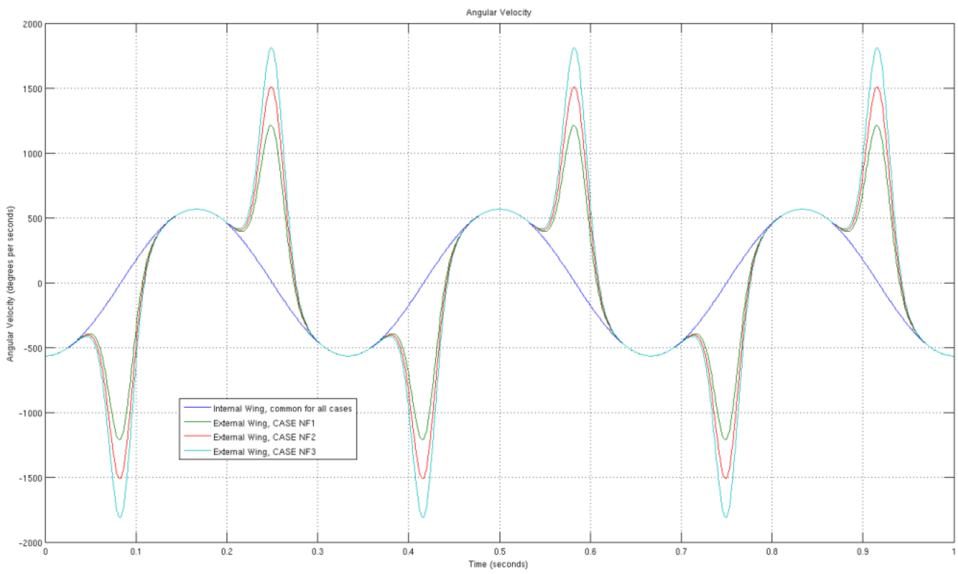

Figure 3.8: Angular velocity evolution of inner and outer wings for different cases.

From these figures it can be seen that in cases NF1, NF2 and NF3 most of the time during the *downstroke* the internal and external wings are aligned. However, this kind of configuration tends

[2] *B* and *C* coefficients refer to the flapping motion function of the external wing (called roll.e.w):

$$rollew = -\frac{A \times \sqrt{\frac{\pi}{2}} \times Erf(\sqrt{2} \times \sqrt{B} \times cos(w \times time))}{2 \times \sqrt{B} \times C}$$

to produce high loads on the wing when it changes direction. This behavior certainly produces high loads when the wing is rotating, which could negatively affect the structural integrity and stability of the Skybird.

The *B* and *C* coefficients which compare in Table 6 are two of the numerical values of the analytical expression of the kinematics. In case NF4, they are varied to try a different balance of the equation. By reducing the time when two semi wings are aligned, the function in Figure 3.9 presents a smoother behavior compared to case NF2.

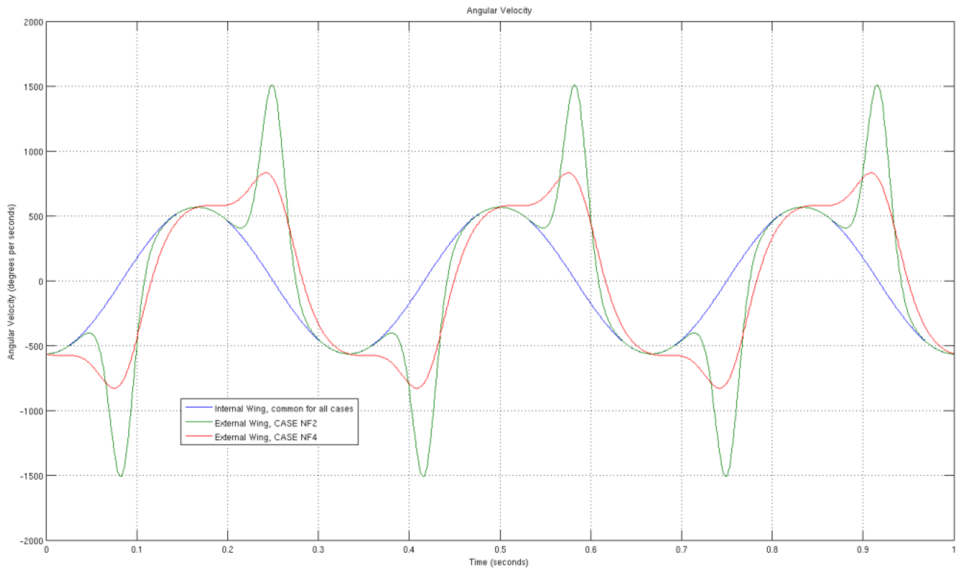

Figure 3.9: Comparison between case NF2 and NF4. They use same angles but different coefficients.

Since loads are more affordable for last case, kinematics NF4 is preferable than the other ones. It will be the standard configuration for next simulations.

The main concern now is to look more closely on how aerodynamic coefficients vary for cases presented below in Table 7.

CASE	A Internal wing	A External wing	B	C
NF5	30°	45°	1.0	1.1963
NF6	30°	50°	1.0	1.1963
NF7	30°	55°	1.0	1.1963

Table 7: Kinematic behaviors for different angles and updated coefficients.

Case NF4 preserves same angles of case NF2. Thus, it can be interesting to look for the behavior of the system around the values of *50°* of relative roll angle.

For charts and comments on results the reader is referred to Chapter 5, section 5.2 and Chapter 6.

3.3 Study on the wingtips

3.3.1 Aerodynamic phenomena on the wings

Several phenomena take place on a flying wing. Lift is obviously the most important, since the wing and the airfoil are designed to produce it. A high pressure zone is created under the wing to sustain the body. As can be seen in Figure 3.10, the wing trail is an area characterized by a *down-wash* velocity. However, the conservation laws applied at the tips reveal that an opposite phenomena must interest the zone right beyond the tips. It is called *up-wash* velocity. Birds, for instance, use to fly in V-formation in order to earn an extra lift, coming just from the *up-wash* zone induced by the flight of the bird ahead.

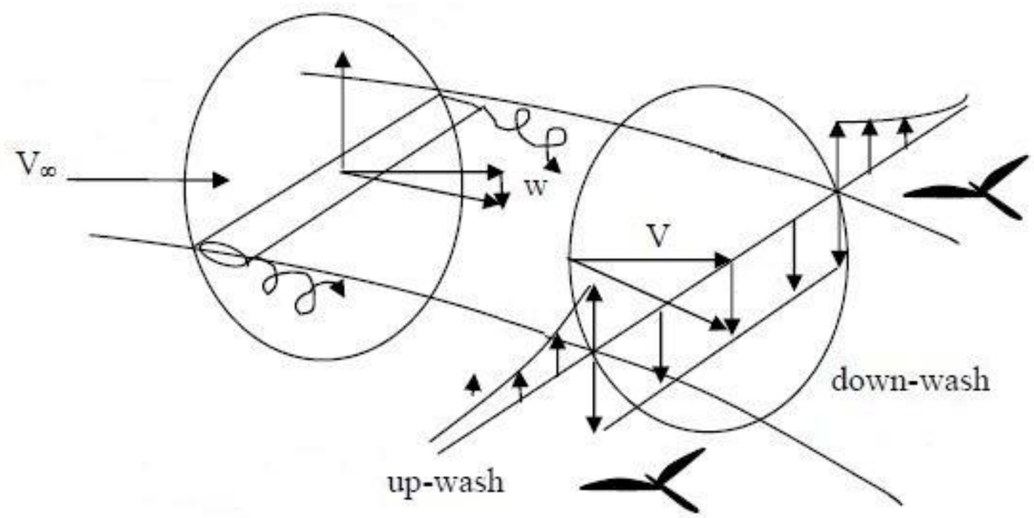

Figure 3.10: Sketch of *up-wash* and *down-wash* zones around a wing trail.

Anyway, pressure drops suddenly on the edge of the wing; the gradient of pressure creates a "suction" of air from below to above the wing. This is simply what happens when a stone is dropped into the water; the fluid is moved away from the bottom of the object and it tries to cover it again with a circular motion as soon as it starts sinking. For the case of a flying object, this particle motion is combined with a linear velocity. Thus, they results in a three dimensional motion with a spiral-like trajectory (Figure 3.11). This is the point where the efficiency of the flying system is involved. Turbulent flows are a sink of energy; in other words, power is dissipated by frictional work between fluid particles. This fact is usually called *induced* drag, since it is a cause of energy waste, but actually induced by a phenomenon which is not the dynamic pressure of the colliding particles on the leading surfaces. Next section will present possible solutions to this problem in order to increase wing efficiency.

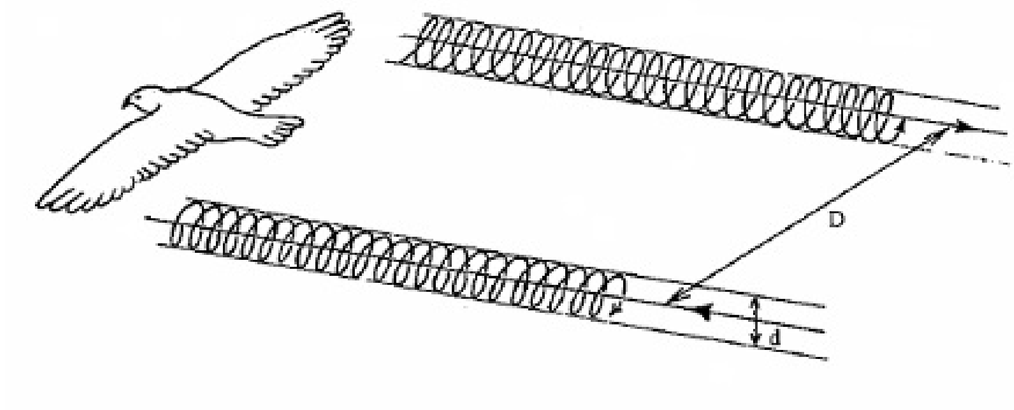

Figure 3.11: Wing tips induced vortexes.

3.3.2 Devices to improve performances

Once the origins of a physical event have been understood, the solution to prevent it from happening comes consequently. In this case, if the pressure gradient at the wingtips was reduced or even canceled, the arrival of the turbulence phenomena would be reduced as well. With a further step back, it can be pointed out that lift is closely connected to pressure variation. The use of a twisted wing comes from this concept. For every airfoil there are charts which express the lift coefficient as function of the angle of incidence of the wing. If the end profile is rotated with respect to the root section by the angle such that it does not produce any lift, theoretically turbulence vortices at the tips are avoided.

Another solution, shown in Figure 3.12, is the so-called *elliptic wing.* Introduced in World War II in fighters[3], it is based on a feature of the lift function. Lift is in fact a function of the local *chord length.* At least ideally, it presents a zero value on the tips, for wings ending with a convex curve. Zero value of lift, means no local *downwash* velocity and thus no induced drag. It is also possible to deal with a *tapered* wing. If the *chord length* is reduced going away from the base profile, the turbulence at the tips is at least reduced, without losing the original shape of the wing.

[3]One of the most representative aircraft with the elliptic wing planform was the *Spitfire*, in force of the *British RAF* during World War II. A curiosity stays in the fact that this particular shape of the wings did not come from aerodynamic studies to improve performances. British engineers instead needed extra space to fit strengthening bars into the wings to sustain machine guns.

Figure 3.12: Elliptic wing planform.

Finally, winglets are the last method exposed here to avoid problem of induced drag. They are widely used in modern airplanes, as it can be seen in Figure 3.13. Their task is to keep separated the two flows above and below the wing, until a point where they are characterized by a similar pressure. This prevents the creation of suction phenomena from low-pressure to high-pressure zones. It is essentially the idea which inspires two previous solutions. However, this is more efficient and stable than the other ones for some reasons. The twisted wing is efficient as long as the flight is leveled, but when the angle of attack changes, it makes the value of the lift at the tip different from zero. Winglets are an extension of the wing, but they do not present an airfoil cross section and thus lift produced is very small. In Figure 3.13 wingtip *fences* on different commercial aircrafts are shown. They are mounted vertically at the tip of the wing and they are designed to stop the whirling motion of particles to reduce the strength of the wingtip vortex (Figure 3.14).

Figure 3.13: Different kind of winglets mounted on Airbus airplanes.

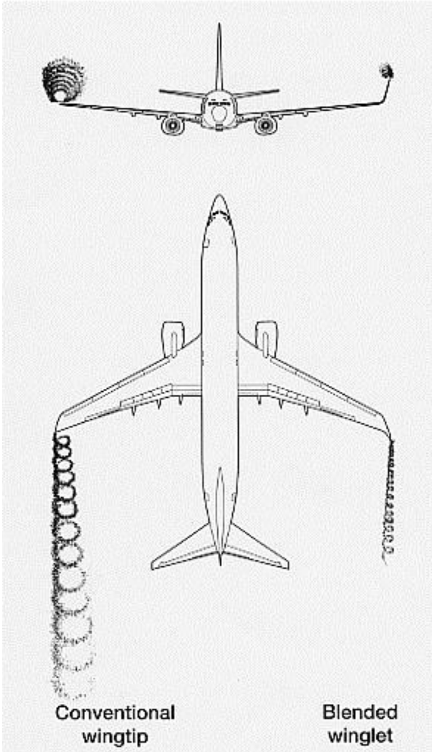

Figure 3.14: Effects of the winglet on the wingtip turbulence.

As far as the respective solution of Nature is concerned, birds are provided of sort of winglets as well. Raptors, for instance, have long feathers at the tips bent upwards to reduce turbulence and eventually save muscular efforts (Figure 3.15). Sea birds instead have usually pointed wings. They use two of the few methods explained above to reduce drag in flight. However, it must be made a distinction between airplanes and birds. First ones deal with rigid wings and, except from turbulent zones, quite stable flows. Birds glide sometimes too, but they usually thrust themselves by flapping their wings and they are in a completely different situation. Theory has been widely developed and the applications work perfectly for high Reynolds number flows and for a rigid wing such as the airplane ones. On the contrary, flapping wings are not a much explored field and neither the behavior of a wingtip in that context has been much studied. Next chapter will present the geometries on which *Skybird* simulations have been run.

Figure 3.15: Osprey in flight.

3.3.3 Geometries creation

Consequently to what said before, it has been decided to work on the base geometry of the wing shown below in Figure 3.16. Three geometries for the tips have been generated with the aid of the *CAD* Software *“Solidworks 2011”.*

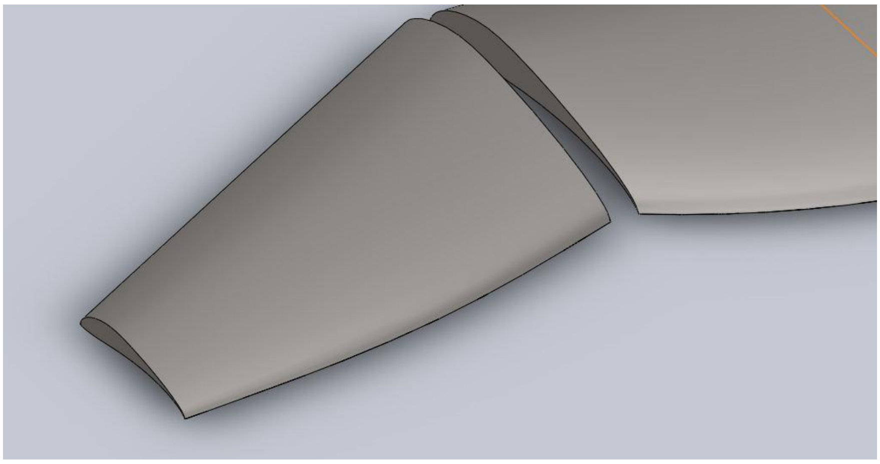

Figure 3.16: Base wing with no wingtips.

3.3.3.1 Tip #1

First geometry is a small step forward with respect to the basic one. The idea is to get rid of the sharp edge which characterizes the geometry “*0.0*”. Figure 3.17 shows the fillet on the upper edge of the wing tip. It has been generated using the *Solidworks* function “*edge fillet”.* This addiction preserves the *1 m* length of the original wing. The idea is to prevent the formation of high strength vortexes by smoothly connecting different surfaces. It is expected a value of the lift slightly higher. This is because the flow should overcome the wing during the *upstroke* a bit easier than moving around a sharp edge.

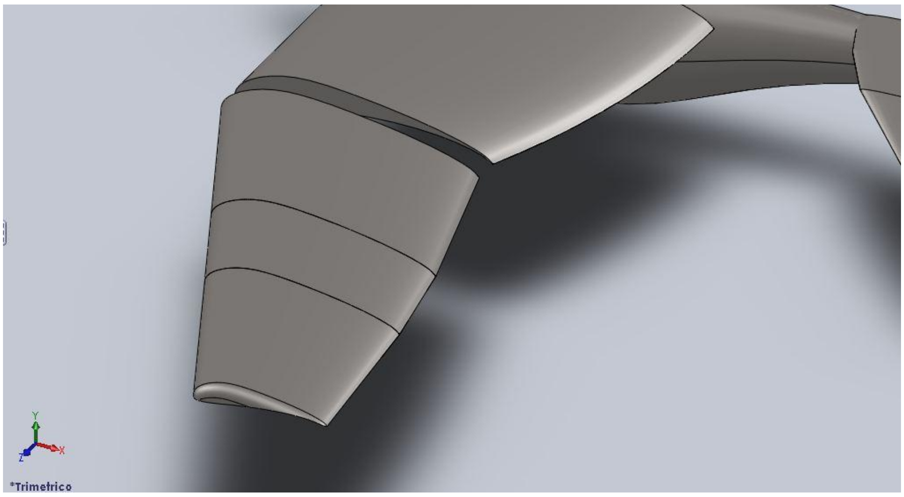

Figure 3.17: Trimetric view of the wing tip #1.

3.3.3.2 Tip #2

Theory beneath the elliptic wingtips inspired the creation of the second geometry. As can be noticed from Figure 3.18, tip is delimited by a curve, which is tangent to the *leading* and *trailing* edges. The base profile is still the Selig airfoil. However, the *loft* function which has been used extrudes the profile until the junction with a line. This creates three-dimensional body with a reverse cup shape. Then the whole wing has been scaled to have the total *span* equal to *1 m.* This geometry should reduce induced drag because of the planform shape of the tip. It is also likely to raise a bit the average value of the lift. During the *upstroke,* the convex side of the tip is leading the motion, thus *down force* should be slightly lower. Similarly, the concave side is pushing air down during *downstroke* and this could raise the lift value.

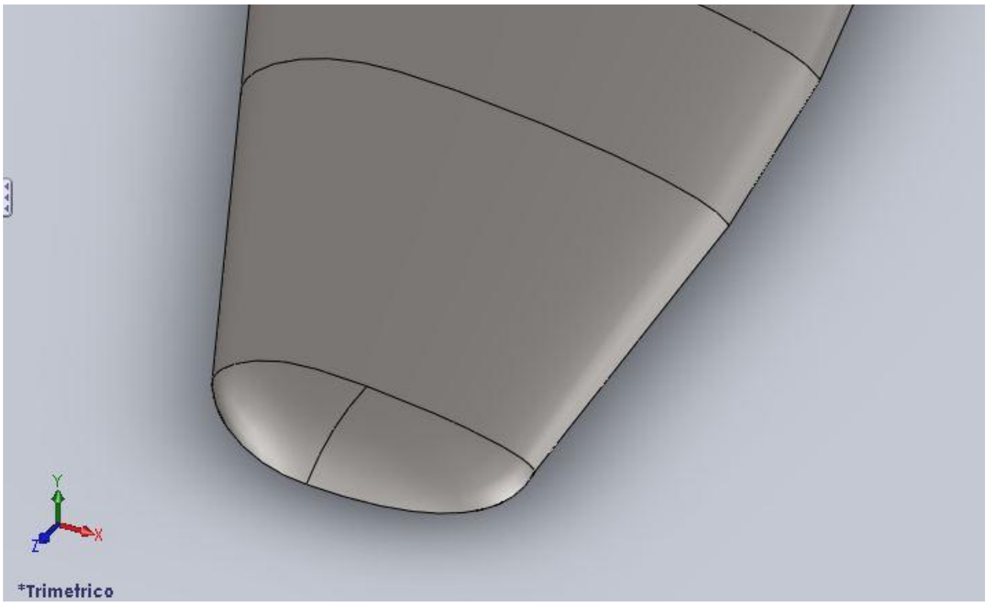

Figure 3.18: Trimetric view of the tip #2.

3.3.3.3 Tip #3

Geometry of the tip *#3* has a different genesis from the other tips; in fact, looking for a particular aerodynamic effect was not the reason which led to this configuration. Nature can give wonderful examples though. Birds are definitely the human-known objects which have the best performances in flapping wing flight. Then, it has been decided to design tip #3 with the shape of an actual wing (Figure 3.19). *Remiges*[4] are necessary in flight manoeuver control, but they are also

[4] The so-called *flight feathers* are divided into *Rectrices* and *Remiges.* First ones are located on the tail; *Remiges* are on the wings. They are divided into *Primaries, Secondaries, Tertials and Emarginations,* respectively going from the outer to the inner.

very useful in cruise flight to reduce drag. However, it is not clear if they have a direct role in flapping flight. Thus we have decided to test a wingtip resembling the actual tip of a bird with prominent *remiges* (Figure 3.19).

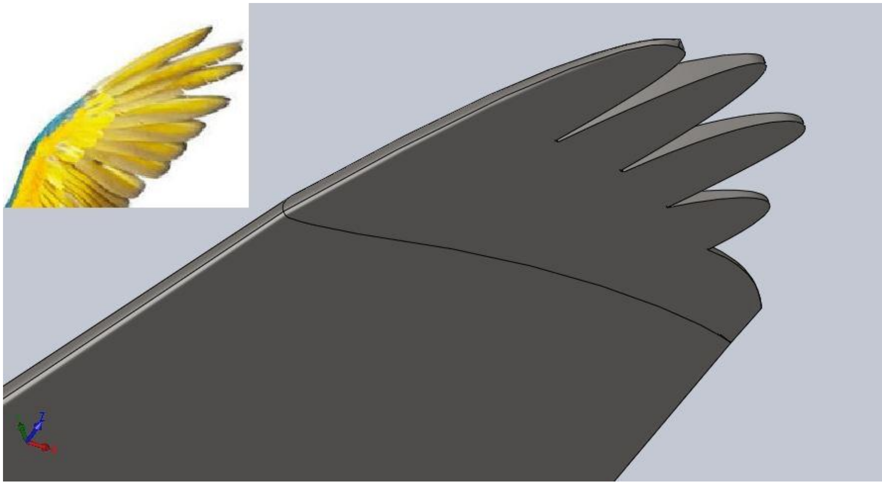

Figure 3.19: Comparison between tip #3 and *Remiges* of a Blue-and-yellow macaw.

The *CAD* process for the creation of this tip has been trickier than the others. In Figure 3.20, two intersecting bodies are shown; one of the two is the base extrusion, the second one is the body to be subtracted from the first one. Base solid has been created with a *loft* function (directed mainly to *y-axis)*, to preserve the curvature of the leading edge of the airfoil also on the tip; the other one is just an *extrusion* on the *z-axis* of a two-dimensional *Sketch*.

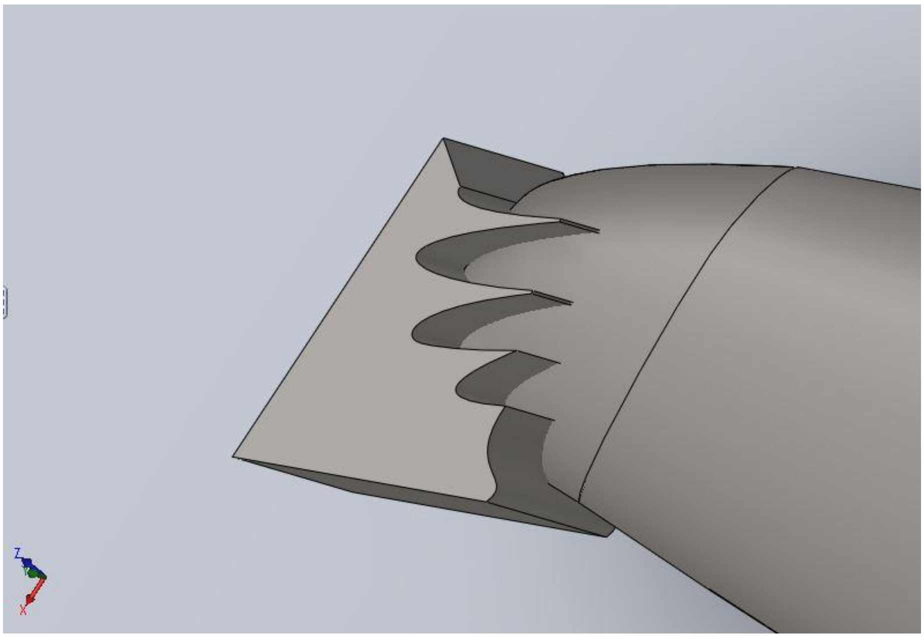

Figure 3.20: Intersecting bodies during tip #3 creation.

A *Boolean operation* of subtraction is applied and, after a scaling to *1 m* total length[5], the final result is shown below in Figure 3.21.

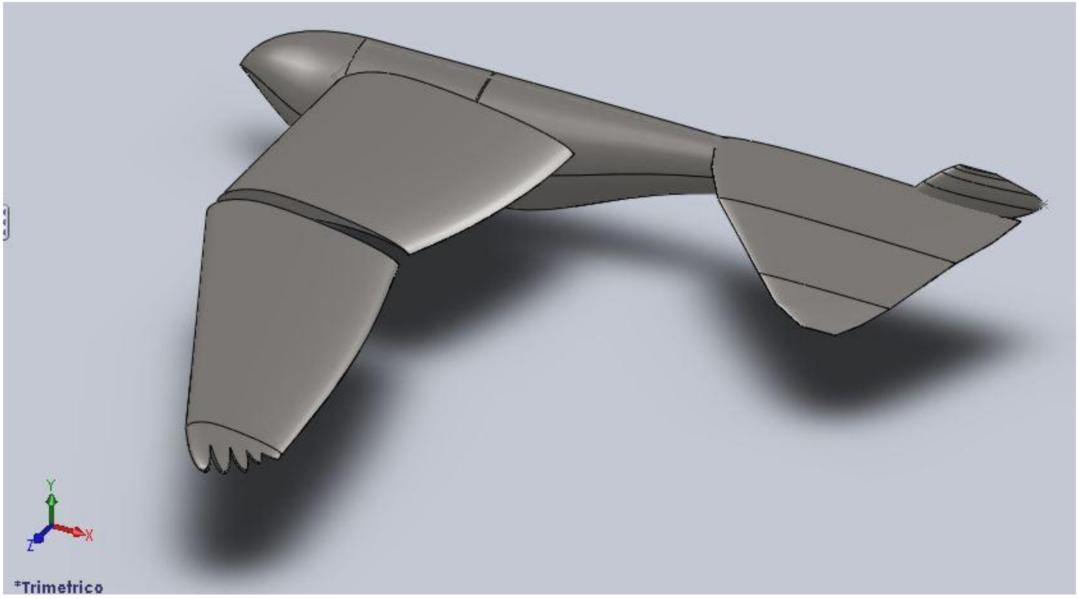

Figure 3.21: Final layout of tip#3.

Regardless performances, this tip is also interesting from the biomimetic point of view. It must be remembered that the aim of this project is the design of a surveillance *UAV*; and of course a reconnaissance vehicle should be disguised as best as possible. Section 3.4 will particularly cover this aspect of the advanced study of the wing geometry.

3.4 Biomimetic shape

3.4.1 Mimetic issue

As said before, *Skybird* is supposed to be equipped with recognition devices. If military context was ever concerned, definitely a biomimetic appearance would be necessary. This concept had been the starting point of the development of this system, since a propelled *UAV* with fixed wings can be spotted very easily, even from an inexperienced sight. Thus, the choice fell on a flapping wing system, to be as close as possible to a real flying bird. However, also particulars are involved; section 3.3.3.3 went through the creation of a biomimetic wingtip inspired by *Primaries*, whereas next paragraph will take an overview on the creation of biomimetic wing edges.

[5] Total length is considered the half-span one, i.e. the length of a single wing.

3.4.2 Geometry creation

This time the use of *Solidworks* has been quite limited. This wing conserves most part of the original wing geometry. *Guidelines* (cf. section 2.2.1) of the *loft* functions are the only difference between the two wings. *Half-span* has not changed, as well as wing cross sections at the root and tip of the wing. As far as performances are concerned, they are expected to be a little enhanced with respect to the *"0.0"* case. Curved profiles should be more aerodynamic than straight leading and trailing edges. Thus, drag coefficient is likely to be a little lower and also side coefficient could be reduced because of the *tapering* of the wing.

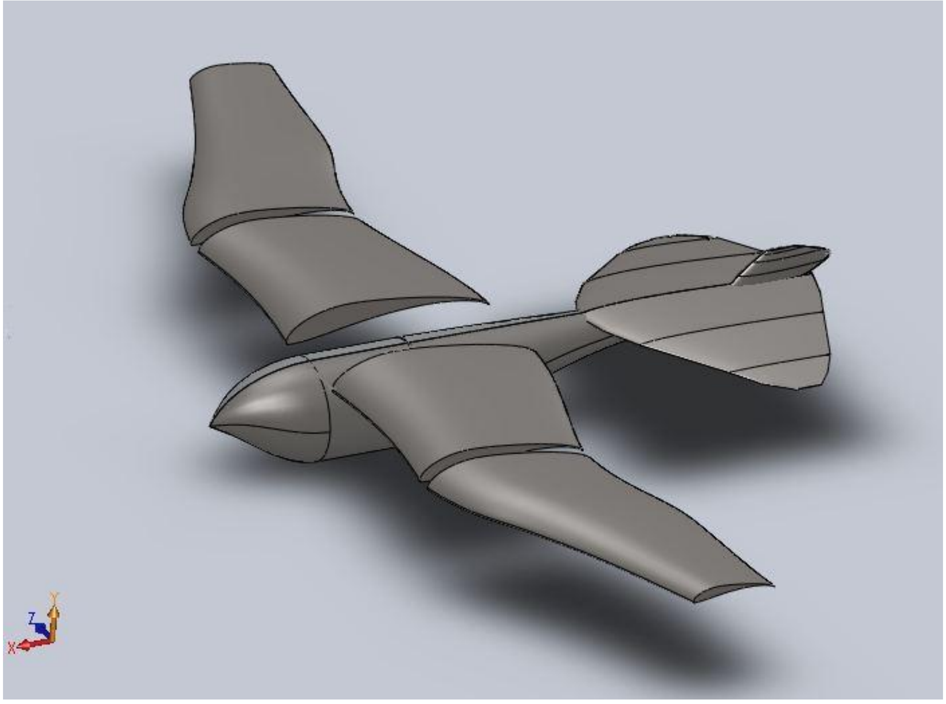

Figure 3.22: Trimetric view of the wing biomimetic edges.

Once the geometries have been obtained, "*Ansys R14"* has been used to perform *CFD* simulations. This software is based on the Finite Volume Method (*FVM*) to solve Navier-Stokes partial differential equations. *PDE*s, usually, are numerically solved because of their non-linear nature, which makes the analytic solution impossible. *FVM* discretization verifies automatically conservation laws (mass and momentum), since it deals with integrated form of *PDE*s. According to this method, inner part of the domain is divided into elementary and neighboring volumes. It is crucially important that the domain is discretized by using a grid, the so-called *mesh*. Volumes are entities very small and finite, but not infinitesimal. Thus, a good quality *mesh* keeps the accuracy of the approximated solution high. Finite Volume Theory is exposed in more details in the next chapter.

4. Computational fluid dynamics theory

All simulations have been run on *ANSYS Fluent*® [13]. In case of solvable systems, the equation solver leads to converging results throughout a numerical iterative method. All governing equations are verified within a range of tolerance on finite volumes of the fluid domain. Hereafter, the theory of the Finite Volume Method is presented.

4.1 Governing equations of fluid dynamics

The governing equations of the physics of the problem to be solved are starting point of any numerical simulation. The equation governing the motion of a fluid can be derived from the statements of the conservation of mass, momentum, and energy [22], [23], and [24]. In the most general form, the fluid motion is governed by the time-dependent three-dimensional compressible Navier-Stokes system of equations. For a viscous Newtonian fluid in the absence of external forces, mass diffusion, finite-rate chemical reaction and external heat addition, the conservation form of the Navier-Stokes system of equations can be written as

$$\frac{\partial \rho}{\partial t} + \nabla \cdot (\rho \boldsymbol{u}) = 0 \tag{4.1}$$

$$\frac{\partial (\rho \boldsymbol{u})}{\partial t} + \nabla \cdot (\rho \boldsymbol{u}\boldsymbol{u}) = -\nabla p + \nabla \cdot \tau$$

$$\frac{\partial (\rho e_t)}{\partial t} + \nabla \cdot (\rho e_t \boldsymbol{u}) = k \nabla \cdot \nabla \mathrm{T} - \nabla p \cdot \boldsymbol{u} + (\nabla \cdot \tau) \cdot \boldsymbol{u}$$

Where flow variables are defined as **u** the velocity vector, containing *u*, *v* and *w* velocity components in the *x, y* and *w* directions and *p, ρ* and e_t the pressure, density and total energy per unit mass respectively. Heat transfer variables are used as *k* thermal conductivity and T temperature. Whereas τ expresses the viscous stresses τ_{xx} , τ_{yy} , τ_{zz} , τ_{xy} , τ_{yx} , τ_{xz} , τ_{zx} , τ_{yz} and τ_{zy} given by the following relationships for the case of a Cartesian coordinate system:

$$\tau_{xx} = \frac{2}{3}\mu\left(2\frac{\partial u}{\partial x} - \frac{\partial v}{\partial y} - \frac{\partial w}{\partial z}\right), \tag{4.2}$$

$$\tau_{yy} = \frac{2}{3}\mu\left(2\frac{\partial v}{\partial y} - \frac{\partial u}{\partial x} - \frac{\partial w}{\partial z}\right),$$

$$\tau_{zz} = \frac{2}{3}\mu\left(2\frac{\partial w}{\partial z} - \frac{\partial u}{\partial x} - \frac{\partial v}{\partial y}\right),$$

$$\tau_{xy} = \tau_{xy} = \mu\left(\frac{\partial u}{\partial y} + \frac{\partial v}{\partial x}\right),$$

$$\tau_{xz} = \tau_{zx} = \mu\left(\frac{\partial u}{\partial z} + \frac{\partial w}{\partial x}\right),$$

$$\tau_{yz} = \tau_{zy} = \mu\left(\frac{\partial v}{\partial z} + \frac{\partial w}{\partial y}\right),$$

Where μ is the dynamic viscosity.

Examining closely the previous sets of equations, we clearly see that they are function of seven unknown flow field variables *u, v, z, ρ, p, T* and e_t. It is obvious that two additional equations are required to close the system. These two additional equations can be obtained by determining relationships that exist between the thermodynamic variables (*p, ρ, T,* e_t) through the assumption of thermodynamic equilibrium. For most problems in aerodynamics and gasdynamics, it is generally reasonable to assume that the gas behaves as a perfect gas, so the first additional equation can be the *perfect gas state equation*

$$p = \rho R_g T \tag{4.3}$$

where R_g is the specific gas constant and it is equal to 287 $\frac{m^2}{s^2 K}$ for air. Assuming also that the working gas behaves as a calorically perfect gas, then the following relations hold

$$e_i = c_v T, \qquad h = c_p T, \qquad \gamma = \frac{c_p}{c_v}, \qquad c_v = \frac{R_g}{\gamma - 1}, \qquad c_p = \frac{\gamma R_g}{\gamma - 1}, \tag{4.4}$$

where γ is the ratio of specific heats and it is equal to 1.4 for air, with c_v the specific heat at constant volume, c_p the specific heat at constant pressure, and *h* the enthalpy. By using eq. 4.3 and eq. 4.4, we obtain the following relations for pressure *p* and temperature *T*

$$p = (\gamma - 1)\rho e_i \tag{4.5}$$

$$T = \frac{p}{\rho R_g} = \frac{(\gamma - 1)e_i}{R_g} \tag{4.6}$$

where the specific internal energy per unit mass $e_i = p/(\gamma-1)\rho$ is related to the total energy per unit mass e_t by the following relationship,

$$e_t = e_i + \frac{1}{2}(u^2 + v^2 + w^2) \tag{4.7}$$

In this discussion it is necessary to relate the transport properties (μ, k) to the thermodynamic variables. Then the dynamic viscosity is computed by Sutherland's formula

$$\mu = \frac{C_1 T^{\frac{3}{2}}}{(T + C_2)} \tag{4.8}$$

where, for the case of air, the constant are $C_1 = 1.458 \cdot 10^{-6} \frac{kg}{ms\sqrt{K}}$ and $C_2 = 110.4\ K$, k is the thermal conductivity.

The Navier-Stokes system of equations (4.1) is a coupled system of nonlinear partial differential equations (*PDE*), and hence very difficult to solve. Since nowadays a closed form general solution of the equations has not yet been found, approximations are applied to find a solution, evaluated on a given domain D with prescribed boundary conditions ∂D and given initial conditions $D\dot{\boldsymbol{Q}}$.

4.1.1 Simplification of the *NSE*: Incompressible Viscous Flow case

The equations previously analyzed are the most general form of the Navier-Stokes system of equations, describing the behavior of a Newtonian, compressible fluid. However, for most cases of aerodynamic flow characterized by a low Reynolds number, compressibility of the air is negligible; in other words standard air is considered as an incompressible fluid [25]. If the flow is also isothermal, the viscosity is constant as well. With the hypothesis assumed earlier, the governing equations written in compact form reduce to the following set

$$\begin{gathered} \nabla \cdot (\boldsymbol{u}) = 0 \\ \frac{\partial \boldsymbol{u}}{\partial t} + \nabla \cdot (\boldsymbol{u}\boldsymbol{u}) = \frac{-\nabla p}{\rho} + \nu \nabla^2 \boldsymbol{u} \end{gathered} \tag{4.9}$$

where ν is the kinematic viscosity defined as $\nu = \mu/\rho$.

The viscous stresses in Cartesian coordinates are:

$$\begin{aligned} \tau_{xx} &= 2\,\mu \frac{\partial u}{\partial x}, \\ \tau_{yy} &= 2\,\mu \frac{\partial v}{\partial y}, \\ \tau_{zz} &= 2\,\mu \frac{\partial w}{\partial z}, \end{aligned} \tag{4.10}$$

$$\tau_{xy} = \tau_{xy} = \mu \left(\frac{\partial u}{\partial y} + \frac{\partial v}{\partial x}\right),$$

$$\tau_{xz} = \tau_{zx} = \mu \left(\frac{\partial u}{\partial z} + \frac{\partial w}{\partial x}\right),$$

$$\tau_{yz} = \tau_{zy} = \mu \left(\frac{\partial v}{\partial z} + \frac{\partial w}{\partial y}\right),$$

The set of equations (4.9) is still a *PDE* system; however, a lower number of variables is involved compared to system (4.1). In theory this should mean that the numerical results are achieved faster.

4.2 Turbulence modeling

All flows encountered in engineering applications, from simple ones to complex three-dimensional ones, become unstable above a certain Reynolds number. At low Reynolds number flows are laminar, but as we increase it, flows tend to become turbulent. Turbulent flows are characterized by a chaotic and random state of motion in which velocity and pressure change continuously on a broad range of time and length scales.

There are several possible approaches to the simulation of turbulent flows. The first and most intuitive one is to directly solve the set of governing equations. However, extremely fine mesh elements are required in order to have a precise modeling of the problem. This approach is called *DNS* (Direct Numerical Simulation) and it is mainly used for academic purposes. It is not possible to tackle industrial problems by *DNS* because of the prohibitive computer costs imposed by the mesh requirements.

A different methodology to model turbulent flows is Large Eddy Simulations (*LES*). This method consists of the direct simulation of the large scale turbulences, whereas the small scales are filtered by a functional model. This allows to reduce storage and computational requirements compared to DNS. *LES* approximations is still quite conservative since small scale eddies have usually common characteristics and it is reasonable to consider them with a model. Thanks to advances in computer hardware and parallel, the use of *LES* for industrial problems is becoming practical.

The most widely diffused modeling application for industrial problems is the Reynolds Averaged Navier-Stokes (RANS) system. In this approach, the RANS equations are derived by decomposing the flow variables into (generally) a time-mean part (obtained over a proper time interval) and a fluctuating part, and then time averaging the entire equations. This process gives rise to new terms which have to be related to the mean flow variables through turbulence models. This statistical approach has been originally developed based on experimental data for relatively simple controlled system. This limits the range of applicability of the turbulence models within a spectrum of condition and geometries.

4.2.1 Reynolds Averaging

The starting point for deriving the RANS equations is the Reynolds decomposition of the general flow variable φ by the sum of a mean value (denoted by a bar over the variable, $\bar{\phi}$) and a time-dependent fluctuating part (denoted by a prime, ϕ').

$$\phi(\boldsymbol{x},t) = \bar{\phi}(\boldsymbol{x},t) + \phi'(\boldsymbol{x},t) \tag{4.11}$$

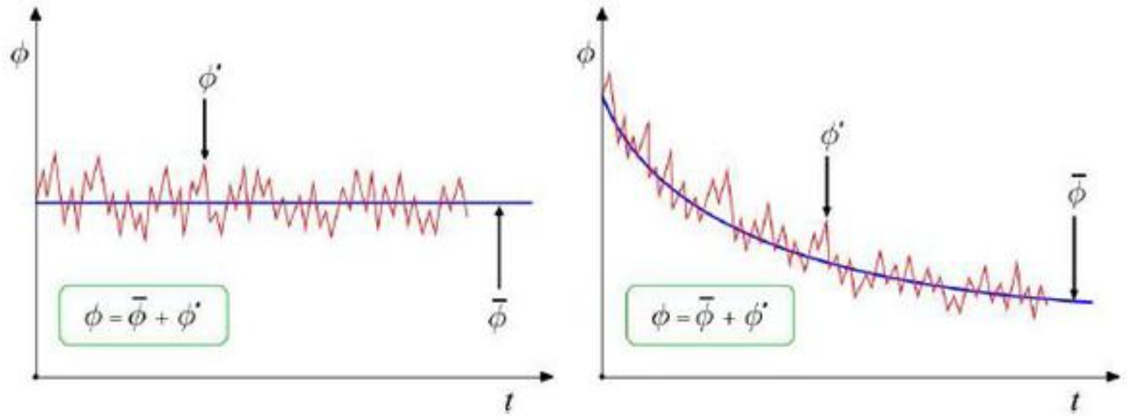

Figure 4.1: *Time averaging for a statistically steady flow (left) and ensemble averaging for an unsteady flow (right)*

The mean value $\bar{\phi}$ is obtained by an averaging procedure. There are three different forms of the Reynolds averaging:

1. Time averaging: appropriate for stationary turbulence (statistically steady)

$$\bar{\phi}(\boldsymbol{x}) = \lim_{T\to+\infty} \frac{1}{T} \int_t^{t+T} \phi(\boldsymbol{x},t)\, dt \tag{4.12}$$

where t is the time and T is the averaging interval. T must be large compared to the typical time scale of the fluctuations. This is the case appropriate for $\bar{\phi}$ not varying in time, but only in space.

2. Spatial averaging: appropriate for homogenous turbulence

$$\bar{\phi}(t) = \lim_{CV\to\infty} \frac{1}{CV} \int_{CV} \phi(\boldsymbol{x},t)\, dCV \tag{4.13}$$

With $\mathcal{CV}$ being a control volume. In this case $\bar{\phi}$ is uniform in space, but is allowed to vary in time.

3. Ensemble averaging: appropriate for statistically unsteady turbulence

$$\bar{\phi}(\boldsymbol{x},t) = \lim_{N\to\infty} \frac{1}{N} \sum_{i=1}^{N} \phi(\boldsymbol{x},t) \tag{4.14}$$

Where N is the number of experiments of the ensemble and it must be large enough to prevent variation due to stochastic phenomena. Here $\bar{\phi}$ is function of both time and space (as illustrated in Figure 4.1).

In case of stationary on homogeneous flow, all three averaging methods are equivalent.

4.2.2 Incompressible Reynolds Averaged Navier-Stokes Equations

Let us recall the Reynolds decomposition for the flow variables of the incompressible *NSE* (4.9)

$$\begin{aligned} \boldsymbol{u}(\boldsymbol{x},t) &= \overline{\boldsymbol{u}}(\boldsymbol{x}) + \boldsymbol{u}'(\boldsymbol{x},t), \\ p(\boldsymbol{x},t) &= \bar{p}(\boldsymbol{x}) + p'(\boldsymbol{x},t), \end{aligned} \tag{4.15}$$

now substituting eqs. (4.15) into the incompressible Navier-Stokes equations (4.9) we obtain for the continuity equation

$$\nabla \cdot (\boldsymbol{u}) = \nabla \cdot (\overline{\boldsymbol{u}} + \boldsymbol{u}') = \nabla \cdot (\overline{\boldsymbol{u}}) + \nabla \cdot (\boldsymbol{u}') = 0 \tag{4.16}$$

Then, time averaging, eq (4.16) results in

$$\nabla \cdot \left(\overline{\overline{\boldsymbol{u}}}\right) + \nabla \cdot \left(\overline{\boldsymbol{u}'}\right) = 0 \tag{4.17}$$

and using averaging properties, it follows that

$$\nabla \cdot (\overline{\boldsymbol{u}}) = 0. \tag{4.18}$$

Same steps applied to momentum equation lead to

$$\frac{\partial \overline{\boldsymbol{u}}}{\partial t} + \nabla \cdot \left(\overline{\boldsymbol{u}}\,\overline{\boldsymbol{u}} + \overline{\boldsymbol{u}'\boldsymbol{u}'}\right) = \frac{-\nabla \bar{p}}{\rho} + \nu \nabla^2 \overline{\boldsymbol{u}}. \tag{4.19}$$

Grouping equations (4.18) and (4.19), we obtain the following set of equations,

$$\nabla \cdot (\overline{\boldsymbol{u}}) = 0.$$
$$\frac{\partial \overline{\boldsymbol{u}}}{\partial t} + \nabla \cdot (\overline{\boldsymbol{u}}\,\overline{\boldsymbol{u}}) = \frac{-\nabla \bar{p}}{\rho} + \nu \nabla^2 \overline{\boldsymbol{u}} + \frac{1}{\rho} \nabla \cdot \tau^R. \tag{4.20}$$

The set of equations (4.20) are the incompressible Reynolds-Averaged Navier-Stokes (RANS) equations. They are identical to the incompressible *NSE* (9) with the exception of the additional term $\tau^R = -\rho(\overline{\boldsymbol{u}}\,\overline{\boldsymbol{u}})$, where τ^R is the so-called Reynolds-stress tensor. It represents the amount of momentum transferred by fluctuating motion and it is defined in Cartesian coordinates as

$$\tau^R = -\rho(\overline{\boldsymbol{u}}\,\overline{\boldsymbol{u}}) = -\begin{pmatrix} \rho(\overline{u'}\overline{u'}) & \rho(\overline{u'}\overline{v'}) & \rho(\overline{u'}\overline{w'}) \\ \rho(\overline{v'}\overline{u'}) & \rho(\overline{v'}\overline{v'}) & \rho(\overline{v'}\overline{w'}) \\ \rho(\overline{w'}\overline{u'}) & \rho(\overline{w'}\overline{v'}) & \rho(\overline{w'}\,\overline{w'}) \end{pmatrix} \tag{4.21}$$

τ^R consists of nine components, but they can be reduced to six, since *u, v* and *w* can be interchanged.

A problem remains on the number of unknowns in system (4.20) (namely pressure (*p*), three components of velocity (*u, v, w*) and the six components of τ^R). They are 10 and there are four equations; hence the system is not closed. The objective is thus to find the six remaining auxiliary equations.

4.2.3 Boussinesq Approximation

The Reynolds averaged approach to turbulence modeling requires that the Reynolds stresses to be derived semi-analytically and several strategies are available to end up with a form of τ^R. The Boussinesq approximation is one of them; it is based on the hypothesis to relate the Reynolds stress to the mean velocity gradients, i.e.

$$\tau^R = -\rho(\overline{\boldsymbol{u}'\boldsymbol{u}'}) = \mu_T[\nabla \overline{\boldsymbol{u}} + (\nabla \overline{\boldsymbol{u}})^T] - \frac{2}{3}\rho\kappa \boldsymbol{I} \tag{4.22}$$

where **I** is the identity matrix, ^{T} is the transpose, μ_T is called the turbulent eddy viscosity, and

$$\kappa = \frac{1}{2}(\overline{\boldsymbol{u}'} \cdot \overline{\boldsymbol{u}'}) \tag{4.23}$$

is the turbulent kinetic energy. Essentially this theory is based on the assumption that the fluctuating stress is proportional to the gradient of average quantities, as Newtonian flows are. In order to evaluate κ usually a governing equation is derived and solved; typically two-equation models include this option.

The turbulent eddy viscosity μ_T is a property of the flow field and not a physical property of the fluid. However, the eddy viscosity concept has been developed assuming a relationship or even an analogy with the molecular viscosity. In spite of theoretical weakness of the eddy viscosity concept, it does reproduce reasonable results for a large number of flows.

The Boussinesq approximation reduces the turbulence modeling process from finding the six turbulent stress components τ^R to determining an appropriate value for the turbulent eddy viscosity μ_T, since an analytical function between them is provided.

4.2.4 Two-equations Models: the κ-ω Model

In this section the widely used κ-ω model is presented. This model is the approach taken in all *Skybird* simulations. It is based on two equations in which the turbulent kinetic energy κ and the turbulent specific dissipation rate ω are involved. Throughout auxiliary relations, they lead to the derivation of the turbulent eddy viscosity μ_T.

Eddy Viscosity

$$\mu_T = \frac{\rho\kappa}{\omega} \tag{4.24}$$

Turbulent Kinetic Energy

$$\rho\frac{\partial\kappa}{\partial t} + \rho\nabla\cdot(\boldsymbol{u}\kappa) = \tau^R\nabla\boldsymbol{u} - \beta^*\rho\kappa\omega + \nabla\cdot[(\mu+\sigma^*\mu_T)\nabla\kappa] \tag{4.25}$$

Specific Dissipation Rate

$$\rho\frac{\partial\omega}{\partial t} + \rho\nabla\cdot(\boldsymbol{u}\omega) = \alpha\frac{\omega}{\kappa}\tau^R\nabla\boldsymbol{u} - \beta\rho\omega^2 + \nabla\cdot[(\mu+\sigma\mu_T)\nabla\omega] \tag{4.26}$$

Closure Coefficients

$$\alpha = \frac{5}{9}, \quad \beta = \frac{3}{40}, \quad \beta^* = \frac{9}{100}, \quad \sigma = \frac{1}{2}, \quad \sigma^* = \frac{1}{2} \tag{4.27}$$

Auxiliary Relations

$$\epsilon = \beta^*\omega\kappa \qquad and \qquad l = \frac{\sqrt{\kappa}}{\omega} \tag{4.28}$$

4.3 Finite Volume Method Discretization

The purpose of every discretization is to transform a partial differential equation (*PDEs*) into a corresponding algebraic one. The solution of the discretized system produces a set of value which has to be the same as the local quantities derived by the original system. The discretization process can be described as a two-steps process, namely; the subdivision of the solution domain into many smaller portions and the discretization of the equations.

The discretization of the solution domain produces a numerical description of the geometrical domain, divided into a finite number of geometrical regions, called control volumes or, generally, cell elements. For transient simulations also the time-domain is divided into a certain number of time steps. Spatial and time discretization has to be fine enough to let the algorithms calculate a precise local solution according to the requirements of the simulation. The equation discretization step altogether with the domain discretization, produces an appropriate transform of the terms of the governing equations into a system of discrete algebraic equations that can be solved using a direct or an iterative method.

4.3.1 Discretization of the solution domain

Discretization of the solution domain proceeds by two steps: creating a computational mesh for the geometry over which the equations are solved and discretization of the time scale. As far as the second one is concerned, it is enough to proceed in time by a single time step, updating the variables from the previous solution. Discretization of space for the Finite Volume Method (*FVM*, [24], [26], [27], [28], [29], [30], and [31]) requires a subdivision into discrete arbitrary control volumes ($\mathcal{CV}$s). They cannot intersect each other and they completely fill the domain.

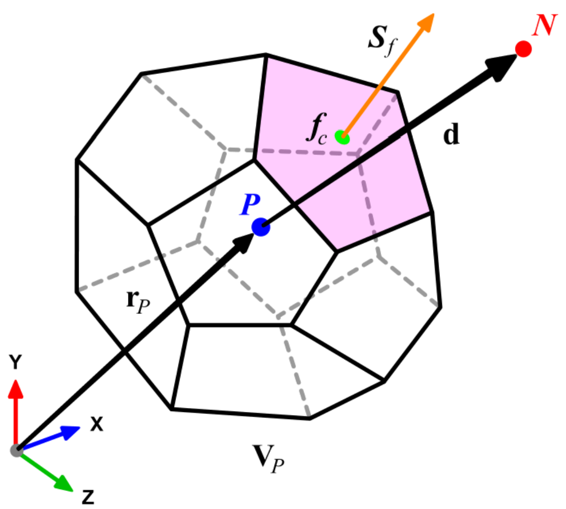

Figure 4.2: Arbitrary polyhedral control volume CV_P. CV is constructed around a point P (CV centroid), hence the notation CV_P and its volume is V_P. The vector from the cell center point P to the neighboring cell point N is d, which represents the distance between them. The faces area vector S_f points outwards from CV_P. The CV faces are labeled as f_c, which also denotes the face center.

The control volume is bounded by a set of flat faces corresponding to cell bounds. There are two different types of faces. Internal faces which separates neighboring control volumes, and boundary faces, laying on the bounds of the domain.

4.3.2 Discretization of the Transport Equation

All equations previously seen can be written in the form of the general transport equation over a given control volume enclosing a point *P* as follows

$$\underbrace{\int_{V_P} \frac{\partial \rho\phi}{\partial t}\, dV}_{temporal\ derivative} + \underbrace{\int_{V_P} \nabla\cdot(\rho\boldsymbol{u}\phi)\, dV}_{convective\ term} - \underbrace{\int_{V_P} \nabla\cdot\left(\rho\Gamma_\phi\nabla_\phi\right) dV}_{diffusion\ term} = \underbrace{\int_{V_P} S_\phi(\phi)\, dV}_{source\ term} \tag{4.29}$$

Here ϕ is the transport quantity, *i.e.*, velocity, mass or turbulent energy and Γ_ϕ is the diffusion coefficient of the transported quantity.

Since the diffusion term includes a second order derivative of ϕ in space, to represent the whole equation with the same accuracy, temporal discretization has to be of second order as well. As a consequence, all variables are assumed to vary linearly around the point *P* and the time *t*

$$\phi(\boldsymbol{x}) = \phi_P + (\boldsymbol{x} - \boldsymbol{x}_P)\cdot(\nabla\phi)_P \tag{4.30}$$

$$\phi(t+\delta t) = \phi^t + \delta t\left(\frac{\partial\phi}{\partial t}\right)^t$$

Finally, it should be mentioned that Gauss theorem will be widely used in the following discussion to substitute volume integrals into surface ones on the boundaries of the $\mathcal{CV}$.

Convection Term

The discretization of the convection term is obtained from the application of Green-Gauss' theorem on the relative term in equation (4.29)

$$\int_{V_P} \nabla\cdot(\rho\boldsymbol{u}\phi)\, dV = \sum_f \boldsymbol{S}\cdot(\rho\boldsymbol{u}\phi)_f = \sum_f \boldsymbol{S}\cdot(\rho\boldsymbol{u})_f\phi_f = \sum_f F\,\phi_f \tag{4.31}$$

where F in equation (4.31) represents the mass flux through the face and defined as

$$F = \boldsymbol{S} \cdot (\rho \boldsymbol{u})_f \tag{4.32}$$

Obviously the flux F depends on the face value ρ and the velocity vector **u** (calculated as explained in the next section). Lastly, we have to keep in mind that the summation of this entity over the whole control volume surface must be equal to zero, according to the hypothesis of the conservation of mass:

$$\int_{V_P} \nabla \cdot \boldsymbol{u}\, dV = \oint_{\partial V_P} d\boldsymbol{S} \cdot \boldsymbol{u} = \sum_f \left(\int_f d\boldsymbol{S} \cdot \boldsymbol{u} \right) = \sum_f F = 0 \tag{4.33}$$

Convection Differencing Scheme

The role of the convection differencing is to evaluate the value of a certain variable ϕ_f on the control volume surface using the values in the centers of the neighboring $\mathcal{CV}$s. Since linearity is assumed, a simple interpolation on the spatial scale is introduced between centers *P* and *N.*

$$\phi_f = f_x \phi_P + (1 - f_x)\phi_N \tag{4.34}$$

where f_x is the ratio of the distances *fN* and *PN*.

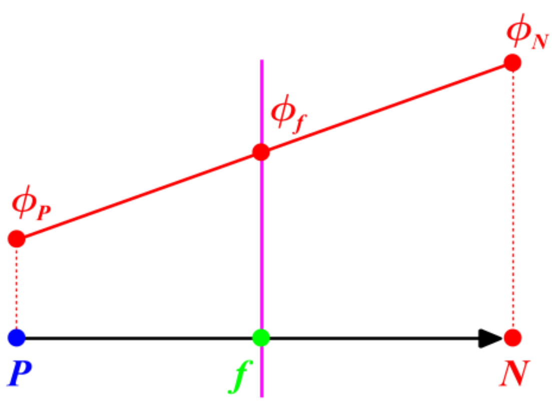

Figure 4.3: Face interpolation.

This method is commonly called Central Differencing (*CD*) and it is characterized by the important feature to be second order accurate for the case of uniform grid distribution ([24], [26], [27], [28], [29], [31], and [32]). This is consistent with the overall accuracy of the discretization. However, *CD* practice has an intrinsic issue. In problems dominated by convection phenomena, this method tends to create unphysical oscillations in the solution which might grow without bound preventing convergence of the procedure.

Diffusion term

Using a similar approach as before, the diffusion term in equation (4.29) can be discretized as follows

$$\int_{V_P} \nabla \cdot (\rho\Gamma_\phi \nabla_\phi)\, dV = \sum_f \boldsymbol{S} \cdot (\rho\Gamma_\phi \nabla_\phi)_f = \sum_f (\rho\Gamma_\phi)_f \boldsymbol{S} \cdot (\nabla\phi)_f \tag{4.35}$$

where $(\Gamma_\phi)_f$ can be found from equation (4.34). If the mesh is orthogonal, in other words the vectors **d** and **S** in figure 4 are parallel, it is possible to use the following expression

$$\boldsymbol{S} \cdot (\nabla\phi)_f = |\boldsymbol{S}| \frac{\phi_N - \phi_P}{|\boldsymbol{d}|} \tag{4.36}$$

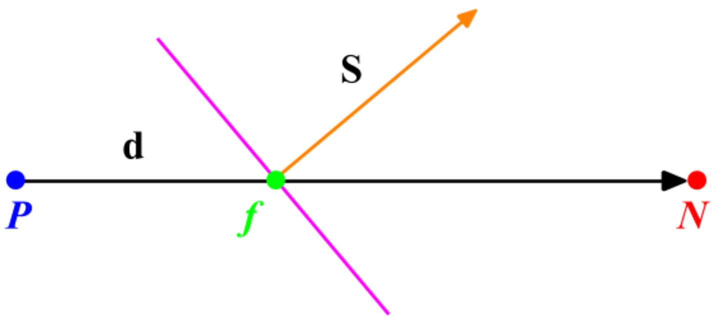

Figure 4.4: Vector d and S on a non-orthogonal mesh.

With equation (4.36) the gradient of the face variable is reduced to a function of the values of the closest centers.

Unfortunately, mesh orthogonality is more an exception than a rule. It is thus preferred to model the vector **S** as a two-component vector and to apply only on the appropriate component the expression (4.35). Vector **S** is split as follows

$$\boldsymbol{S}\cdot(\nabla\phi)_f = \underbrace{\Delta\cdot(\nabla\phi)_f}_{orthogonal\ contribution} + \underbrace{\boldsymbol{k}\cdot(\nabla\phi)_f}_{non-orthogonal\ contribution} . \tag{4.37}$$

The two vectors **Δ** and ***k*** introduced in equation (4.37) need to satisfy the condition

$$\boldsymbol{S} = \Delta + \boldsymbol{k}. \tag{4.38}$$

Since vector Δ is parallel to vector ***d*** by definition, it can be derived from equation (4.36); whereas the non-orthogonal part has to be treated in another way. To handle mesh decomposition there are several approaches ([28], [32], [33]), however the so-called over-relaxed approach seems to be the most robust and efficient. The relative model of vector Δ is defined as follows

$$\Delta = \frac{\boldsymbol{d}}{\boldsymbol{d}\cdot\boldsymbol{S}}|\boldsymbol{S}|^2. \tag{4.39}$$

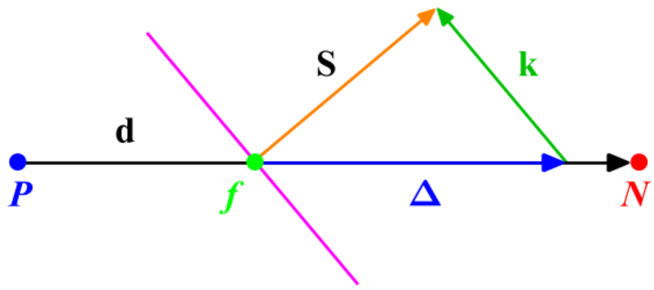

Figure 4.5: Vectorial decomposition of face area vector

The diffusion term equation in its differential form exhibits a bounded behavior. Thus care must be taken to keep the mesh quality high. If this happens, the boundedness of the solution is not affected by the correction due to non-orthogonal meshes.

Source terms

All terms of the transport equation that cannot be written as convection, diffusion or temporal contributions are here included in the source term. The source term $S_\phi(\phi)$ is a general function of a face variable ϕ.

Specific theories are not discussed here, we limit ourselves to a description of the source term as a linear function of ϕ, such that

$$S_\phi = S_u + S_p\phi\,, \tag{4.40}$$

where S_u and S_p can also depend on face variables. The volume integral of the source term in equation (4.29) can be written as follows, using relation (4.40).

$$\int_{V_P} S_\phi(\phi)\, dV = S_u V_P + S_p V_P \phi_P \tag{4.41}$$

Conclusions

Reynolds transport equation can be thus written, using equations (4.31), (4.35) and (4.41), as

$$\int_{V_P} \frac{\partial \rho\phi}{\partial t} dV + \sum_f F\,\phi_f - \sum_f \left(\rho\Gamma_\phi\right)_f \boldsymbol{S}\cdot(\nabla\phi)_f = S_u V_P + S_p V_P \phi_P \tag{4.42}$$

4.3.3 Temporal Discretization

In the previous sections spatial discretization was presented. Let us now consider the derivative of the general transport equation (4.29), by integrating in time we obtain:

$$\int_t^{t+\delta t} \left[\frac{\partial}{\partial t}\int_{V_P} \rho\phi\, dV + \int_{V_P} \nabla\cdot(\rho\boldsymbol{u}\phi)\, dV - \int_{V_P} \nabla\cdot\left(\rho\Gamma_\phi \nabla_\phi\right) dV\right] dt = \int_t^{t+\delta t}\left(\int_{V_P} S_\phi(\phi)\, dV\right) dt \tag{4.43}$$

or, deriving from equation (4.43), the so-called *semi-discretized* form of the transport equation

$$\int_t^{t+\delta t} \left[\left(\frac{\partial \rho\phi}{\partial t}\right)_P V_P + \sum_f F\,\phi_f - \sum_f \left(\rho\Gamma_\phi\right)_f \boldsymbol{S}\cdot(\nabla\phi)_f = S_u V_P + S_p V_P \phi_P\right] dt = \int_t^{t+\delta t} \left(S_u V_P + S_p V_P \phi_P\right) dt. \tag{4.44}$$

It should be noted that the order of the temporal unsteady term does not need to be necessarily the same as the spatial terms (convection, diffusion and source). Thus, each term can be treated separately, according to specific requirements. As long as the individual terms are second order accurate, the overall accuracy will also be second order.

4.3.3.1 Crank-Nicolson time centered method and backward differencing method

Keeping in mind the fact that ϕ changes in time, temporal derivative and time integral can be calculated as follows

$$\left(\frac{\partial\rho\phi}{\partial t}\right)_P = \frac{\rho_P^n\phi_P^n - \rho_P^{n-1}\phi_P^{n-1}}{\delta t} \tag{4.45}$$

$$\int_t^{t+\delta t}\phi(t)dt = \frac{1}{2}(\phi_P^{n-1} + \phi^n)\ \delta t$$

where superscripts *n* and *n-1* indicate the new and the previous time respectively at which the variables are evaluated. Combining equations (4.45) with the *semi-discretized* form of the transport equation (eq. 4.44), and assuming that density and diffusivity do not change in time we have

$$\begin{aligned}\frac{\rho_P^n\phi_P^n - \rho_P^{n-1}\phi_P^{n-1}}{\delta t}V_P &+ \frac{1}{2}\sum_f F\,\phi_f^n - \frac{1}{2}\sum_f \left(\rho\Gamma_\phi\right)_f \boldsymbol{S}\cdot(\nabla\phi)_f^n \\ &+ \frac{1}{2}\sum_f F\,\phi_f^{n-1} - \frac{1}{2}\sum_f \left(\rho\Gamma_\phi\right)_f \boldsymbol{S}\cdot(\nabla\phi)_f^{n-1} \\ &= S_uV_P + \frac{1}{2}S_pV_P\phi_P^n + \frac{1}{2}S_pV_P\phi_P^{n-1}\,.\end{aligned} \tag{4.46}$$

This is the so-called Crank-Nicolson (CN) method. It requires the values of φ for both new and old time levels. Although it is unconditionally stable, it does not guarantee the boundedness of the solution. However, the backward differencing method has better stability properties and it is second order accurate.

Since the variation of φ in time is assumed to be linear, the discretization presented by equation (4.43), is second order accurate only in a $t \pm \delta t$ time interval. Backwards Differencing (*BD*) uses three time levels to calculate temporal derivative. Expressing time levels *n-2* and *n*-1 using a Taylor expansion around time *n*, we obtain a second order approximation of the temporal derivative as follows

$$\left(\frac{\partial\phi}{\partial t}\right)^n = \frac{\frac{3}{2}\phi^n - 2\phi^{n-1} + \frac{1}{2}\phi^{n-2}}{\delta t}. \tag{4.47}$$

By neglecting the temporal variation in the faces fluxes and derivatives, equation (4.46) produces a fully implicit discretization of the transport equation:

$$\frac{\frac{3}{2}\rho_P\phi^n - 2\rho_P\phi^{n-1} + \frac{1}{2}\rho_P\phi^{n-2}}{\delta t}V_P + \sum_f F\,\phi_f^n - \sum_f \left(\rho\Gamma_\phi\right)_f \boldsymbol{S}\cdot(\nabla\phi)_f^n = S_uV_P + S_pV_P\phi_P^n \tag{4.48}$$

In *CN* method inner iterations are needed due to the evaluation at the time *n+1* which starts from the new time *n*. *BD* method results in a smaller computational effort since those additional calculations are not required. However the lack of variation leads to a wider computational error.

4.3.4 Boundary Conditions

Each control volume provides an algebraic equation. However external cells have to be considered in a special way. Since there are no nodes outside the domain, face flux values on the boundaries cannot be evaluated by averaging center values of the neighboring cells. To prevent extra unknowns from being introduced in a system of a fixed number of equations, boundary conditions have to be supplied.

Usually there are three different types of boundary conditions, which are used to close the system:

- Zero-gradient *BC*s, defining the solution gradient to be zero. It is also known as Neumann-type *BC*.
- Fixed-value *BC*s. The Dirichlet-type *BC* defines a specified value on certain points.
- Symmetry *BC*s treats the conservation of variables as if the boundary was a mirror plane. This condition specifies that the component of the solution gradient normal to this plan should be fixed to zero.

For example, for an external aerodynamics simulation, at the inflow boundary the velocity is defined as fixed-value and the pressure as zero-gradient. At the outflow bound, the pressure is defined as fixed-value and the velocity as zero-gradient. If symmetry is a concern, a symmetric *BC* is used at fixed-boundaries.

4.3.5 Flow Solver and Solution of the Navier Stokes Equation

In this study, the unsteady incompressible Reynolds-Averaged Navier-Stokes (*URANS*) equations are numerically approximated by using the commercial finite volume solver *Ansys Fluent*. The cell-centered values of the variables are interpolated at the face location using a second-order centered difference scheme for the diffusion terms. The convective terms at cell faces are discretized by means of second-order upwind scheme [39]. In order to prevent spurious oscillations a multidimensional slope limiter is used [40], which enforce the monotonicity principle by prohibiting the linearly reconstructed field variable on the cell faces to exceed the maximum or the minimum of neighboring cells. This results in a total variation diminishing (*TVD*) scheme, which guarantees the accuracy, stability and boundedness of the solution [23, 25, and 26]. For computing the gradients at cell centers, the least square cell-based reconstruction method is used. The pressure-velocity coupling is achieved by means of the *SIMPLE* algorithm [25, 27, and 28] with cell orthogonality corrections and as the solution takes place in collocated meshes, the Rhie-Chow [41] interpolation scheme is used to prevent pressure checkerboard instability. The turbulent quantities (κ and ω) are discretized using the same scheme as for the convective terms. For time discretization it used a second order backward implicit method. Hence, the whole methodology is second order accurate in space and time.

5. Simulations and results data

5.1 Simulation set up conditions

Geometries have been created by assembling single parts such as tail, rudder, fuselage and wings, separately drawn. Then, it is necessary to work on the *meshes* to discretize the fluid domain. The tools *"Ansys Design Modeler"* and *"Ansys Mesher"* have been used to import in *Ansys* the geometry previously generated in *CAD* software *Solidworks.* A parallelepiped computational domain is created around the *Skybird.* The inlet surface of the flow is far enough not to interfere with the geometry; the outlet surface is separated from the body by a sufficient distance to let wingtip vortices develop completely (Figure 5.1). Each external face of the fluid domain has been named with the function *"Named Selection"* and characterized by the relative feature. The velocity value associated with the *Inlet* face is *5 m/s*. This value is related to a Reynolds number of around *Re = 130.000* ($Re = \frac{\rho v L}{\mu}$, where *L* is the *chord length*). A "*wall with slip condition*" is assigned to four external side faces of the domain. On the *outlet* face a "*pressure outlet"* condition is used, set at the atmospheric pressure value. The symmetry plan is also featured by a *symmetry condition,* which means not only perpendicular velocity to the plane equal to zero, but also the gradients of all the variables normal to it equal to zero. Finally, a "*Boolean operation"* is applied to the parallelepiped: the solid domain delimited by the *Skybird* outline must be subtracted from the fluid domain. At this point the *.agdb* extension file is exported to "*Ansys Mesher".* It has to be noticed that, since the symmetrical conditions of the problem, *CAD* drawings and meshes deal with half of the *Skybird*, simulations are performed only on half of the domain; the other half must present the same behavior.

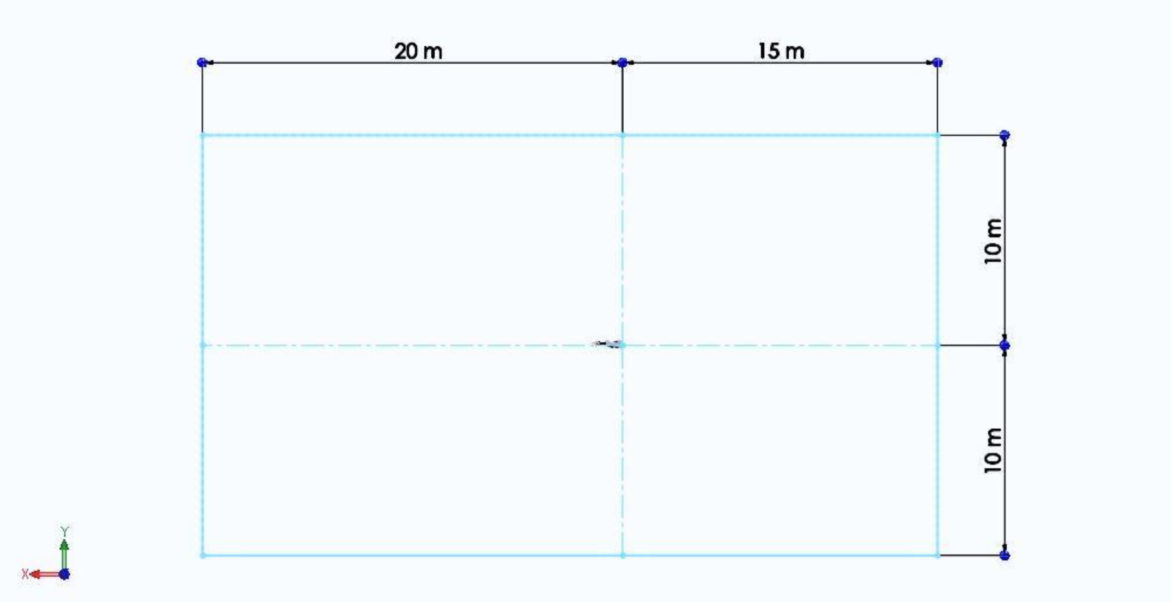

Figure 5.1: Dimensions of the computational domain

In “*Ansys Mesher”* an unstructured mesh is chosen for this domain and it is made by a grid of tetrahedral elements. The mesh “*sizing”* is an input value which controls the dimensions of the mesh cells. A general value can be adjusted, but particular grid-cell sizes can be applied in areas which need finer elements to solve the flow. A “*face-sizing”* has been also introduced; it is a sizing parameter which is referred to the smallest element on the body surface. In critical points such as surfaces with high curvature, spikes or thin volumes the dimensions of the cells are reduced and their number increased to keep the mesh quality high. The element sizing in these simulations is included into values ranging from *0,02 m* (on the fuselage) to *0,001 m* (on the trailing edge of the tail)*;* the general sizing for the whole domain is set to *0,01 m.* These settings applied to this geometry lead to meshes with few millions of elements. Their number varies from 2.564.353 in the standard case mesh, to 3.036.133 of the mesh of the most geometrically complex tip #3. *“Ansys Fluent R14”* numerical simulation is obtained using a pressure based method with coupling algorithms for velocity and pressure. The methods used are a second order approximation in space (for steady and transient cases) and in time (for unsteady cases). The *κ-ω SST (“Shear stress transport”)* [42, 43] is the turbulent modeling used to close the *RANS* equations. It is a very strong and stable model, particularly suggested for low Reynolds number flows, characterized by high velocity gradients. However, it is heavier from the point of view of the computational effort. This method makes use of a transition function which couples Standard *κ-ω* model (applied close to the walls) with *κ-ε* model (optimized for high Reynolds number flows). The latter is used far from the boundary layer. The method presented here takes into account the effects of the shear stress transport due to turbulence; it usually gives an accurate solution concerning separation of boundary layers and their thicknesses. *Monitors* of the flow variables are set up to write output files of aerodynamic coefficients to *.txt* files each *timestep*; they are used later on to plot graphs of functions and to calculate mean values of performances. All aerodynamic simulations are run with standard air at the sea level.

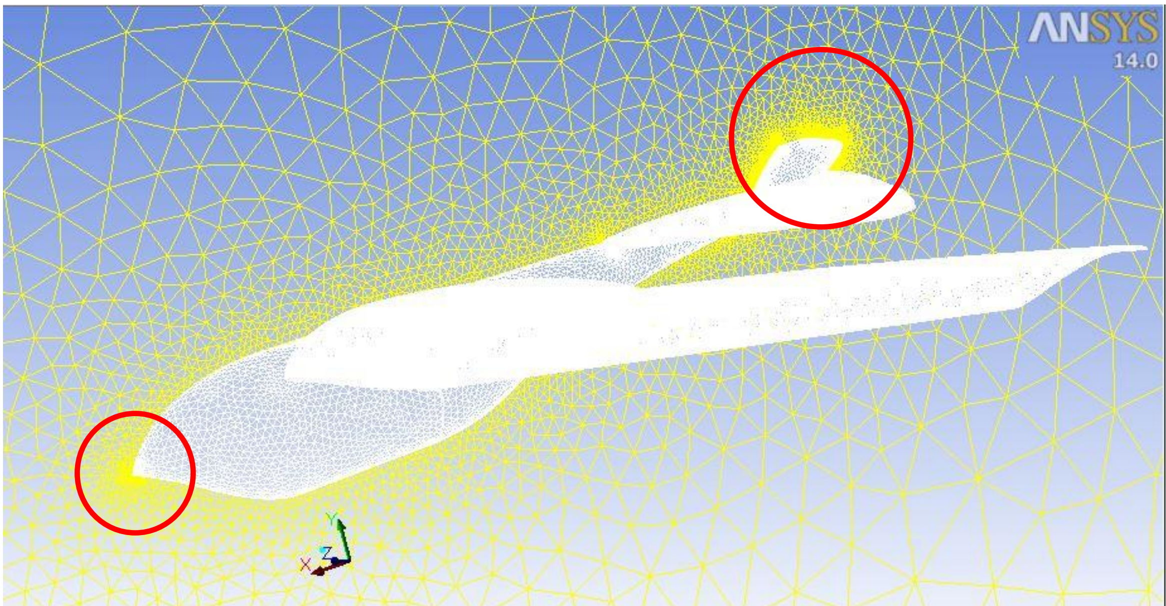

Figure 5.2: Mesh structure around the *Skybird.* The small grid elements around critical points are highlighted within the red circles.

5.2 Data results summary

All sets of simulations are presented with the specific characteristics, plotted functions and tables of results. Pictures representing the development in space of the turbulence trails and streamlines will be presented in the following.

5.2.1 Relative flapping angle study

Set of simulations	*Relative flapping angles (RFA)*
Number of simulations	*3 cases*
Type of simulations	*Unsteady, periodical*
Frequency of the cycle	*3 Hz*
Flow velocity	*5 m/s*
Angle of attack	*0°*
Wing span scale	*1 m*
Time step amplitude	*0.0005 s*
Duration of simulation	*0.7 s (0.0005x1400 time steps)*

Table 8: Simulation set #1 overview of input data.

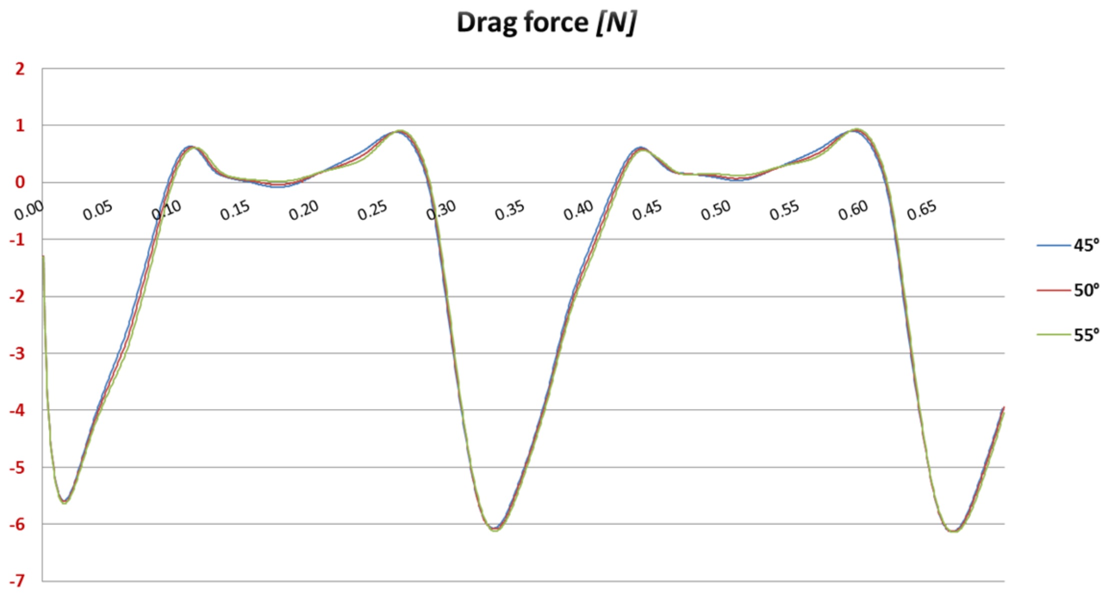

Figure 5.3: Drag as functions of time for three cases of study.

Drag results		
case	**mean force value [*N*]**	**behavior**
45°	*-1.152767522*	*-1.47%*
50° (standard)	*-1.169924270*	----
55°	*-1.181180424*	*+0.96%*

Table 9: Summary of drag forces for three cases of study.

From Figure 5.3 and Table 8, it can be seen that drag is only slightly affected by the relative angle of flapping between the two semi wings. The last column of the table shows the relation with the value of the standard case which is set to *50* degrees of flapping (everything else being fixed at the same conditions). It has to be noticed that negative drag means efficient thrust; the negative peak of the function corresponds to the *downstroke* of the wing. Mean force values are calculated in the fluid solver by integration of the pressure distribution. To compute mean drag coefficient value C_D is enough the well-known following formula:

$$C_D = \frac{2D}{\rho V^2 S} \tag{5.1}$$

where D is the drag coefficient, ρ the fluid density, V the velocity of the flow and S the relative planform surface.

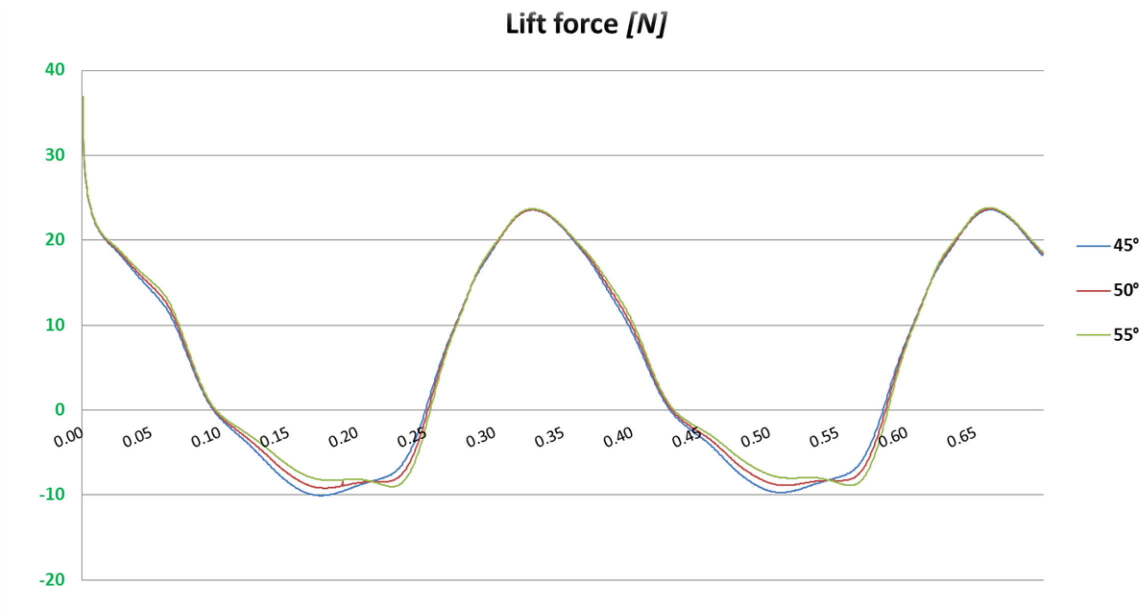

Figure 5.4: Lift as functions of time for three cases of study.

Lift results		
case	**mean force value [*N*]**	**behavior**
45°	*4.765420115*	*-4.04%*
50° (standard)	*4.966184173*	----
55°	*5.174899468*	*+4.20%*

Table 10: Summary of lift forces for three cases of study.

Figure 5.4 and Table 10 show lift function behavior in time. In the same way of the drag function, positive peaks of lift are referred to the *downstroke* of the wing. Still few percentage points are involved in the variation of the lift as function of the *RFA.* Lift coefficient can be calculated in the same way as the drag coefficient, using Lift *L* instead of Drag *D* in equation (5.1).

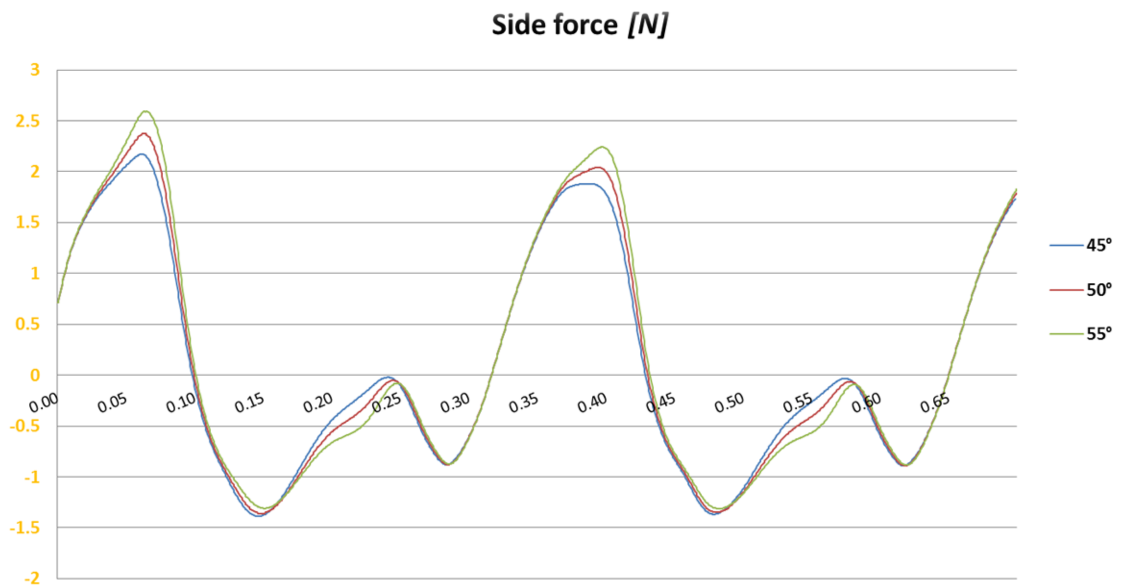

Figure 5.5: Side force as functions of time for three cases of study.

Side force results		
case	**mean force value [*N*]**	**behavior**
45°	*-0.005658194*	*-107.79%*
50° (standard)	*0.072593537*	----
55°	*0.172915235*	*+139.20%*

Table 11: summary of lift forces for three cases of study.

When looking at side effects (Figure 5.5 and Table 11), forces are widely affected by the parameter of the relative flapping angle. In fact the *45°* case shows a side force which is even negative (force pulling inwards), whereas increasing the *RFA* by only *5 degrees* makes the side force raise by a factor of 2.4. The magnitude of the force should not cause mechanical and structural problem. However, this behavior of the side force must make designers aware of the sensitivity of the side force to this parameter.

5.2.2 Wingtip study

Set of simulations	*Wingtip Study*
Number of simulations	*4 cases (1 standard + 3 customized)*
Type of simulations	*Unsteady, periodical*
Frequency of the cycle	*3 Hz*
Flow velocity	*5 m/s*
Angle of attack	*0°*
Wing span scale	*1 m*
Time step amplitude	*0.0005 s*
Duration of simulation	*0.7 s (0.0005x1400 time steps)*

Table 12: Simulation set #2 overview of input data.

5.2.2.1 Standard case "0.0"

As shown in Figure 5.7, the geometry of the case is the plain one; no tips or any customized geometries are involved. The results of this case will be later on taken as a reference point for comparison purposes.

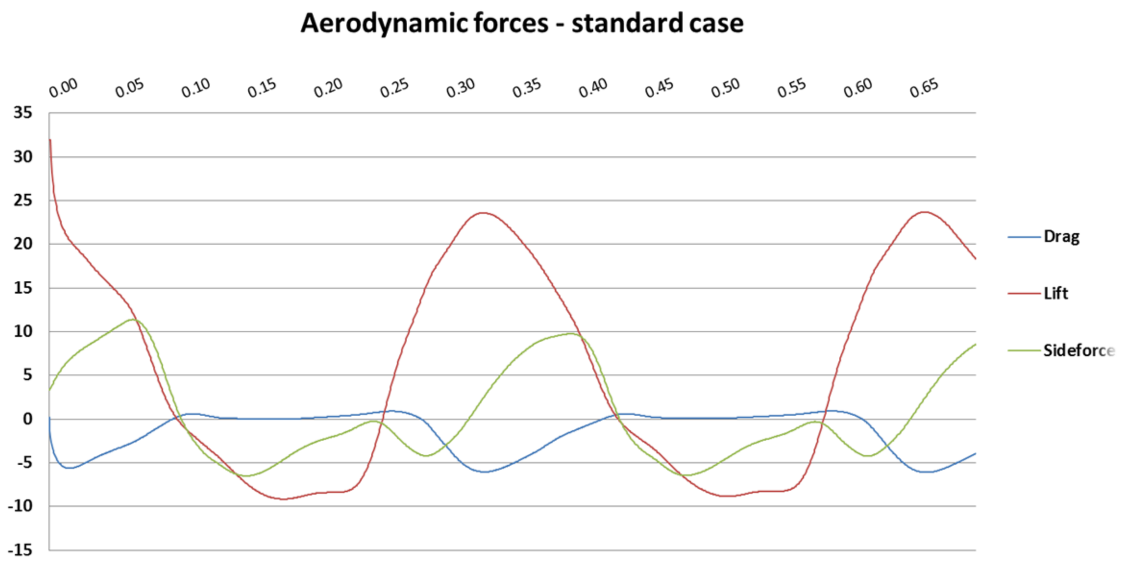

Figure 5.6: Behavior in time of drag, lift and side force functions (standard case).

Results table	
Force	**mean force value [*N*]**
Drag	*-1.1555258*
Lift	*4.9778816*
Side force	*0.0677256*

Table 13: Aerodynamic forces of standard case *"0.0"*.

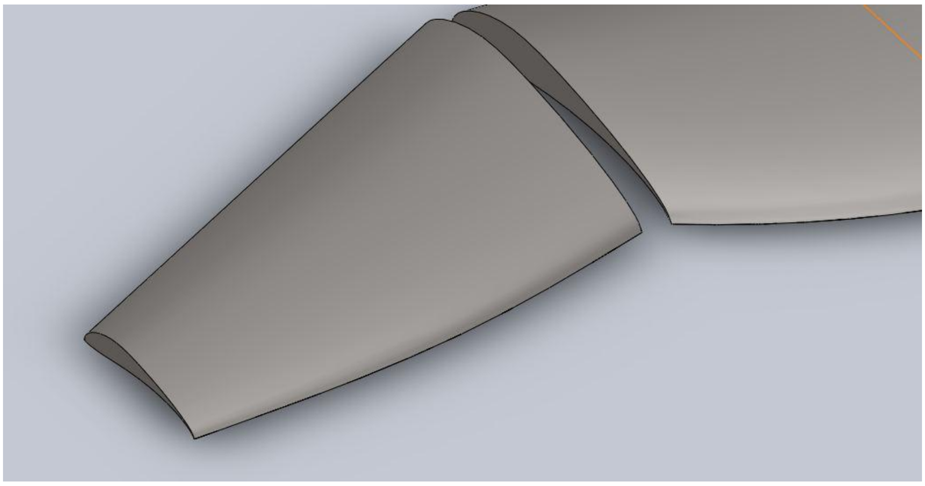

Figure 5.7: Standard wing with straight edges and cut end.

5.2.2.2 Tip #1

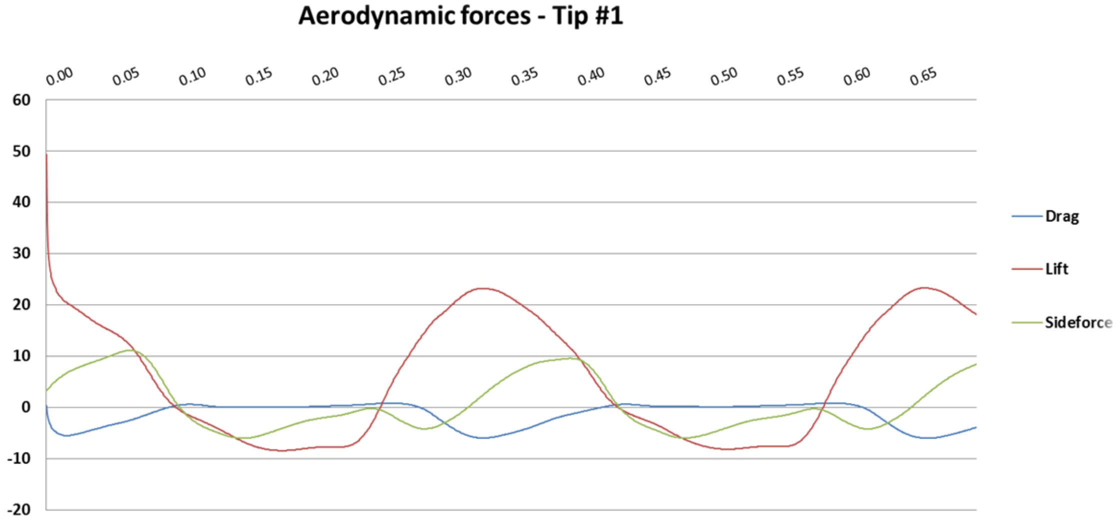

Figure 5.8: Behavior in time of drag, lift and side force functions (Tip #1).

Results table			
Force	**mean reference force value [*N*]**	**mean force value [*N*]**	**behavior with respect to the standard case**
Drag	*-1.1555258*	*-1.134893647*	*-1.79%*
Lift	*4.9778816*	*5.092041289*	*+2.29%*
Side force	*0.0677256*	*0.144298904*	*+113.06%*

Table 14: Aerodynamic forces of Tip #2 case.

Looking at Table 14, it can be noticed that drag and side force values are not improved. However, tip #1 is the only customized geometry which increases lift performances during flapping motion. Then, attention should be focused on which parameter of the geometry is responsible for the improved performances. Drag is only slightly affected and, despite the simplicity of this winglet, it is expected to be one of the most useful geometry as far as dynamic simulations are concerned.

5.2.2.3 Tip #2

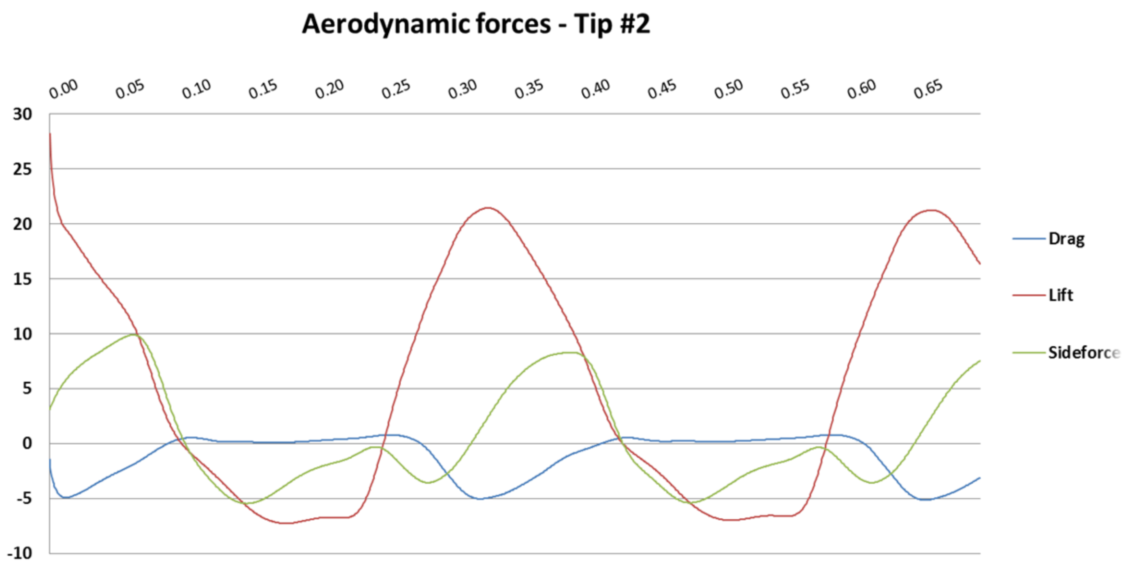

Figure 5.9: Behavior in time of drag, lift and side force functions (Tip #2).

Results table			
Force	**mean reference force value [*N*]**	**mean force value [*N*]**	**behavior with respect to the standard case**
Drag	*-1.1555258*	*-0.9023247*	*-21.91%*
Lift	*4.9778816*	*4.7031730*	*-5.52%*
Side force	*0.0677256*	*0.1101008*	*+62.27%*

Table 15: Aerodynamic forces of Tip #2 case.

Tip #2 performs even worse than the standard case from any point of view. It was expected, at least, an improvement in lift, coming from the particular geometry (cf. section 3.3.3.2). However, the reverse cup shape of the tip, which characterizes this geometry, apparently makes its effect only in raising the side force. As far as the drag coefficient is concerned, a reduction of its negative value can be observed. At first sight this could suggest less drag, but the values only says that thrust has been reduced. This makes sense. A round shape is suggested for gliding to minimize induced drag; however, this wing is flapping and other phenomena involved have a greater physical weight. During *downstroke* the straight edge of the standard case wing pushes the mass of air more efficiently than a wing equipped with a round tip; where; on the contrary, air slips also laterally outwards of the wing.

5.2.2.4 Tip #3

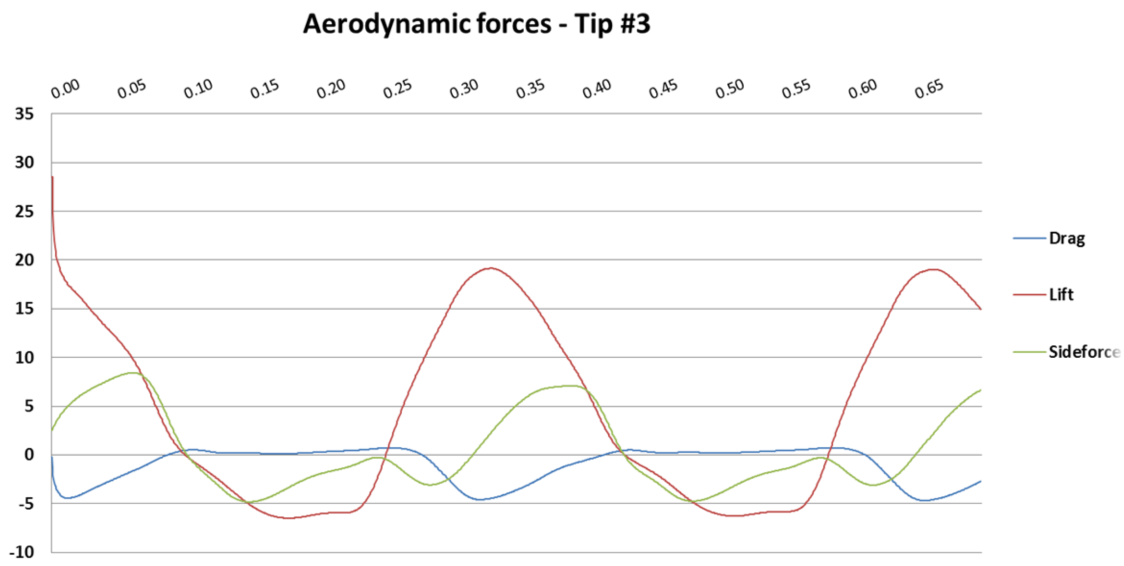

Figure 5.10: Behavior in time of drag, lift and side force functions (Tip #3).

Results table			
Force	**mean reference force value [*N*]**	**mean force value [*N*]**	**behavior with respect to the standard case**
Drag	*-1.1555258*	*-0.7927476*	*-31.40%*
Lift	*4.9778816*	*4.1684147*	*-16.26%*
Side force	*0.0677256*	*0.0685565*	*+1.23%*

Table 16: Aerodynamic forces of Tip #3 case.

This should have been the most advanced tip geometry. However, results data in Table 16 show that aerodynamically this tip does not improve performances. It is likely that some of the problems come from the interaction of the flow structures produced by the feathers. This can be avoided by placing *remiges* staggered on the *z-x* plane. This would make turbulence created by feathers develop and dissipate instead of interfere with other parts. Below an example of a gliding eagle is shown: it can be noticed how *Primaries* do not belong to the same horizontal plane. Thus, keeping them separated and non-coplanar, should improve drag performances.

Figure 5.11: Eagle in gliding flight.

It has also to be said that the rear edge of the tip is not straight, but in some way rounded. This can badly affect thrust due to issues discussed before in section 5.2.2.3 about tip #2. Also lift has worsened with respect to the standard case. Since coefficients are integrated by *Fluent* from pressure distribution, the wing area scale cannot affect values, only aerodynamic properties can. Thus, it can be hypothesized that lift lowering can be produced by the following situation. Air flow can possibly go through the feathers more easily than overcoming the straight edge of the standard case. This situation can be clarified thinking about a cylindrical and a square bars (with same projected areas) which are moved inside a high viscous fluid such as water or oil; square edges create more turbulence, dissipates more energy and it needs more power to be moved around. Despite the aerodynamic behavior of tip #3; this could still be useful since it is very adapted to biomimetic task. The *UAV* aspect is much more realistic if it is equipped with devices reproducing the outline of a real bird. After a revision according to what said before, tip #3 can be a possible tip if applied to a configuration which satisfies by itself all performance requirements.

5.2.3 Steady simulations of the tips

Set of simulations	*Wingtip Study*
Number of simulations	*4 cases (1 standard + 3 customized)*
Type of simulations	*Steady*
Frequency of the cycle	--
Flow velocity	*5 m/s*
Angle of attack	*0°*
Wing span scale	*1 m*
Number of iterations	*1000*
Duration of simulation	*1 single step (in time 00:000 s)*

Table 17: Simulation set #3 overview.

A quick set of steady simulations has been run as an addition to the wingtip study. The theory beneath the use of winglets is well-known for gliding flight with rigid wings, such as airplanes or gliders. In this case customized wingtips must have a positive effect on performances.

Drag results

Case	Drag *[N]*	Behavior
"0.0"	*0.36950131*	--------
Tip #1	*0.36321591*	*-1.70%*
Tip #2	*0.34249744*	*-7.30%*
Tip #3	*0.32653855*	*-11.63%*

Lift results

Case	Lift *[N]*	Behavior
"0.0"	*2.79745664*	--------
Tip #1	*2.68414924*	*-4.05%*
Tip #2	*2.62945241*	*-6.01%*
Tip #3	*2.43762642*	*-12.86%*

Side force results

Case	Side force *[N]*	Behavior
"0.0"	*0.19103845*	--------
Tip #1	*0.17705841*	*-7.32%*
Tip #2	*0.18318133*	*-4.11%*
Tip #3	*0.16948945*	*-11.28%*

Table 18: Tables of results of wingtips steady simulations.

Tables 18 present the results of steady simulations of the wingtips. All the wing geometries provided with a wingtip reduce the drag coefficient and consequently the drag force. This is due to the reduction of the induced drag, coming from wingtip vortices. Also the side force decreases for all cases. This result is harder to explain. As far as lift is concerned, apparently all the customized cases make it worse compared to the standard case. Later on (cf. *Chapter 6*) it will be explained why this is not completely true.

5.2.3.1 Results visualization

The graphic visualization of the results coming from the complete solution of the fluid domain is called *"post-processing"*. Commercial software dedicated to this is available to quickly understand the nature of the results. Below pictures exported from the program *EnsightGold* [38] show streamlines and vorticity at the wingtips due to separated boundary layers.

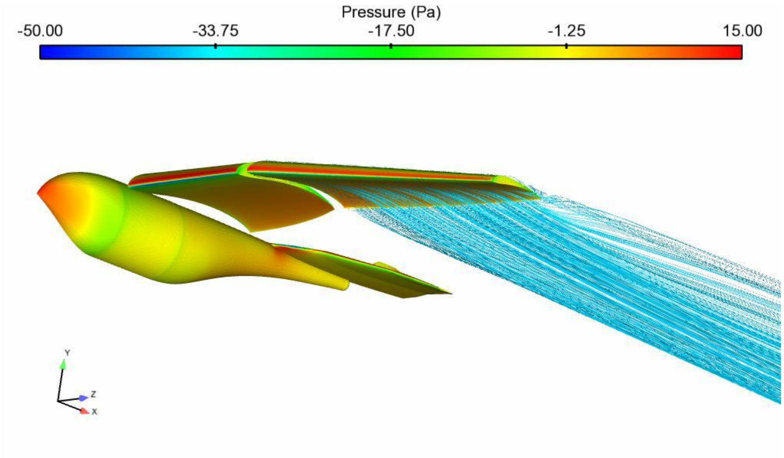

Figure 5.12: Visualization of static pressure on the surface and streamlines around the wing (standard case).

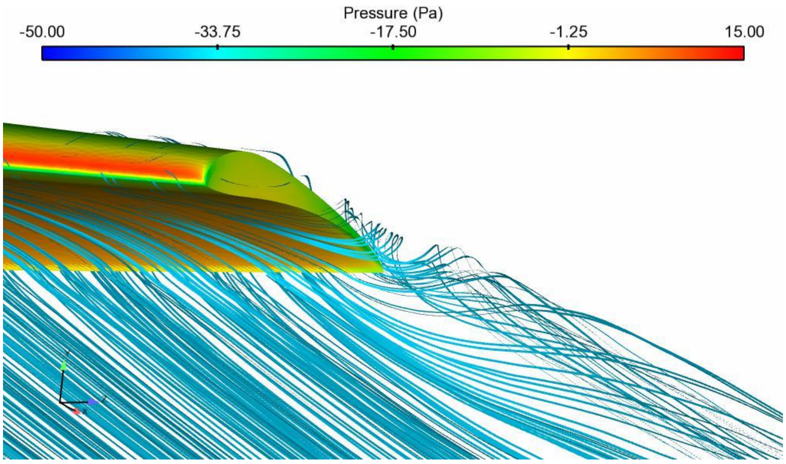

Figure 5.13: Detail of the wingtip vortices (standard case).

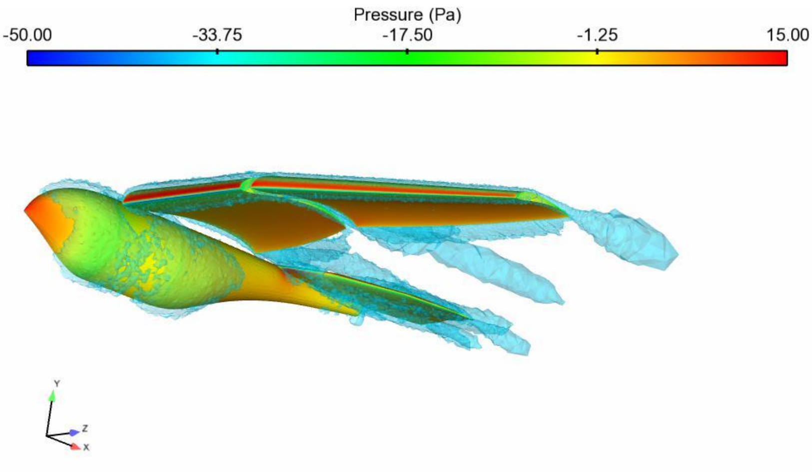

Figure 5.14: Visualization of dynamic pressure on the wing and trail by Q-criterion [37] (standard case).

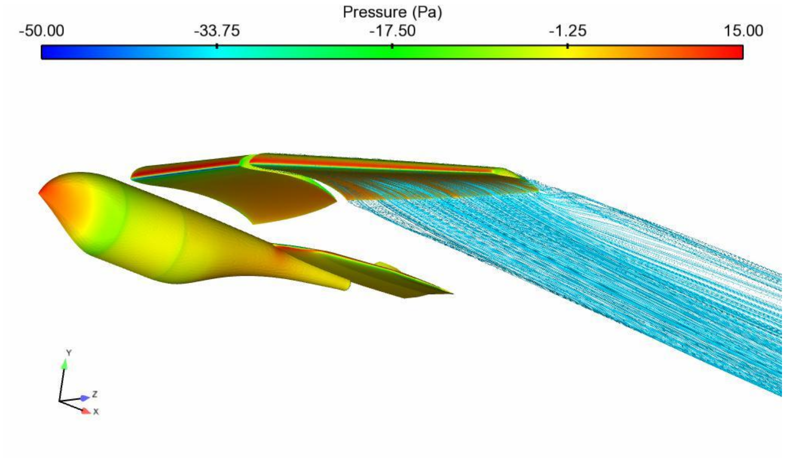

Figure 5.15: Visualization of static pressure on the surface and streamlines around the wing (tip #1 case).

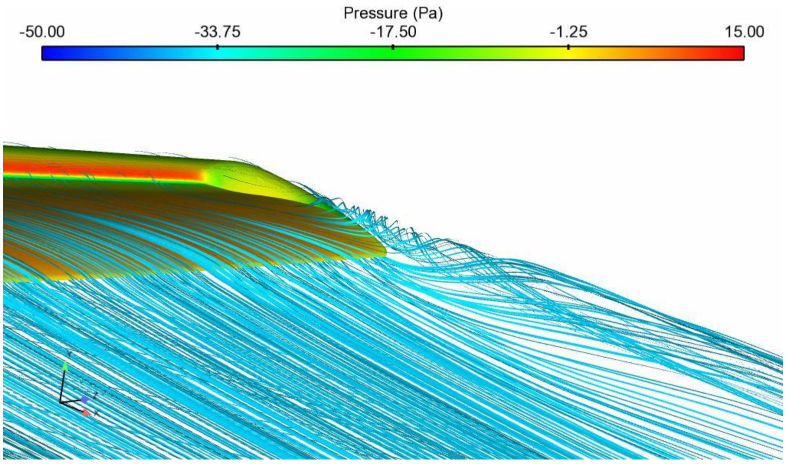

Figure 5.16: Detail of the wingtip vortices (tip #1 case).

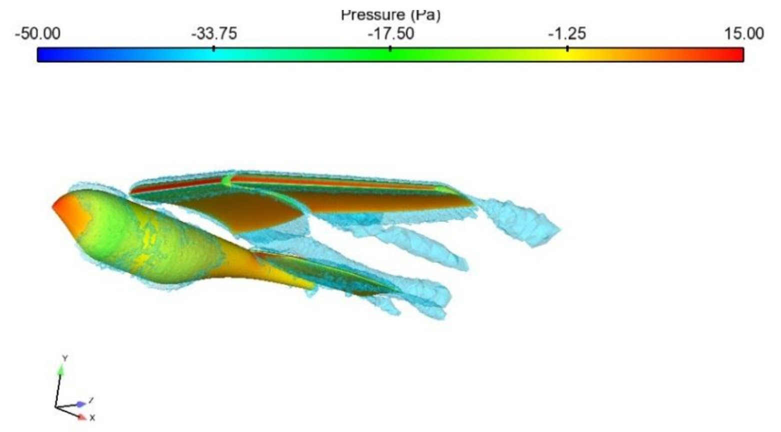

Figure 5.17: Visualization of dynamic pressure on the wing and trail by Q-criterion [37] (tip #1 case).

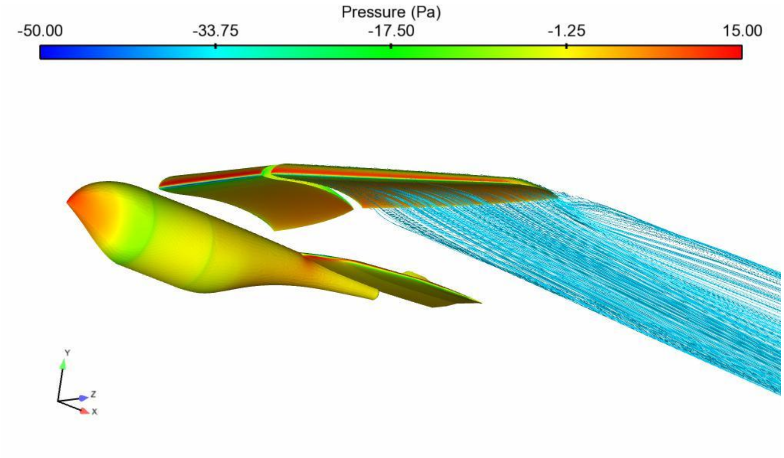

Figure 5.18: Visualization of static pressure on the surface and streamlines around the wing (tip #2 case).

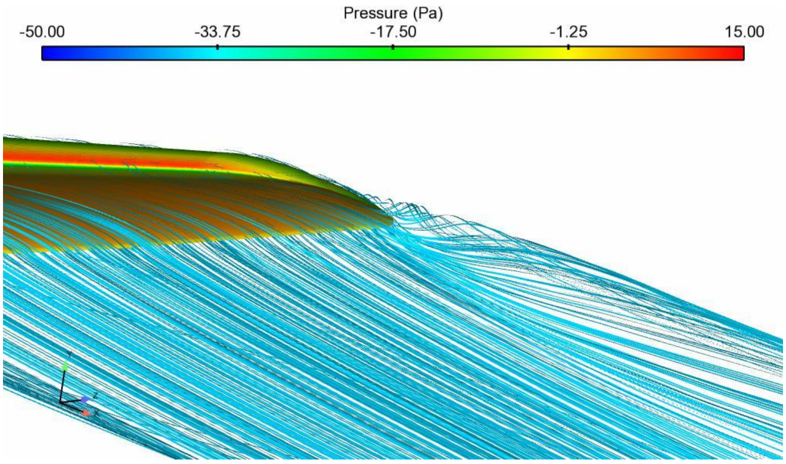

Figure 5.19: Detail of the wingtip vortices (tip #2 case).

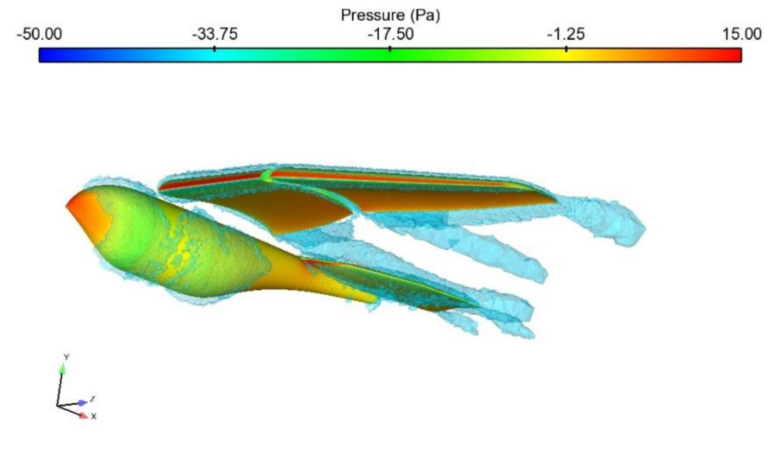

Figure 5.20: Visualization of dynamic pressure on the wing and trail by Q-criterion [37] (tip #2 case).

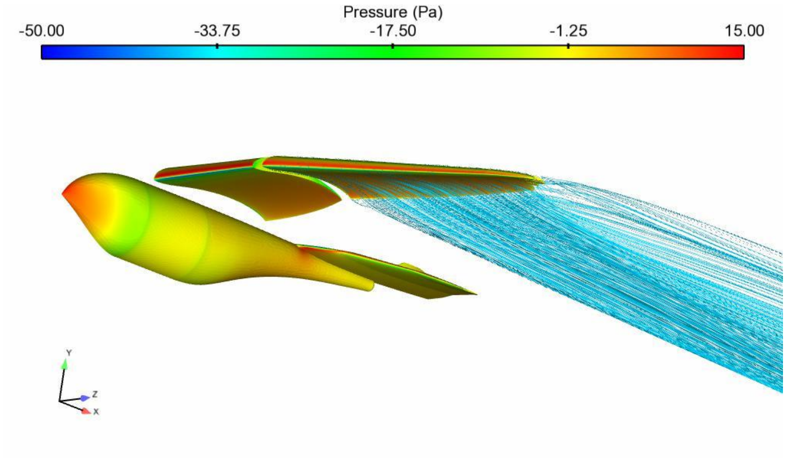

Figure 5.21: Visualization of static pressure on the surface and streamlines around the wing (tip #3 case).

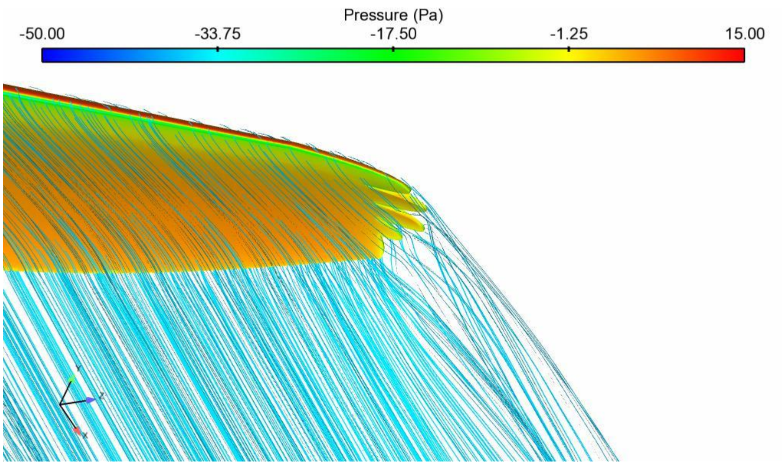

Figure 5.22: Detail of the wingtip vortices (tip #3 case).

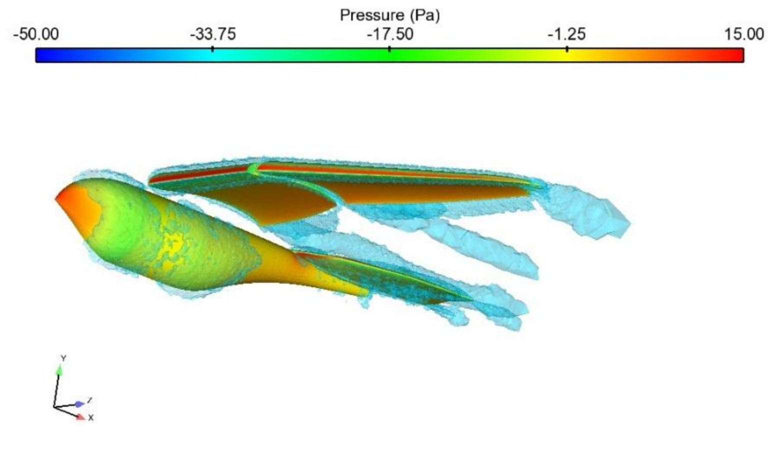

Figure 5.23: Visualization of dynamic pressure on the wing and trail by Q-criterion [37] (tip #3 case).

5.2.4 Biomimetic planform

Set of simulations	*Biomimetic planform*
Number of simulations	*1 case*
Type of simulations	*Unsteady, periodical*
Frequency of the cycle	*3 Hz*
Flow velocity	*5 m/s*
Angle of attack	*0°*
Wing span scale	*1 m*
Time step amplitude	*0.0005 s*
Duration of simulation	*0.7 s (0.0005x1400 time steps)*

Table 19: Simulation set #4 overview of input data.

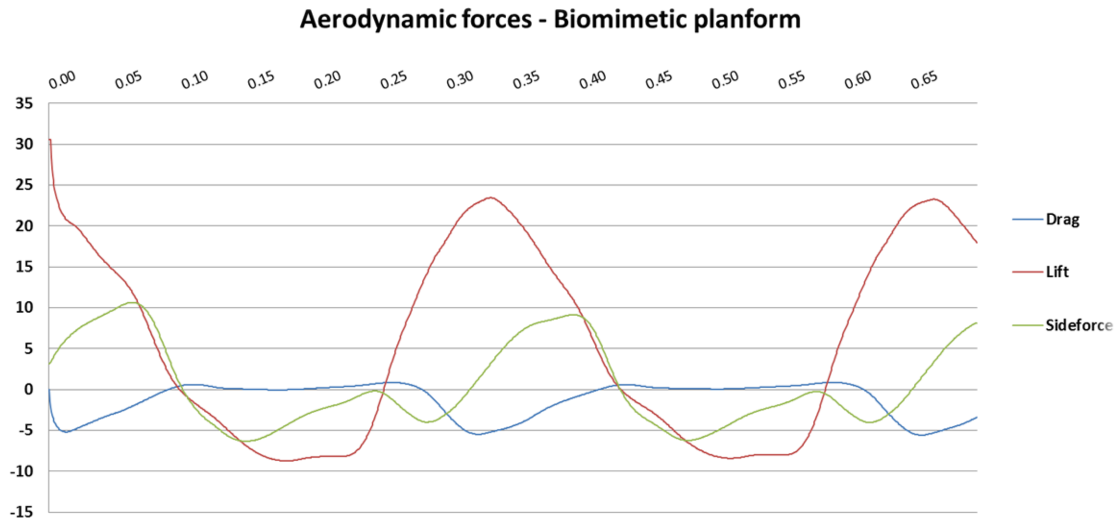

Figure 5.24: Behavior in time of drag, lift and side force functions (Biomimetic planform).

Results table			
Force	**mean reference force value [*N*]**	**mean force value [*N*]**	**behavior with respect to the standard case**
Drag	*-1.1555258*	*-0.992247722*	*-14.13%*
Lift	*4.9778816*	*4.853116597*	*-2.51%*
Side force	*0.0677256*	*0.006943470*	*-89.75%*

Table 20: Aerodynamic forces of Biomimetic planform case.

In Figure 5.24 it can be easily seen that the side force presents a different shape from all other cases. This relates to the most surprising value reported in Table 20. Granted that lift and thrust are subjected again to a negative variation, side force value is incredibly reduced. Its value in fact collapses by an order of magnitude; it goes from approximately *0.068 N* for the standard case to *0.0069 N* for this case. The causes of this effect are not completely clear, but it can be related to the particular shape, which lets the side flow slide around the wing creating less turbulence than the standard shape. This result is very interesting because it is applicable regardless of the decisions on the wingtips, since it involves the plain *"0.0"* geometry.

A simulation with rigid wings has also been run for the biomimetic geometry of the wing. Results are shown in Table 21.

Steady simulation results

Force	Mean value *[N]*	behavior
Drag	*0.358274754*	*-3.04%*
Lift	*2.649006789*	*-5.31%*
Side force	*0.176678027*	*-7.52%*

Table 21: Table of results of steady simulation for gliding flight.

Likewise the dynamic behavior of the biomimetic edge, the parameter mostly affected is the side force. Drag is reduced as well by the *3%*, from a loss in lift. The lift loss issue will be covered more in detail in *Chapter 6*.

Figures below visualize aerodynamic flow structures for biomimetic planform still taken from *EnsightGold*.

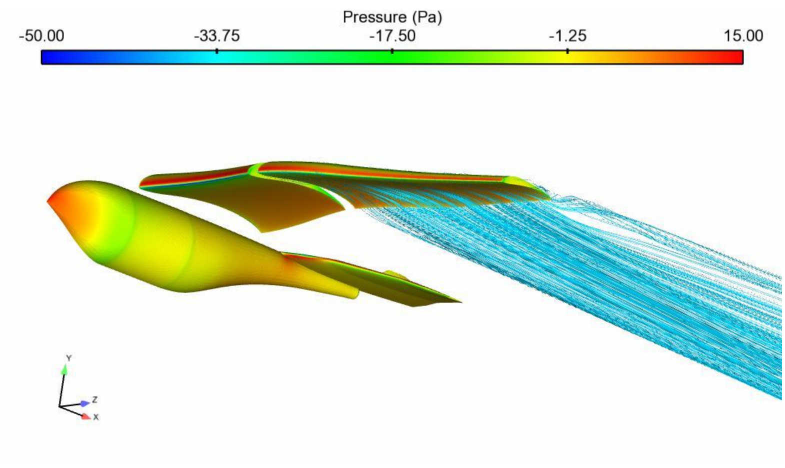

Figure 5.25: Visualization of static pressure on the surface and streamlines around the wing (biomimetic planform case).

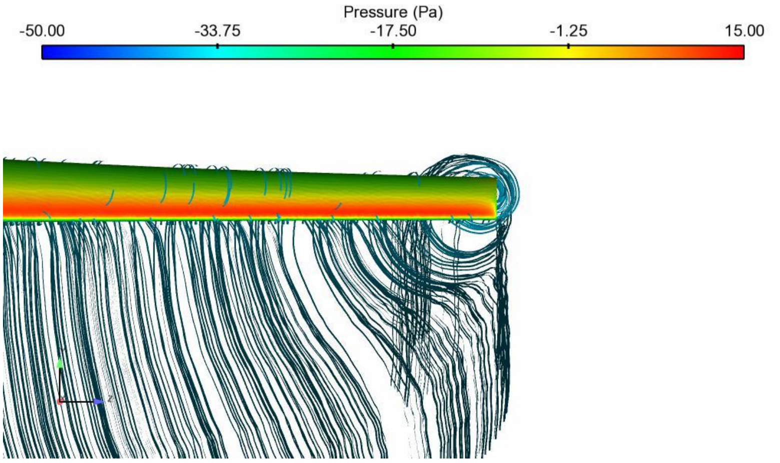

Figure 5.26: Detail of the wingtip vortices (biomimetic planform case).

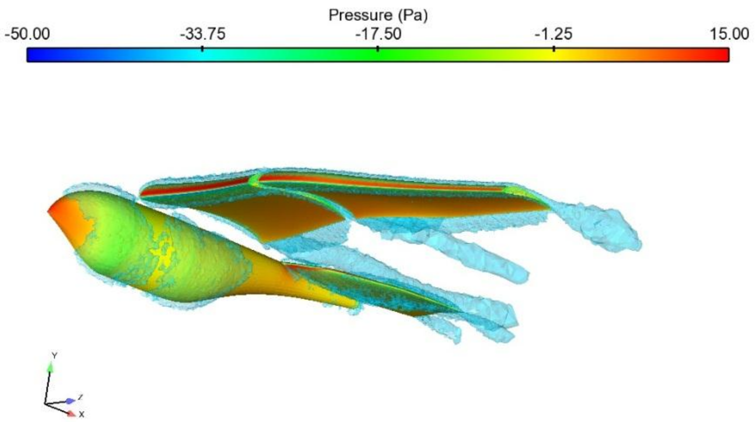

Figure 5.27: Visualization of dynamic pressure on the wing and trail by Q-criterion [37] (biomimetic planform case).

To make sure that the results were not affected by set up mistakes, *monitors* of the drag coefficient on the fuselage and the tail called *cdfuse.dat* and *cdtail.dat*, have been compared for different cases. Table 22 below, shows mean values for all of them. They differ from each other by a value which can reasonably be related to the different eddies shed by the tips of the flapping wing. Since values are very small, their variations are even smaller.

Case	Mean Drag value (fuselage)	Mean Drag value (tail)
Standard	0.0196606	0.0138822
Tip #1	0.0171312	0.0100677
Tip #2	0.0178917	0.0069025
Tip #3	0.0184848	0.0048280
Biomimetic shape	0.0181635	0.0083728

6. Conclusions and future work

This thesis is a report of aspects of the advanced design of a long term project. First of all, an introduction to the topic of interest and to the state-of-the-art in the field have been presented.

Results of previous simulations pointed out that to obtain required lift and thrust two options are possible. The first one is to introduce a complex kinematics involving dynamic twisting of the wing. That would improve much the aerodynamic coefficients in flapping flight. However, it would mean to complicate the structure by introducing servo motors at the wing tip to generate the motion. Not less important, payload and inertia forces involved would be certainly higher in that case. The second option is to increase the wing total span from *1.5 m* to *2 m.* This would lead to higher loads to the mechanical structure. In either case, the aerodynamics of the wing should be improved by advanced geometries, in order to earn in performances.

A set of wingtips has been drawn using *"Solidworks 2011"*; from the simplest ones to the biomimetic inspired geometry. Then, they have been assembled with the rest of the geometry of the *Skybird* and exported to "*Ansys Design Modeler".* Next step has been the creation of a fluid domain, over which we have generated *meshes* of the geometries to run the simulations.

The first set of *CFD* experiments has been about the relative flapping angle. The expected behavior has been confirmed: forces involved not only change proportionally with the *RFA*, but also they are almost linear in the considered domain (this can be seen from Tables 9, 10 and 11 which show how values vary approximately of the same quantity in each direction). Hence, the choice on the optimum kinematics will be based on a compromise between allowable forces from the structure and aerodynamic requirements.

A second set of simulations involved the geometrical optimization of the wing. Therefore, wingtips have been created with the purpose of reducing the induced drag. An aerodynamic edge of the wing has also been designed to produce less resistance against the air flow. The latter geometry and the tip #3 are also apt for biomimetic usage. As far as the dynamic simulations are concerned, performances do not improve consistently with the introduction of the customized wingtips. The only exception is in the biomimetic profile, which makes the side force collapse by an order of magnitude. However, steady simulations of gliding flight have been more encouraging. Winglets work perfectly: drag is reduced by values ranging from *1.7%* to *11.68%*. Results say also that lift values go down proportionally to drag values, but a further explanation must be given. Drag value is the most concerning parameter in a simulation which tests the efficiency of devices such as the winglets. Thus, the span of a single wing has been scaled for each case and kept as the constant parameter in order to have the same projected frontal area. This implies that wing provided with winglets have less planform area than the standard one, due to the presence of the round tips. Lift is proportional to such area and thus results concerning lift are affected by it. The configuration characterized by the biomimetic edges behaves exactly in the same way: less drag and side force, but the lift suffers from the reduced planform area compared to the reference case.

At this point of the development, the forces at play are sufficiently well known to integrate the aerodynamic improvements with the mechanical structure. The DIME department has finished developing the kinematic train, with the aid of software such as Virtual Lab [36]. Whereas Ghelardi [11] has led a study on the flight stability and he ended up with a tail configuration for the *Skybird* under gliding conditions. Study of the payload and the choice of materials will be the concern of next steps of the development. The greatest part of the future work will certainly be putting together all the studies and results. They have been obtained by different people, in different areas, but all with the same purpose: make the *Skybird* fly.

Bibliography

[1]. F. Negrello: Configurazioni esistenti di *UAV* ad ali battenti, con caratteristiche geometriche, prestazioni, tipo di cinematismi e materiali costruttivi. Relazione tecnica Selex Galileo MUAS #1, (2011).

[2]. http://www.greenx.nl/

[3]. http://www.ornithopter.net/index_e.html

[4]. http://ornithopter.de/english/literature.html

[5]. http://www.festo.com/cms/en_corp/11369.html

[6]. http://www.youtube.com/watch?v=Fg_JcKSHUtQ

[7]. T. Liu, K. Kuykendoll, R. Rhew, S. Jones: Avian wings. AIAA paper 2004-2186, (2004).

[8]. http://www.arizona-software.ch/graphclick/

[9]. http://www.solidworks.it/

[10]. M. S. Selig, J. J. Guglielmo, A. P. Broeren, P. Giguere: Summary of low-speed airfoil data (volume 1). SoarTech Publications, Virginia, (1955).

[11]. F. Ghelardi: Sviluppo geometrico/aerodinamico della superficial di coda di un velivolo in volo planato, Tesi di Laurea in Ingegneria Meccanica, Università di Genova, Sept. 2012.

[12]. W. Shyy, Y. Lian, J. Tang, D. Viieru & H. Liu: Aerodynamics of low Reynolds number flyers. Cambridge U. Press, (2008).

[13]. http://www.ansys.com/

[14]. C.Pacioselli: Sviluppo Aerodinamico di un velivolo ad ala battente, , Tesi di Laurea Magistrale in Ingegneria Meccanica, Università di Genova, March 2012.

[15]. A.Bottaro, J.Guerrero: Studio Preliminare Sulle Prestazioni dello Skybird. Relazione tecnica Selex Galileo MUAS #4, April 2012.

[16]. A. Bottaro, J.Guerrero, C.Pacioselli, J. Pralitz, F. Negrello, P. Silvestri: Skybird: Preliminary Design, January 2012.

[17]. C. J. Pennycuick: Modelling the flying bird. Academic Press, (2008).

[18]. H. Tennekes: The Simple Science of Flight. From Insects to Jumbo Jets. Revised and Expanded Edition. MIT Press, (2009).

[19]. http://www.redhammer.se/tornado/

[20]. J. Moran: Computational Fluid Dynamics. Wiley & Sons, (1984)

[21]. J. Anderson: Fundamentals of aerodynamics (3rd edition). McGraw-Hill, (2001).

[22]. J. D. Anderson: Computational Fluid Dynamics: The Basics with Applications. McGraw-Hill, (1995).

[23]. D. Drikakis and W. Rider: High-Resolution Methods for Incompressible and Low-Speed Flows. Springer, (2005).

[24]. C. A. J. Fletcher: Computational Techniques for Fluid Dynamics: Volume 2: Specific Techniques for Different Flow Categories. Springer, (1996).

[25]. J. H. Ferziger and M. Peric: Computational Methods for Fluid Dynamics. Springer, Second Edition, (2002).

[26]. E. F. Toro: Riemann Solvers and Numerical Methods for Fluid Dynamics. Springer, Third Edition, (2009).

[27]. H. Versteeg and W. Malalasekera: An Introduction to Computational Fluid Dynamics: The Finite Volume Method. Pearson, Second Edition, (2007).

[28]. S. Patankar: Numerical Heat Transfer and Fluid Flow. McGraw-Hill, (1980).

[29]. R. H. Pletcher, J. C. Tannehill and D. A. Anderson: Computational Fluid Mechanics and Heat Transfer. Taylor and Francis, Second Edition, (1997).

[30]. R. J. LeVeque: Finite Volume Methods for Hyperbolic Problems. Cambridge Texts in Applied Mathematics, (2002).

[31]. H. Jasak: Error Analysis and Estimation for the Finite Volume Method with Application for Fluid Flows. PhD Thesis, Imperial College London, (1996).

[32]. J. Blazek: Computational Fluid Dynamics: Principles and Applications. Elsevier, Second Edition, (2003).

[33]. J.E. Guerrero, D. Maestro & A. Bottaro: Biomimetic spiroid winglets for lift and drag control. C. R. Mécanique, Vol. 340 (2012) pp. 67-80

[34]. G.K. Taylor, R.L. Nudds & A.L.R. Thomas: Flying and swimming animals cruise at a Strouhal number tuned for high power efficiency. Nature, Vol. 425 (2003) pp.707-711

[35]. M.S. Triantafyllou, G.S. Triantafyllou & D.K.P. Yue: Hydrodynamics of fish-like swimming. Annual Review of Fluid Mechanics, Vol. 32 (2000) pp. 33-53

[36]. http://www.lmsintl.com/virtuallab

[37]. R. Haines, D. Kenwright: On the velocity gradient tensor and fluid feature extraction. AIAA Paper 1999-3288-CP, 1999.

[38]. http://www.ceisoftware.com/ensight10/

[39]. T. J. Barth and D. C. Jespersen: The Design and Application of Upwind Schemes on Unstructured Meshes. AIAA Paper, 89-0366, AIAA 27th Aerospace Sciences Meeting, Reno, Nevada, (1989).

[40]. S. E. Kim, B. Makarov and D. Caraeni: A Multi-Dimensional Linear Reconstruction Scheme for Arbitrary Unstructured Grids. Technical Report, AIAA Paper, 2003-3990, AIAA 16th Computational Fluids Dynamics Conference, Orlando, Florida, (2003).

[41]. C. M. Rhie and W. L. Chow: Numerical Study of the Turbulent Flow Past an Airfoil with Trailing Edge Separation. AIAA Journal, 21(11), (1983), pp. 1525-1532.

[42]. D. C. Wilcox: Re-assessment of the Scale-Determining Equation for Advanced Turbulence Models. AIAA Journal, vol. 26(11), (1988), pp. 1299-1310.

[43]. D. C. Wilcox: Turbulence Modeling for CFD. DCW Industries, Third Edition, (2006).